

Simulating Complex Dynamics In Intermediate And Large-Aspect-Ratio Convection Systems

Ming-Chih Lai

Department of Mathematics, Chung Cheng University, Minghsiang, Chiayi 621, Taiwan

Keng-Hwee Chiam and M.C. Cross

Department of Physics, California Institute of Technology, Pasadena, CA 91125

Henry Greenside

Department of Physics, P. O. Box 90305, Duke University, Durham, NC 27708-0305

Abstract

Buoyancy-induced (Rayleigh-Bénard) convection of a fluid between two horizontal plates is a central paradigm for studying the transition to complex spatiotemporal dynamics in sustained nonequilibrium systems. To improve the analysis of experimental data and the quantitative comparison of theory with experiment, we have developed a three-dimensional finite-difference code that can integrate the three-dimensional Boussinesq equations (which govern the evolution of the temperature, velocity, and pressure fields associated with a convecting flow) efficiently in large box-shaped domains with experimentally appropriate lateral boundary conditions. We discuss some details of this code and present two applications, one to the occurrence of quasiperiodic dynamics with as many as 5 incommensurate frequencies in a moderate-aspect-ratio 10×5 convection cell, and one to the onset of spiral defect chaos in square cells with aspect ratios varying from $\Gamma = 16$ to 56.

Introduction

A frontier of great importance for DOE-related research is the study of sustained nonequilibrium dynamical systems, for which imposed external fluxes of energy and matter can lead to states that vary temporally and spatially in a complex way [1]. Despite the collaboration of theorists, computational scientists, and experimentalists over the last thirty years and despite the great need to solve numerous practical engineering problems, many basic questions about sustained nonequilibrium states remain unanswered. Researchers would like to know what possible states can occur for specified external fluxes, how to predict when one state will change into another as some parameter is varied, how transport of energy and matter depends on the spatiotemporal structure of a state, and whether one can select particular states by appropriate external perturbations so as to optimize a system for a particular goal. While experiments and simulations have been useful in suggesting what possibilities can occur (e.g., the surprising experimental discovery of the spiral defect chaos state [2], a numerical example of which is shown below in Fig. 3), there remains a great need to develop a stronger theoretical and conceptual foundation that can unify the many observations and that can improve both experimental and computational investigations.

Perhaps the simplest and best idealized experimental system for exploring basic questions and principles of nonequilibrium systems is Rayleigh-Bénard convection, which has become an experimental and theoretical paradigm for many researchers [1]. A Rayleigh-Bénard experiment consists of a thin layer of fluid confined between two horizontal spatially-uniform constant-temperature metal plates such that the bottom plate is maintained at a constant higher temperature than the upper plate. As the temperature difference (or its dimensionless equivalent, the Rayleigh number R) is increased in successive constant steps, the fluid first makes a transition from a motionless structureless state to cellular overturning convection rolls and then to ever more complex dynamical states which eventually become nonperiodic in space and time. Convection has significant advantages over other experimental systems in having static homogeneous boundary conditions, in having no net flow of fluid through the system, in allowing precise and reproducible experiments with

good visualization, and in being amenable to a quantitative mathematical description through the so-called Boussinesq equations.

In this paper, we report applications of a new computer code to two intriguing convection experiments. The code is the first of several being developed and applied by a Caltech-Duke collaboration whose long-term goal is to understand convection phenomena more quantitatively, especially in the large-aspect-ratio limit (cells whose widths are large compared to their depths) which experiments have shown to be of great interest even close to the onset of convection, where analytical progress is most likely to be possible [1]. Our code differs from some other recently developed codes [3] primarily through the inclusion of experimentally appropriate lateral boundary conditions (rather than periodic boundary conditions) on the velocity and temperature fields so that the forcing due to lateral boundaries can be taken into account. In the following sections, we give a brief summary of the code followed by a discussion and demonstration of how the code can provide new insights about two poorly understood experimental phenomena, the occurrence of dynamics with many incommensurate frequencies in a moderate-aspect ratio convection cell first observed by Walden et al [4] and the onset of spiral defect chaos in domains of varying size (which has not yet been studied experimentally). These results provide new and detailed examples of the substantial influence of lateral boundaries on nonequilibrium dynamics.

Numerical Integration Of The 3D Boussinesq Equations

Since technical details of our numerical algorithm will be available elsewhere [5], we provide only some motivation for and highlights of our numerical method. The goal is to integrate the five coupled three-dimensional nonlinear partial differential equations known as the Boussinesq equations which state (under certain assumptions not given here) the local conservation of momentum, energy, and mass for parcels of fluid subjected to buoyancy forces. By scaling time, space, and field magnitudes in appropriate ways, one can write the Boussinesq equations in the following dimensionless form:

$$\partial_t \mathbf{u} = -\mathbf{u} \cdot \nabla \mathbf{u} - \nabla p + \sigma \nabla^2 \mathbf{u} + \sigma R T \hat{z}, \quad (1)$$

$$\partial_t T = -\mathbf{u} \cdot \nabla T + \nabla^2 T, \quad (2)$$

$$\nabla \cdot \mathbf{u} = 0, \quad (3)$$

where $\mathbf{u}(t, \mathbf{x}) = (u_x(t, \mathbf{x}), u_y(t, \mathbf{x}), u_z(t, \mathbf{x}))$ is the velocity field at time t and position $\mathbf{x} = (x, y, z)$, $T(t, \mathbf{x})$ is the temperature field, $p(t, \mathbf{x})$ is the pressure field, σ is the fluid's Prandtl number which is assumed to be independent of temperature and so a constant, and R is the Rayleigh number which is the key parameter that is varied in most experiments and simulations, usually with all other parameters held fixed. In this paper, we study these equations in a simple box geometry of dimensions $\Gamma_x \times \Gamma_y \times 1$; the quantities Γ_x and Γ_y are ratios of lateral widths to the unit fluid depth and are called aspect ratios. Since the fluid is confined by stationary material walls, the velocity vanishes at these walls which provides the following boundary condition on \mathbf{u} :

$$\mathbf{u} = 0 \quad \text{on all walls.} \quad (4)$$

With our rescaled variables, the constant temperature boundary conditions on the bottom and top plates ($z = 0$ and $z = 1$ respectively) are simply

$$T(t, x, y, 0) = 1 \quad \text{and} \quad T(t, x, y, 1) = 0. \quad (5)$$

The temperature field T satisfies an additional boundary condition on the lateral walls which, for this paper, we take to be a no-flux condition corresponding to a perfect thermal insulator

$$\partial_n T = \hat{\mathbf{n}} \cdot \nabla T = 0 \quad \text{on lateral walls,} \quad (6)$$

where $\hat{\mathbf{n}}$ is the normal unit vector at a given point on the wall. However, the code is more general and can treat thermal boundary conditions that interpolate between conducting and insulating sidewalls.

The numerical challenge is to integrate these equations and boundary conditions efficiently and accurately over long time intervals in large cells of simple geometry; boxes and cylinders cover nearly all the experimental cases while a box with periodic sidewalls is useful for comparing with theory. Rayleigh-Bénard convection

is so important that many numerical methods have been developed and tried over the years although, somewhat unfortunately, most of these methods have not been compared with each other to determine which best achieves a practical balance of efficiency, accuracy, ease of programming, and parallel scalability on some specific computer architecture. Because our interest is to study fundamental questions in simple cell geometries, we chose not to use finite element or spectral element methods whose main strengths are the ability to handle irregular boundaries. Because our short term needs are for modest accuracy, simplicity and flexibility of coding, and good parallel scaling on Beowulf-style computers, we chose second-order-accurate finite-difference approximations on Cartesian meshes instead of spectral methods.

Our code uses a traditional time-splitting method in which higher-order linear operators are advanced implicitly in time and lower-order nonlinear terms are advanced explicitly [5], achieving at each time step an overall accuracy of second order in time. The incompressibility condition $\nabla \cdot \mathbf{u} = 0$ is treated by a standard projection method [6] in which the momentum conservation equations are used to update the current velocity $\mathbf{u}(t, \mathbf{x})$ to an intermediate field \mathbf{u}^* that is not divergence free, and then \mathbf{u}^* is "projected" onto a divergence-free field $\mathbf{u}(t + \Delta t, \mathbf{x})$ by solving a Poisson equation for the new pressure field. To advance one time step Δt , four 3D Helmholtz equations and one 3D Poisson equation must be solved with appropriate boundary conditions, and the solution of these linear equations constitute the most time consuming part of the code. For this first generation code, we used FISHPACK fast direct solvers (available through www.netlib.org) which are well suited for modest-aspect-ratio problems on single-processor Alpha workstations. Future codes will use parallel iterative methods which are also better suited for the non-constant-coefficient linear operators that arise in a cylindrical geometry.

Our code was innovative mainly through the use of *colocated* meshes, in which all field values and all operators of field values were evaluated on the same set of mesh points. For two- and three-dimensional fluid simulations of incompressible flow, empirical studies and some analysis have suggested that staggered meshes (in which scalar quantities are stored at the centers of grid boxes while vector components are stored on the faces or vertices of the boxes) were necessary to avoid numerical instabilities associated with the pressure [7]. Our colocated-mesh Boussinesq code proved to be numerically stable which led to a substantial reduction in the effort of writing and validating the code compared to a staggered-mesh code. For lack of space, we refer to our forthcoming paper for further details, e.g., how our code was validated and its efficiency and accuracy as a function of various parameters [5].

Applications

We now report on two preliminary applications of the above convection code. First we try to simulate an intriguing experiment [4] that goes to the heart of how chaotic behavior arises in a continuous medium, here through the occurrence of quasiperiodic states with as many as five incommensurate frequencies. The mystery to understand is the spatial structure of the different oscillations and their dependence on aspect ratio and Rayleigh number. Second, we investigate how the onset of spiral defect chaos state [2] depends on the aspect ratio Γ of a square box, which we increase in small successive increments. Varying the aspect ratio is difficult in laboratory experiments and these calculations demonstrate the usefulness of having quantitatively accurate codes to complement experiments.

Multi-Frequency Dynamics at Intermediate Aspect Ratios

Our first calculation was motivated by the experimental paper of Walden et al [4], which reported in 1984 the unexpected occurrence of spatiotemporal quasiperiodic states in a convecting flow with as many as five incommensurate frequencies. This result seemed to contradict one of the major mathematical insights of the time, a theorem of Newhouse, Ruelle, and Takens [8] which argued that chaotic behavior should be typically observed after at most three successive Hopf bifurcations since quasiperiodic dynamics with three or more incommensurate frequencies can be perturbed infinitesimally to become chaotic. Although the abstract mathematical arguments were difficult to interpret for laboratory experiments and despite clarifications of this theorem by later numerical simulations on simple map systems [9], it is still not understood how a physical continuous medium can develop so many independent oscillations or whether a physical mechanism can be identified for each independent frequency.

To make contact with this experiment, we have carried out the first (to our knowledge) simulations in a box-like domain with parameters nearly identical to those of the experiment. Thus we performed numerical integrations of the 3D Boussinesq equations in a cell of aspect ratio $9.5 \times 4.5 \times 1$, for a fluid with Prandtl number $\sigma = 3.5$ (corresponding to water with a mean temperature of 50°C) and over a comparable range of Rayleigh numbers up to $R = 20R_c$, where $R_c \approx 1708$ is the critical value for the onset of convection in an infinite-aspect-ratio cell. The most poorly justified approximation was our choice of laterally insulating sidewalls Eq. (6) since the real experiment had finitely conducting glass sidewalls between a copper bottom plate and sapphire upper plate. (The thermal diffusivities κ of copper, glass, sapphire, and water are respectively 1.20, 0.004, 0.113, and $0.00147 \text{ cm}^2/\text{sec}$.) A typical run used a resolution of $76 \times 36 \times 8$ points and a constant time step of $\Delta t = 0.001$. A run to collect 65,000 points took approximately 1.5 hours on a Compaq XP1000 workstation using a 667 MHz 264 Alpha chip with a 4 MB cache.

Some representative results are shown in Fig. 1. As the Rayleigh number R is increased in small steps, new incommensurate frequencies appear until, at $R/R_c = 17.5$, 5 incommensurate frequencies are observed just as in the experiment. The fact that these frequencies were incommensurate was supported by plotting (not shown) the ratios of frequencies corresponding to different peaks and observing that these ratios varied smoothly with R , i.e., no mode locking to a rational value took place. The numerical simulations did not

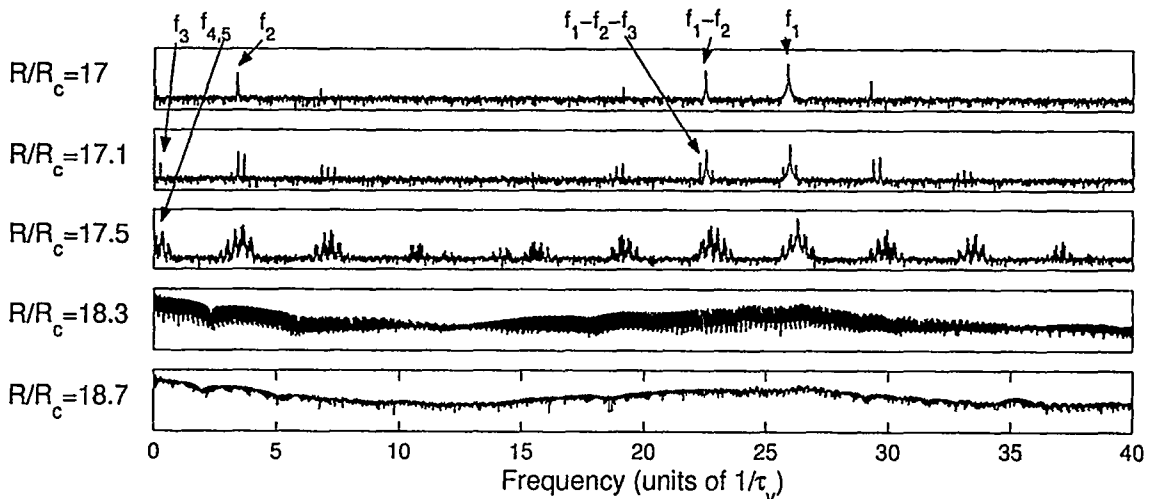


Figure 1: Power spectra $P(f)$ versus frequency f for five values of the Rayleigh number R over the range $17 \leq R/R_c \leq 18.7$ in a cell of aspect ratio $9.5 \times 4.5 \times 1$ and for a fluid of Prandtl number $\sigma = 3.5$. The top three panels show quasiperiodic motion with 2, 3, and 5 incommensurate frequencies respectively. The last two panels show spectra of chaotic dynamics with continuous broad-band features.

reproduce quantitatively the magnitude of the lower frequencies observed in experiment. For example, for the 4-frequency convection state, the simulation has a low frequency peak at $f_4 \approx 0.17$ which is about a factor of three smaller than that observed in the experiment. A first guess is that this discrepancy is a consequence of the convenient but experimentally inaccurate no-heat-flux boundary condition Eq. (6).

In related simulations, we have also explored how the dynamics depended on aspect ratio, a question which is difficult to explore experimentally. Fig. 2 shows several instantaneous convection patterns and the power spectra of the corresponding time-dependent states over the range $9.5 \leq \Gamma_x \leq 10.5$ with Γ_y and R held fixed. A surprising and new result is that small changes in Γ lead to dramatically different patterns and dynamics. Indeed, for the states of Fig. 2 and others not shown over this same range, one can identify time independent, periodic, quasiperiodic (with 3 and 4 frequencies), and chaotic dynamics. The spatiotemporal dynamics is evidently highly sensitive to small changes in the system geometry at these intermediate aspect ratios.

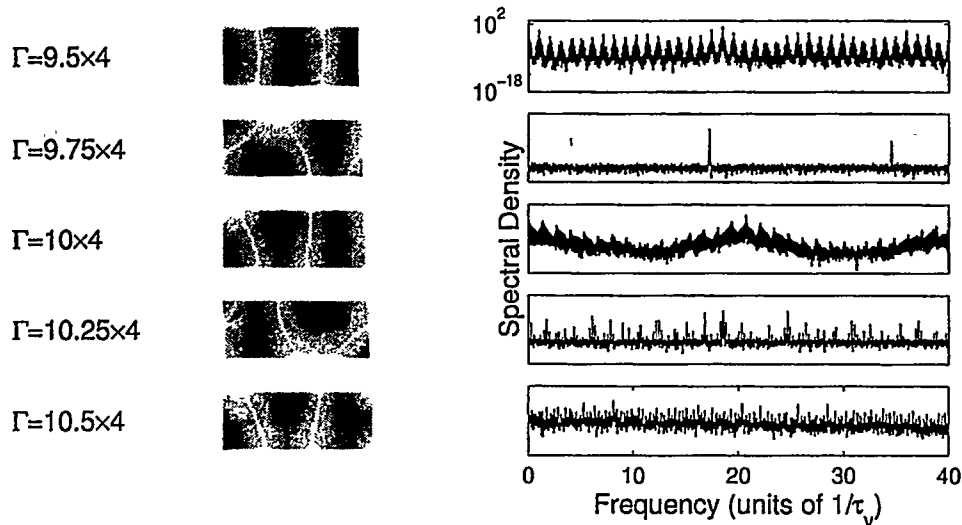


Figure 2: Changes in convection dynamics as the aspect ratio Γ_x is increased in small steps for fixed $\Gamma_y = 4$ and $R = 18R_c$. The left column of plots are instantaneous density plots of the temperature field at the midplane $z = 1/2$ with light regions corresponding to warm fluid, dark regions to cool fluid. The right column of plots are corresponding power spectra $P(f)$ calculated from time series of 65,536 values of the temperature at the midpoint of the cell. Rows 1, 3, and 5 are chaotic, row 2 is periodic, and row 4 is quasiperiodic with three independent frequencies.

Onset of Spiral Chaos

As the technology improved for exploring large-aspect-ratio convection dynamics, experimentalists made a remarkable discovery in 1993 [2] of an intricate spatiotemporal chaotic convecting flow in a cylindrical geometry near onset, a regime that previous experiments in smaller aspect ratios had suggested would show only simple convective patterns, and for which theory predicts that parallel time-independent convection rolls should be stable [10]. This *spiral defect chaos* state (so named because of the unexpected occurrence of rotating spiral structures) remains poorly understood seven years later and is now regarded by many convection researchers to be an especially important example of spatiotemporal chaos to understand. Intriguing and also poorly understood is the experimental observation that spiral defect chaos is observed only when the aspect ratio Γ of the cylindrical cell is sufficiently large, with the radius being at least 40 times the fluid depth.

Using the code described above, we have explored for the onset and properties of spiral defect chaos in finite cells with experimentally realistic lateral boundary conditions and with varying aspect ratio, although for a square rather than cylindrical geometry. Representative results for two different values of the reduced Rayleigh number $\varepsilon = (R - R_c)/R_c$ are shown in Fig. 3. For $\Gamma \leq 24$, the asymptotic dynamics are stationary while time-dependent states are observed for larger Γ , with spirals being observed only for the larger Rayleigh numbers. Spirals appear in square geometries for smaller aspect ratios than those of a cylindrical cell at the same reduced Rayleigh number.

As a first step towards quantifying and analyzing these complex patterns, we have calculated the time-averaged distribution $P(q)$ of local wave numbers q as a function of aspect ratio and Rayleigh number. Following a recent suggestion of Egolf et al [11], we estimated local wave numbers $q(t, x, y)$ from the ratio $-\nabla^2\theta/\theta$ where $\theta = \theta(t, x, y, 1/2)$ is the deviation of the temperature field T from its linear conducting profile, evaluated at the cell midplane $z = 1/2$. The distribution $P(q)$ was then obtained by averaging many instantaneous histograms of q over time. A compilation of the mean wave numbers \bar{q} associated with each wave number distribution is shown in Fig. 4, which shows rather remarkably that the trend for the variation of \bar{q} with R is nearly independent of the aspect ratio, and that \bar{q} decreases roughly linearly with increasing Rayleigh number up to $R/R_c \simeq 2$. Near the value $q - q_0 = -0.8$ (with q_0 the critical wave number at onset),

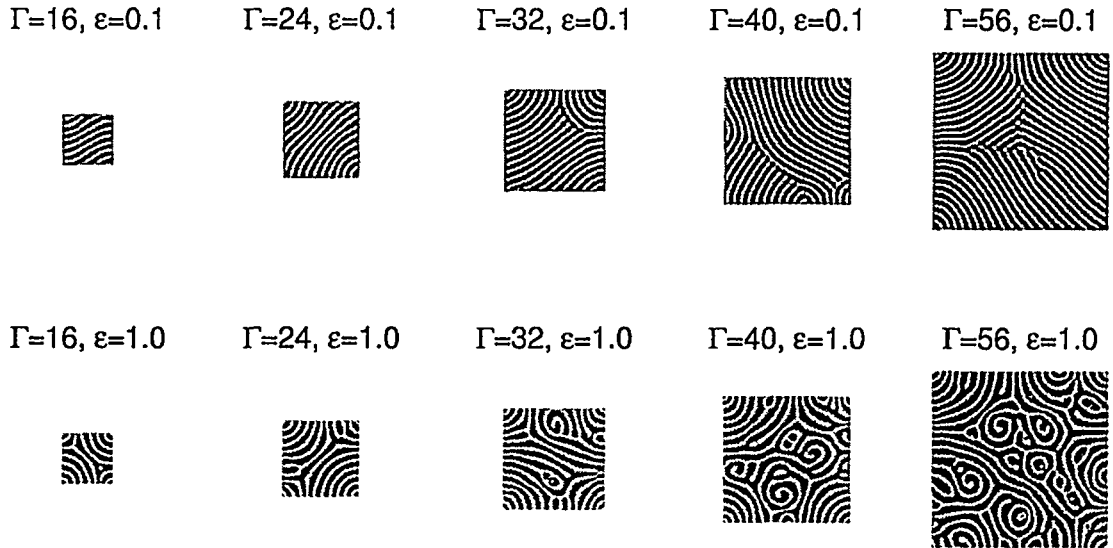


Figure 3: Instantaneous patterns observed in various aspect ratios for two values of the reduced Rayleigh number $\varepsilon = (R - R_c)/R_c$ and for a fixed Prandtl number of $\sigma = 0.96$, corresponding to the compressed CO_2 gas used in the experiments. The first two columns of states are time independent.

there is a dramatic change with \bar{q} becoming essentially independent of R . At this point, spiral defect chaos develops in the larger aspect ratio cells while the smaller cells are chaotic and lack spiral defects.

The average spatial disorder of each pattern can also be quantified by a correlation length ξ , which is defined here to be the inverse of the width of the distribution $P(q)$. The inset in Fig. 4 shows that ξ is also insensitive to the aspect ratio and obeys approximately a power law dependence $\varepsilon^{-1/2}$ which is the same as that predicted by the amplitude equation theory [1] (although the range of Rayleigh numbers in the plot is much larger than the range over which this theory might be expected to hold). A similar trend has again been noticed in cylindrical geometry experiments, although an experiment in a rectangular cell found a divergence at a nonzero value of ε .

The trend of $\bar{q}(\varepsilon)$ in Fig. 4, which has also been observed in cylindrical experiments, is far from that predicted theoretically by Cross and Newell [13], who argued that portions of circular rolls around a “focus singularity” such as those spanning the corners in the cells of Fig. 3 should lead to the selection of the same wave number q_f as that selected in concentric axisymmetric rolls [14]. The discrepancy is particularly striking in the simple structures seen at low values of ε such as Fig. 5, where theory [13] suggests that the focus singularities in the corners should determine the wave number over much of the system. One possible way in which arcs of rolls can act differently than complete circles is that arcs can drive a “mean flow”, which may then modify the wave number distribution. The mean flow is, roughly, the horizontal fluid flow integrated across the depth of the cell and cannot occur in axisymmetric (or straight) roll configurations because of the incompressibility of the fluid. The mean flow is known to be important in producing the skew-varicose instability and in suppressing the zigzag instability for Prandtl numbers of order unity.

Using the detailed knowledge provided by the code of the convection pattern, the wave number distribution, and the mean flow, we are able to assess for the first time the importance of the mean flow in producing the deviations of the measured wave number \bar{q} from q_f . Fig. 5 shows the distribution of the wave number field and corresponding mean flow. In regions towards the center of the cell where the mean flow is small, the wave number is indeed close to the predicted value $q_f = 3.1$. However circulating mean flow patterns develop in the cell corners and the wave numbers there are substantially reduced below q_f . A plot of the distribution $P(q)$ (not shown) indicates in fact that the *largest* q with significant probability is close to q_f but the spread of $P(q)$ to smaller values of q means that the *mean* \bar{q} is considerably below q_f . Given the characteristic form of the mean flows that form in the corners—consisting of two regions of counter-rotating vorticity—an analytic attack on this long standing question is an appropriate next step.

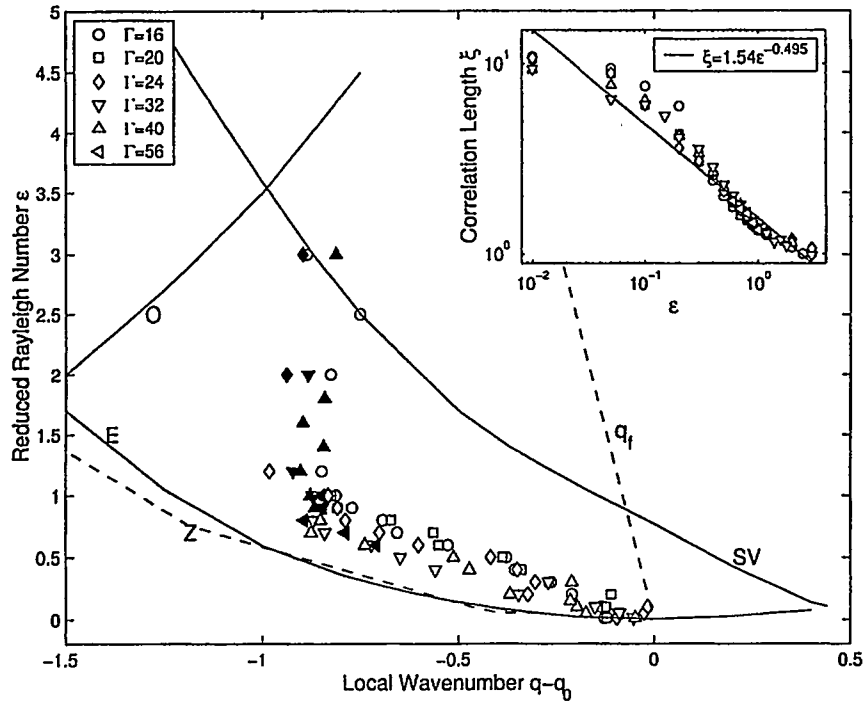


Figure 4: Plot of the deviation $\bar{q} - q_0$ of the mean wave number \bar{q} from the critical wave number $q_0 = 3.117$ as a function of the reduced Rayleigh number ϵ . Also shown are the instability boundaries [12] which limit the range for the ideal roll state in a laterally infinite geometry (SV=skew varicose; O=oscillatory; E=Eckhaus; Z=zigzag), and the wave number $q_f(\epsilon)$ that is selected in axisymmetric rolls. Solid symbols denote states where dynamic spiral defects are observed. The inset shows the correlation length ξ defined as the inverse of the width of the wave number probability distribution $P(q)$. The straight line has a slope 1/2 as would be predicted by the amplitude equation theory near threshold.

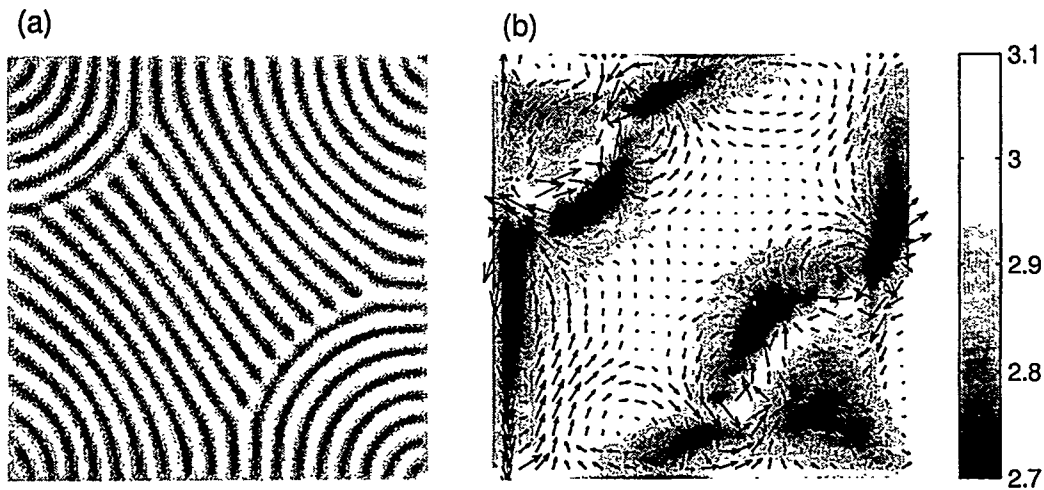


Figure 5: (a) Roll pattern and (b) wave number distribution (gray scale) at $R/R_c = 1.15$ in a cell of aspect ratio $\Gamma = 40$. The corresponding mean flow (arrows) was estimated by integrating the horizontal velocity components of \mathbf{u} vertically over the fluid depth. The maximum Euclidean norm of \mathbf{u} has the value 6.1 in units of d/t_v while the mean flow is much smaller, with a corresponding maximum magnitude of 0.12.

Conclusions

As initial applications of our intermediate- to large-aspect-ratio fluid convection code we have studied two aspects of the onset of chaotic dynamics. In both of these examples the role of the physical boundaries were found to play a vital role –in the intermediate aspect ratio by determining the basic structures about which dynamics develops, and in the large aspect ratio cell where the mean flows that form in the corners of the cell play an important roll in determining the wave number distribution–and so the physical issues are not accessible to previous codes where periodic boundary conditions are used. The preliminary results we present here suggest further directions to explore, both numerically and analytically.

Acknowledgements

This work was supported by the Engineering Research Program of the Office of Basic Energy Sciences at the Department of Energy, Grant DE-FT02-98ER14892. We also thank Paul Kolodner for useful discussions concerning the convection apparatus of Walden et al.

References

- [1] M. C. Cross and P. C. Hohenberg. Pattern formation outside of equilibrium. *Rev. Mod. Phys.*, 65(3):851–1112, 1993.
- [2] Stephen W. Morris, Eberhard Bodenschatz, David S. Cannell, and Guenter Ahlers. Spiral defect chaos in large-aspect-ratio Rayleigh-Bénard convection. *Phys. Rev. Lett.*, 71(13):2026–2029, September 1993.
- [3] W. Decker, W. Pesch, and A. Weber. Spiral defect chaos in Rayleigh-Bénard convection. *Phys. Rev. Lett.*, 73(5):648–651, 1994.
- [4] R. W. Walden, P. Kolodner, A. Passner, and C. M. Surko. Nonchaotic Rayleigh-Bénard convection with four and five incommensurate frequencies. *Phys. Rev. Lett.*, 53:242–245, 1984.
- [5] M. Lai and H. S. Greenside. An Efficient Colocated Mesh Projection Method for Simulating Large-Aspect-Ratio Rayleigh-Bénard Convection. To be submitted to the *Journal of Computational Physics*, 2000.
- [6] John B. Bell, Phillip Colella, and Harland M. Glaz. A second-order projection method for the incompressible Navier-Stokes equations. *J. Comp. Phys.*, 85:257–283, 1989.
- [7] Francis H. Harlow and J. Eddie Welch. Numerical calculation of time-dependent viscous incompressible flow of fluid with free surface. *Phys. Fluids*, 8(12):2182–2189, 1965.
- [8] Edward Ott. *Chaos in Dynamical Systems*. Cambridge U. Press, New York, 1993.
- [9] C. Grebogi, E. Ott, and J. A. Yorke. Attractors on an N -Torus: Quasiperiodicity Versus Chaos. *Physica D*, 15:354, 1985.
- [10] Reha. V. Cakmur, David A. Egolf, Brendan B. Plapp, and Eberhard Bodenschatz. Bistability and competition of spatiotemporal chaotic and fixed point attractors in Rayleigh-Bénard convection. *Phys. Rev. Lett.*, 79(10):1853–1856, 1997.
- [11] David A. Egolf, Llarion V. Melnikov, and Eberhard Bodenschatz. Importance of local pattern properties in spiral defect chaos. *Phys. Rev. Lett.*, 80(15):3228–3231, 1998.
- [12] F. H. Busse. Nonlinear properties of convection. *Rep. Prog. Phys.*, 41:1929–1967, 1978.
- [13] M. C. Cross and A. Newell. Convection patterns in large aspect ratio systems. *Physica*, 10D:299–328, 1984.
- [14] J. C. Buell and I. Catton. Wavenumber selection in large-amplitude axisymmetric convection. *Physics of Fluids*, 29:23–30, 1986.

ENTRAINMENT IN HIGH-VELOCITY, HIGH-TEMPERATURE PLASMA JETS

J. R. Fincke, D. M. Crawford, S. C. Snyder, W. D. Swank, and D. C. Haggard, R. L. Williamson
Idaho National Engineering and Environment Laboratory
PO Box 1625, Idaho Falls, ID, USA 83415-2211

ABSTRACT

The development of a high-velocity, high-temperature argon plasma jet issuing into air has been investigated using a variety of diagnostic techniques. In particular the entrainment of the surrounding air, its effect on the temperature and velocity profiles and the subsequent mixing and dissociation of oxygen has been examined in detail. The total concentration of oxygen and the velocity and temperature profiles in the jet were obtained from an enthalpy probe. Coherent Anti-Stokes Raman Spectroscopy (CARS) was used to measure the concentration and temperature of molecular oxygen. Two-photon Laser Induced Fluorescence (LIF) was used to measure the concentration of atomic oxygen. It was found that both the incompleteness of mixing at the molecular scale and the rate of dissociation and recombination of oxygen have an effect on the observed jet behavior.

INTRODUCTION

The entrainment of cold gas into turbulent, high temperature, and high velocity atmospheric pressure plasma jets dominates their behavior [1]. Entrainment alters the chemical composition and quickly slows and cools the jet. Evidence suggest that entrainment is more of an engulfment or induction phenomena [1-4], rather than gradient driven diffusion. In this description entrainment refers to the process by which the surrounding irrotational fluid is transported into the shear flow. The term mixing refers to mixing at the molecular level. A qualitative conceptual model, which describes the main features of the process, and estimates the important time scales, has been proposed by Broadwell and Briedenthal [5]. The model describes the entrainment and mixing process as a sequence of events initiated by the engulfment or induction of irrotational fluid into the jet shear layer. This initial process is kinematic and not diffusive with the irrotational fluid immediately adjacent to the shear layer participating in the large-scale structure motion of the shear layer long before it has acquired vorticity of its own. These entrained or inducted "lumps" of fluid are subsequently strained and broken down into

smaller and smaller spatial scales or eddies. During this process the interfacial area rapidly increases until the viscous Kolmogorov microscale, λ_0 , is reached. Once λ_0 is reached and the interfacial zones intermingle, molecular diffusion and heat conduction quickly annihilate the local concentration and temperature gradients homogenizing the mixed fluid.

For large Reynolds numbers the time to reach the Kolmogorov scale, $\lambda_0 = k_2 \delta / R_c^{3/4}$, is $\tau_\delta \approx k_1 \delta / \Delta U$, where δ is the thickness of the shear layer, $\Delta U = 1/2 U_{\text{centerline}}$, and k_1 and k_2 are constants. The Reynolds number, $R_c = \Delta U \delta / \nu$, is based on the shear layer thickness and ΔU . The time scale to diffuse across the small scale [5] λ_0 is $\tau_\lambda = \lambda_0 S_c R_c^{-1/2}$ where the Schmidt number S_c is defined as the ratio of kinematic viscosity to mass diffusion coefficient. The other time scale of importance for the formation of a chemical product is the chemical reaction time, or Damkohler number; τ_k / τ_c for the large scales and τ_λ / τ_c for the small scales [6], where τ_c is the chemical reaction time constant. Large Damkohler numbers tend towards mixing limited chemistry while small values tend toward rate limited chemistry.

An intermediate stage can also be associated with diffusive processes, such as molecular mixing or heat conduction that may or may not precede to a significant extent the final stage. The relative importance depends on the relative magnitude of the corresponding molecular diffusivity to that of the kinematic viscosity or the Schmidt number [7]. The corresponding diffusion scale λ_D differs from the Kolmogorov scale by the inverse of the square root of the Schmidt number, $\lambda_D = \lambda_0 S_c^{1/2}$. In particular for chemical reactions between entrained gases in a turbulent shear layer where the Schmidt number is of order unity the time scale for this process is comparable to τ_λ . This intermediate stage, sometimes referred to as infusion, is indistinguishable in gases from the final diffusive dominated process occurring at the Kolmogorov scale. Because of the very large temperature gradients present in high temperature jets, significant heat transfer at the boundaries of cold inducted eddies may occur before the fluid is mixed at the Kolmogorov scale making this intermediate stage process particularly significant. For the case of chemical reaction between the entrained fluid and the shear layer fluid, such as the dissociation of oxygen studied here, this stage of the entrainment process may be very important.

Measurements of plasma velocity, temperature, and composition were obtained using an enthalpy probe integrated with a mass spectrometer [8-10]. Measurements of the concentration of atomic oxygen were obtained using two-photon laser induced fluorescence (LIF). Coherent anti-Stokes Raman Spectroscopy (CARS) was used to determine the temperature of the entrained molecular oxygen and to estimate the local molecular concentration. In the following sections the experiment is described, the measurement techniques detailed, and the general features of the flow field examined. These results will ultimately be used to benchmark a comprehensive computational model of the entire process that is under development. All testing was conducted using a commercial direct current plasma torch. The Miller SG-100 plasma torch was operated at 900 A and 40 V, with a standard anode and cathode arrangement (Miller #165 and #129 respectively). The torch nozzle exit diameter was 8.0 mm. The argon flow rate was 35.4 slm. The measured thermal efficiency of the torch under these operating conditions was 27 %, and the atmospheric pressure was 85.5 kpa.

ENTHALPY PROBE

Originally developed in the 1960s, enthalpy probes [11,12] have enjoyed renewed application to thermal plasma processing problems [13-15]. Their range of application has been extended by integration with a mass spectrometer for measurement of gas composition [8], and their performance has been validated by comparison to laser scattering measurements [9,10]. The enthalpy probe is a water-jacketed gas sampling and stagnation pressure probe from which the enthalpy, temperature, and velocity of a hot flowing gas can be derived once the composition is known. The probe used is copper with an outside diameter of 4.76 mm and a hemispherical tip. Probe survivability in high temperature and high velocity flows dictates a large probe size. The calorimetric method used to determine gas enthalpy and hence temperature depends heavily on a "tare" measurement. Observation of the coolant temperature rise and flow rate are made in the absence of gas flow through the inner diameter of the probe. Gas is then caused to flow and the same coolant measurements are repeated, together with measurements of the gas flow rate through the probe and gas temperature at the probe exit. The rate of heat removal from the gas sample is thus given by the difference between the measured delta of cooling water inlet and outlet temperatures,

$$\dot{m}_g (h_\infty - h_c) = \dot{m}_{cw} C_p [(\Delta T_{cw})_{gas\ flow} - (\Delta T_{cw})_{no\ gas\ flow}]$$

where m_g = gas sample mass flow rate, m_{cw} = cooling water mass flow rate, h_∞ = unknown gas enthalpy at the probe entrance, h_c = gas enthalpy at the probe exit thermocouple, C_p = cooling water specific heat, and ΔT_{cw} = cooling water temperature rise. The unknown gas enthalpy h_∞ at the probe tip is now uniquely determined, provided that the gas sample flow rate and the gas enthalpy at the probe exit are known. The exit gas sample enthalpy is determined from the measured temperature and the gas sample flow rate is measured via a sonic orifice. While the probe is in the "no gas flow" mode the stagnation pressure is measured. The gas mixture composition is required to determine the gas sample flow rate and to relate measured enthalpy and stagnation pressure to thermodynamic properties and gas velocity. Composition is obtained by a quadrupole mass spectrometer interfaced to the enthalpy probe via a differentially pumped vacuum system. For low Mach number flows the free stream velocity, U , is obtained from $U = [2(P_t - P_\infty) / \rho_\infty]^{1/2}$ where P_t is the stagnation pressure and P_∞ is the ambient or static pressure. The density ρ_∞ is a function of the freestream enthalpy, pressure and gas composition. Centerline velocity and temperature data derived from enthalpy probe measurements are shown in Figures 1 and 2. The axial coordinate is measured from the face of the torch. Particularly noticeable is the rapid increase in air content and the associated slowing and cooling of the jet.

COHERENT ANTI-STOKES RAMAN SPECTROSCOPY

Non-intrusive optical diagnostic techniques such as CARS, developed for combustion research, are also applicable in thermal plasma flow fields [14]. CARS has the advantage of high conversion efficiency, a laser-like coherent signal beam for high collection efficiency, excellent

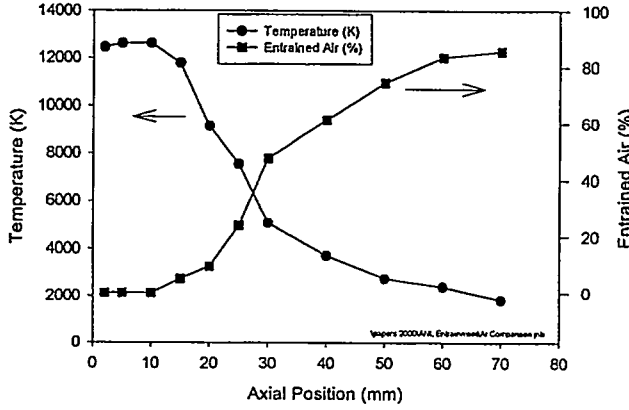


Figure 1. Temperature comparisons, showing effect of gas and liquid injection.

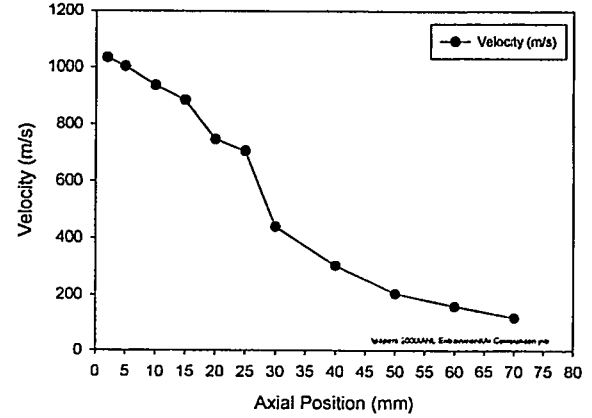


Figure 2. Velocity comparisons, showing effect of gas and liquid injection.

fluorescence and luminosity discrimination, and high spatial and temporal resolution. The technique is applicable to the measurement of the concentration of any Raman active species.

The theory of CARS and its application as a combustion diagnostic are detailed in [7]. A CARS signal is generated when two laser beams at frequency ω_1 , (termed the pump beams) and one laser beam at frequency ω_2 (termed the Stokes beam) interact through the third-order nonlinear susceptibility of the medium $\chi^{(3)}$. This interaction generates an oscillating polarization and thus coherent (laser like) radiation at frequency $\omega_3=2\omega_1-\omega_2$. The third order susceptibility is a complex quantity and is composed of a resonant (χ_r) and a non-resonant (χ_n) component. The non-resonant component is proportional to the number density of the species present and is generally a slowly varying function of wavelength.

In general, the pump (ω_1) and Stokes radiation fields (ω_2) have a finite line-width. The CARS signal is then proportional to

$$I_3(\omega_3) \propto \int I_1(\omega') d\omega' \int I_1(\omega'') I_2(\omega'+\omega''-\omega_3) \left| \chi^{(3)}(\omega_3 - \omega'') \right|^2 d\omega''.$$

Because our pump beam is transform limited in spectral bandwidth (≈ 100 MHz) the cross-coherence effects present when multi-mode YAG lasers are used have been neglected. Furthermore it is assumed that the CARS lines are superimposed without interaction (isolated line approximation) and are homogeneously broadened. Normalizing $\bar{\chi}_r = \chi_r^{(3)}/n$ and $\bar{\chi}_n = \chi_n^{(3)}/n_0$ and noting that $\bar{\chi}_r = \text{Re} \chi_r + i \text{Im} \chi_r$ and that $\bar{\chi}_n$ is a real quantity, $I_3(\omega_3)$ then, disregarding the convolution, is $I_3(\omega_3) \propto \left((n_0 \bar{\chi}_n)^2 + 2n_0 \bar{\chi}_n n \text{Re} \bar{\chi}_r + (n |\bar{\chi}_r|^2) \right) I_1^2 I_2$. For the case in which the non-resonant background is insignificant or is suppressed by choosing certain polarizations of the pump and probe beams (polarized CARS) then $I_3 \propto n^2 |\bar{\chi}_r|^2 I_1^2 I_2$. The particle density is obtained by absolute intensity measurement of the CARS signal. The temperature is

determined from the relative vibrational and rotational populations $n(v,j)$. A typical single shot Q-branch CARS oxygen spectra taken at 1000 K is shown in Figure 3. Overlaid with the experimental data is a theoretical spectra calculated using a modified version of the CARSFT [16] computer code. The feature between 579.0 and 579.2 nm is the so called hot band, originating from the $v=2$ to $v=1$ rotational-vibrational transitions. The rotational temperature is determined by fitting the theoretical distribution to the data with temperature as a parameter. The particle density measurement, which is dependent upon measurement of the absolute intensity of the CARS signal, is complicated by intensity fluctuations of the lasers and changes in beam overlap, while the temperature measurement is dependent only on relative measurements and is less affected.

Figure 4 compares the rotational temperature of molecular oxygen obtained from the CARS measurement taken on the centerline of the jet. For locations closer to the torch face than 30 mm the concentration of molecular oxygen is insufficient to yield a CARS signal. As is evident in the plot the measured temperatures are significantly less than the mixture temperatures obtained from the enthalpy probe. This indicates that significant amounts of relatively cold air are rapidly inducted deep into the jet flow. These cold eddies have not yet been fully mixed and equilibrated with the hot plasma gas. At 60 mm the mixing process is relatively complete and the two temperature measurements converge.

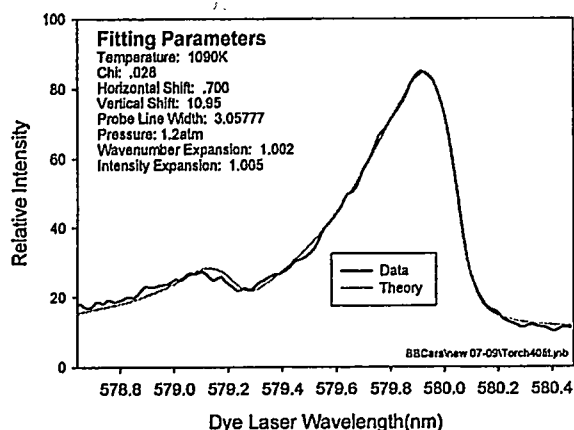


Figure 3. CARS O_2 spectrum at approximately 1000 K.

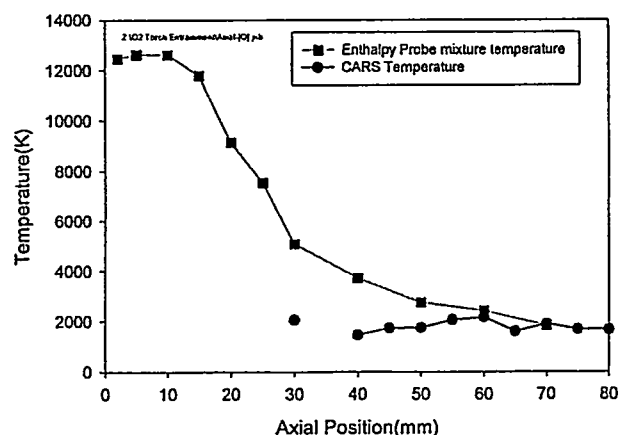


Figure 4. Comparison of CARS O_2 temperature and enthalpy probe mixture temperature.

TWO PHOTON LASER INDUCED FLUORESCENCE

Multiphoton excitation techniques are required for laser induced fluorescence monitoring of the concentration of light atoms such as atomic oxygen [17-19]. Multiphoton excitation allows the creation, from the ground state, of observable populations of excited state O atoms. A

simplified energy level diagram for O is shown in Figure 5. Two 225 nm photons excite the ground $2p^3P$ state to the $3p^3P$ state. The fluorescence signal at 844 nm results from the $2p^3P$ to $3s^3S$ transition. The laser used is a Nd:YAG pumped dye. The fundamental of the dye is doubled and mixed with the $1.06\ \mu\text{m}$ fundamental from the YAG in a KDP crystal yielding 1 mJ of 225 nm light. The two-photon LIF measurement is complicated by the extremely high quenching rates of the laser produced excited state. The observed lifetime of the two-photon produced excited state ($3p^3P$) is less than 2 ns as compared to its natural undisturbed lifetime of 35 ns, Figure 6.

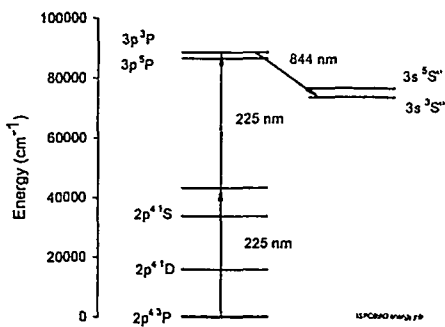


Figure 5. Simplified atomic oxygen energy level diagram.

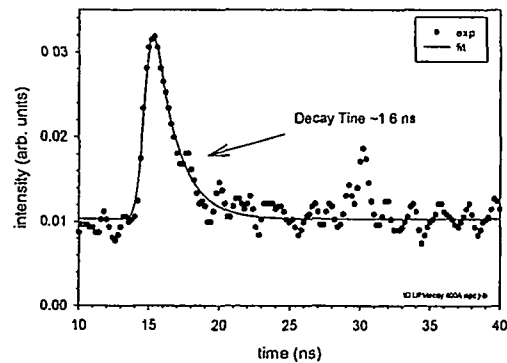


Figure 6. Time resolved fluorescence signal.

The measured centerline axial distribution of atomic oxygen is shown in Figure 7. The decay time (quench rate) of the LIF signal is approximately constant over the extent of the flow field, hence the intensity of the LIF signal is approximately proportional to the atomic oxygen concentration. Also plotted in Figure 7 is the amount of molecular oxygen calculated as the difference between the total amount of oxygen measured by the enthalpy probe and the LIF measurement of atomic oxygen. The CARS measurement of molecular O_2 is also plotted. Much of the variation in the CARS signal is due to laser intensity drift, thus this plot illustrates the limitation of CARS in the measurement of concentration. The same data is also shown in Figure 8 along with the calculated amounts of atomic and molecular oxygen that would be present if the mixture were in equilibrium at the temperature measured by the enthalpy probe. In general the dissociation of molecular oxygen lags the equilibrium in the hot regions of the jet and the recombination lags the apparent cooling of the jet. The fundamental question is which phenomena account for the observations, is the process mixing limited, or does the rate of chemical reaction, dissociation, and recombination account for the observations.

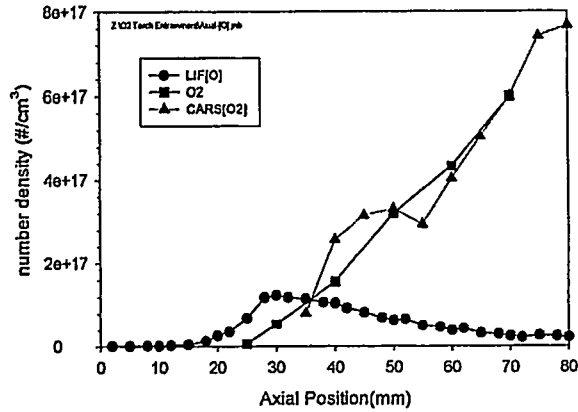


Figure 7. Atomic oxygen concentrations measured by LIF and molecular oxygen concentration obtained from CARS and enthalpy probe measurements.

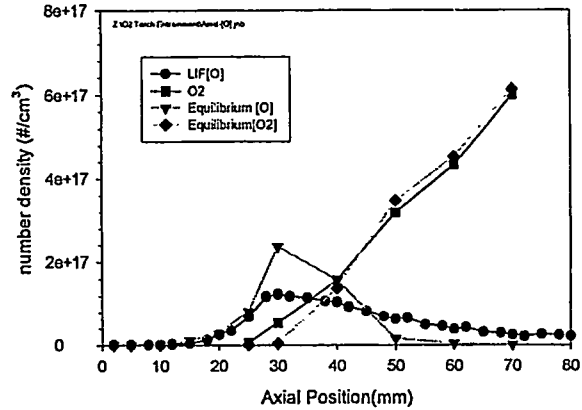


Figure 8. Measured and equilibrium concentrations of atomic and molecular oxygen.

DISCUSSION

The dissociation reaction for oxygen is $O_2 + M \rightleftharpoons O + O + M$ where $M = Ar, He, O_2, N_2, e^-, \dots$. Initially the time constant for this reactions is approximately $\tau_d(Ar) = 1/(2[Ar]k_D)$ where the reaction rate is $k_D(Ar) = 1.6 \times 10^{14} \exp(-54245/T)$ [19]. The time constant for dissociation τ_d is on the order of 100 μs at 6000 K. The mixing time scales estimated from the model of Broadwell and Breidenthal [5] are $\tau_k = 20 \mu s$ and $\tau_\lambda = 10 \mu s$ in the jet near field. With respect to the data in Figures 2 and 4 the absolute upper limit on the time scale for mixing is on the order of $\tau \approx .005 \text{ m} / 500 \text{ m/s}$ or 100 μs consistent with the estimates. The corresponding Damkohler numbers are $\tau_k/\tau_c = 0.2$ and $\tau_\lambda/\tau_c = 0.1$. Thus the entrainment and mixing processes and the chemical reaction time have similar time scales. This is consistent with the apparent incompleteness of mixing illustrated by the temperature data in Figure 4 where large scale inhomogeneities still persist well downstream in the flow field and contribute to the apparent deviations from equilibrium. At the same time the recombination process (the reverse dissociation reaction) takes place at a relatively low temperature, on the order of 2000 K. At this temperature the time constant for recombination is on the order of 1 ms suggesting a greater influence of the rate of reaction. Additional experimental work and modeling are underway which will help to clarify the observed phenomena.

ACKNOWLEDGEMENT

This work was supported by the U. S. Department of Energy, Office of Energy Research, Office of Basic Energy Sciences, Engineering Research Program, under Contract No. DE-AC07-99ID13727.

REFERENCES

1. E. Pfender, J. Fincke, and R. Spores, "Entrainment of Cold Gas into Thermal Plasma Jets," *Plasma Chemistry and Plasma Processing*, 11, pp. 529-543 (1991).
2. J. R. Fincke, R. Rodriguez, and C. G. Pentecost, "Coherent Anti-Stokes Raman Spectroscopic Measurement of Air Entrainment in Argon Plasma Jets, *Plasma Processing and Synthesis of Materials III*, Materials Research Society Symposia Proceedings Vol. 190, San Francisco, CA (1990).
3. J. R. Fincke, R. Rodriguez, and C. G. Pentecost, "Measurement of Air Entrainment in Plasma Jets," *Proc. of the 1990 National Thermal Spray Conference*, Long Beach, CA, ASM International, pp. 45-48 (1990).
4. R. Spores and E. Pfender, Flow Structure of a Turbulent Plasma Jet," *Proc. of the 1988 National Thermal Spray Conference*, Cincinnati, ASM International, pp. 85-92 (1988).
5. J. E. Broadwell and R. E. Breidenthal, "A Simple Model of Mixing and Chemical Reaction in a Turbulent Shear Layer," *J. Fluid Mech.* 125, pp. 397-410 (1982).
6. M. G. Mungal and P. E. Dimotakis, "Mixing and Combustion with Low Heat Release in a Turbulent Shear Layer," *J. Fluid Mech.* 148, pp. 349-382 (1984).
7. P. E. Dimotakis, "Two-Dimensional Shear-Layer Entrainment," *AIAA Journal*, 24, pp. 1791-1796 (1986).
8. W. D. Swank, J. R. Fincke, and D. C. Haggard, *Rev. Sci. Instr.*, 64, 56 (1993).
9. J. R. Fincke, S. C. Snyder, and W. D. Swank, and D. C. Haggard, "Comparison of Enthalpy Probe and Laser Light Scattering Measurement of Thermal Plasma Temperatures and Velocities," *Review of Scientific Instruments*, 64, pp. 711-718 (1993).
10. J. R. Fincke, W. Swank, and D. Haggard, "Enthalpy Probe Performance in Compressible Thermal Plasma Jets," *Review of Scientific Instruments*, 64, pp. 3585-3593 (1993).
11. Grey, J., *ISA Transactions*, 4, pp. 102-115 (1965).
12. Grey, J., P.F. Jacobs, and M.P. Sherman, *Review of Scientific Instruments*, 33, pp. 738-741 (1962).
13. Brossa, M. and Pfender, E., *Plasma Chemistry and Plasma Processing*, 8, pp. 75-90 (1988).
14. Fincke, J. R. and Pentecost, C. G., "Laminar to Turbulent Transition in Thermal Plasma Jets" *Heat Transfer in Thermal Plasma Processing, HTD-Vol. 161*, K. Etemadi and J. Mostaghimi, Eds, ASME, New York, pp. 101-106 (1991).
15. Levenson, M. D., *Introduction to Nonlinear Laser Spectroscopy*, Academic Press, New York, 1982.
16. Palmer, R. E, SAND89-8206, Sandia National Laboratories, Livermore, CA (1989).
17. Bischel, W. K., Perry, B. E., and Crosley, D. R., *Chemical Physics Letters*, 82, pp. 85-88 (1981)
18. DiMauro, L. F., Gottscho, R. A., and Miller, T. A., *J. Appl. Phys*, 56, pp. 2007-2011 (1984).
19. Alden, M., and Westblom, U., *Optics Letters*, 14, pp. 305-307 (1989).
18. W. C. Gardiner, ed., *Combustion Chemistry*, Springer-Verlag, New York, (1984).

**FILM COOLING IN A PULSATING STREAM:
RECENT RESULTS FOR LAMINAR AND TURBULENT WALL JET**

H. Fasel, A. Ortega, I. J. Wygnanski
Department of Aerospace and Mechanical Engineering,
The University of Arizona,
Tucson AZ 85721
USA

ABSTRACT

The heat transfer in a forced laminar, transitional, and turbulent wall jet was investigated with a combined theoretical, experimental, and computational approach. When forcing is introduced into the laminar wall jet, two staggered rows of vortical disturbances develop. At high amplitudes, these structures increase the mixing within the wall jet, which in turn increases the spreading rate and reduces the skin friction. In addition, the large structures entrain cold fluid from the ambient, and hot fluid is convected away from the wall, which leads to an increase in the effective thermal diffusion. It is found that forcing both the principal and subharmonic modes is most efficient. Experimental investigations of the turbulent wall jet show that forcing at all frequencies generally decreases the wall friction because the growth rate of the jet increases. The decrease in wall friction does not seem to have a comparable effect on the wall heat transfer. This is possibly because the outer shear layer vortices that dominate the flow when forcing is introduced do not necessarily produce the small scale turbulence in the inner region that is so important in scalar transport. Preliminary computational investigations of the turbulent wall jet show that the turbulence model is capable of predicting the turbulent mean flow accurately. Qualitatively, the effect of the structures on the turbulent flow is very similar to the laminar flow.

NOMENCLATURE

Re_j	Reynolds number measured at exit plane $= \rho U_j d / \mu$	Y_m	maximum normal distance from the wall (for the integration domain), m
T	local mean temperature, K	c_p	specific heat of air at free-stream, J/kg-K
T_o	free-stream temperature, K	d	wall jet slot width, m
T_w	wall temperature, K	k	thermal conductivity, W/m-K
U	local streamwise mean velocity, m/s	\dot{m}	mass flow rate, kg/s
U_j	jet exit velocity, m/s	t'	fluctuating temperature, K
U_m	local maximum streamwise velocity, m/s	u'	fluctuating streamwise velocity, m/s
U_o	free-stream velocity, m/s	x, y	coordinates, m

Greek symbols

δ	denotes boundary layer thickness, m
δ_v	local hydrodynamic boundary layer thickness, m
δ_t	local thermal boundary layer thickness, m
μ	free-stream dynamic viscosity, N-s/m ²
ρ	free-stream density, kg/m ³

Subscripts

j	jet exit plane
m	maximum
o	free-stream
t	thermal
v	hydrodynamic
w	wall

INTRODUCTION

Along with the boundary layer and the free jet, the wall jet is one of the most important of all flows. The wall jet is a fluid jet introduced tangentially along a surface. The free-stream can either be co-flowing or quiescent and the characteristics of the flow are strongly related to the ratio of the jet velocity to the free-stream velocity. Wall jets have important technological applications such as in film cooling of gas turbine components. In film cooling, a turbulent wall jet is used to shield blades and other surfaces exposed to high temperature free-stream flow. In this multiyear investigation, we are investigating the fundamental mechanisms by which the transport of heat to or from a surface may be enhanced or suppressed by exploiting the naturally occurring instabilities of the flow. We have chosen to focus on a strong laminar, transitional, and turbulent wall jet flow since it exhibits characteristics of both free shear layers and boundary layers that make it particularly susceptible to external excitation. It is thus an ideal flow for fundamental study of heat transfer control by external forcing.

RESULTS FOR THE LAMINAR WALL JET

By a combined experimental and theoretical approach, we previously showed that selective forcing of the laminar and transitional wall jet at its dominant instability modes produced profound changes in the momentum and heat transfer from an isothermal wall. The strong wall jet can be viewed as a combination of a boundary layer (near the wall) and a free shear layer further away from the wall. These two basic flow types exhibit very different stability characteristics, a fact that can be exploited to alter the mean flow by introducing controlled perturbations at specific frequencies and at large amplitudes. The linear stability characteristics of the laminar jet have now been well established, Likhachev et al. (1998) and experimentally confirmed, Likhachev et al. (1999), Quintana et al. (1997). We now have substantial experimental evidence that suggests that forcing with a frequency for which, according to linear stability theory, the boundary layer mode is unstable, is much more effective than forcing the shear layer mode. For the laminar wall jet, the experiments definitively established that forcing the inner boundary layer mode at levels of only 2%, the skin friction can be reduced by as much as 65% and, for the same flow, the wall heat flux can be increased by 45%, Quintana et al. (1997).

Substantial progress has been made in applying Direct Numerical Simulation (DNS) to the laminar wall jet, Seidel and Fasel (2000). Our understanding of the physical mechanisms leading to the profound changes in the momentum and heat transfer has been greatly enhanced. DNS computations were conducted based on the incompressible Navier-Stokes equations solved in the vorticity-velocity formulation in conjunction with the energy equation. A 4th-order accurate Runge-Kutta method was used for the time integration. For the spatial discretization, 4th-order accurate compact differences were used in both the x- and y-directions. The solution procedure of the viscous terms in the vorticity transport equations was extensively modified to facilitate the introduction of a wide variety of turbulence models. For the results shown here, an equidistant grid in the x-direction was used. In the wall normal direction, grid points were clustered near the wall to resolve the steep gradients.

Before applying the codes to extensive simulations of our laboratory experiments, the code was tested and validated to demonstrate its ability to efficiently obtain accurate results. After computing the undisturbed wall jet mean flow, disturbances were introduced into the flow field by periodic blowing and suction through a slot in the wall near the inflow boundary. At low disturbance amplitude levels, the results of the computations showed excellent agreement with results from linear stability theory. Increasing the disturbance amplitude caused a mean flow distortion due to nonlinear interactions. As in the experimental investigations, two frequencies were investigated, $\beta_j =$ (the shear layer mode), and $\beta_j =$ (the boundary layer mode).

Case	Case01	Case02	Case03	Case04	Case05	Case06	Case07
A_f/U_f	5×10^{-4}	1×10^{-2}	1.5×10^{-2}	1×10^{-2}	1×10^{-2}	1.5×10^{-2}	1.5×10^{-2}
A_s/U_s	-	-	-	1×10^{-3}	1×10^{-2}	1×10^{-3}	1×10^{-3}

Table 1 Disturbance amplitudes for the fundamental ($b_j=0.094$) and the subharmonic ($b_j=0.047$) frequency

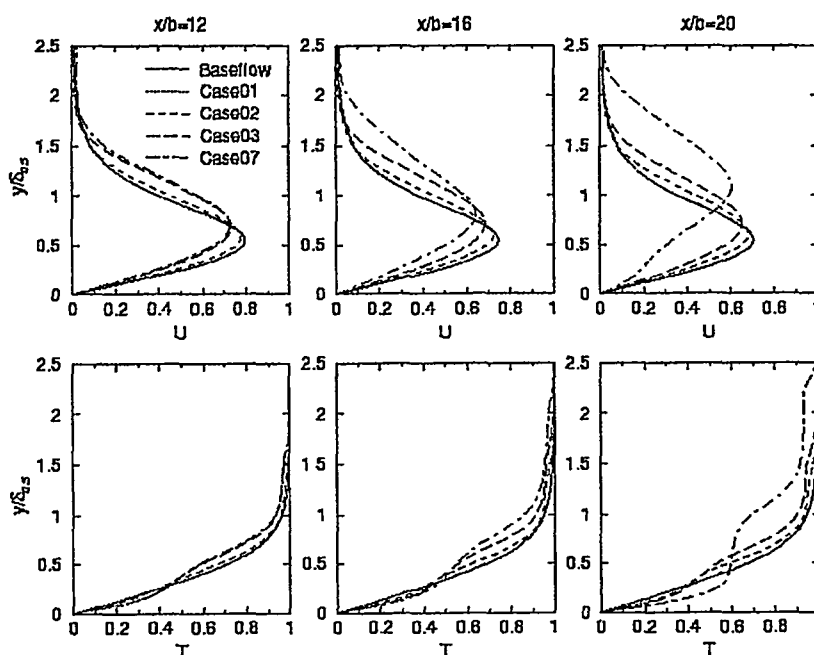


Figure 1. Comparison of mean flow distortion of u-velocity and temperature for different forcing amplitudes.

Forcing the shear layer mode does not show a significant distortion of the mean flow profiles. In contrast, forcing the boundary layer mode has a pronounced effect on the mean flow profiles. The top three graphs in Fig. 1 show the mean velocity profiles. Clearly, the disturbances cause a reduction of the local maximum velocity and the displacement of the location of maximum velocity away from the wall. Both changes of the mean flow profile contribute to the significant reduction in skin friction. The mean temperature profile is shown in the bottom three graphs in Fig. 1. When large amplitude disturbances are

introduced into the flow, the mean temperature profile develops an inflection point near the wall, which results in an increase in the wall heat transfer. Even though forcing with $b_j=0.094$ has a significant effect on the mean flow, the reduction in skin friction and the increase in heat transfer is not nearly as large as our experiments suggest. Scrutinizing the experimental power spectra, the emergence of the subharmonic was observed. This prompted us to introduce forcing at the subharmonic frequency in addition to the fundamental frequency (see Table 1 Cases 04 - 07). Figure 1 shows that with this subharmonic, the mean flow distortion is significantly increased. The spreading rate of the wall jet increases dramatically and the inflection point in the temperature profile becomes more pronounced. The effect of forcing on the near wall mean profiles can be seen more clearly in the change of the analogy factor in the Reynolds analogy, $2St/C_f$. This quantity is plotted in Fig. 2 as a function of downstream distance. The graph shows that only if the amplitude of the subharmonic disturbance is sufficiently high can a mean flow distortion comparable to the experiments be achieved. This clearly shows that it is not the amplitude of the fundamental itself, but rather the subharmonic resonance that results in the significant mean flow distortion observed in the experiments.

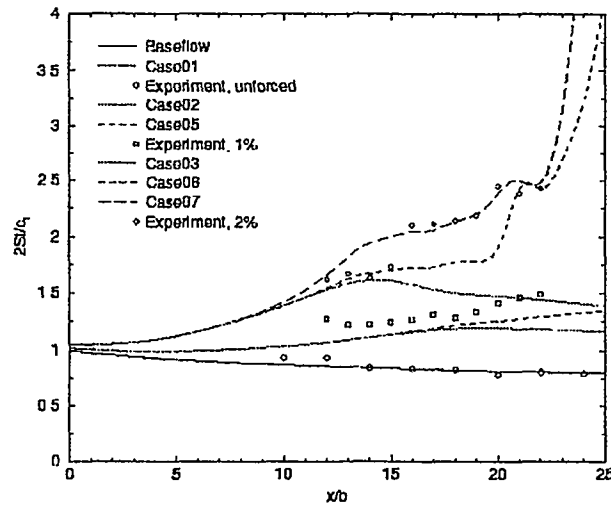


Figure 2. Analogy factor for $b_j=0.094$. See Table 1 for explanation of different cases.

To qualitatively analyze the effect of forcing, the size and location of the large structures is shown in Fig. 3 for different forcing amplitudes. Color contours show the temperature distribution and the contours lines identify vortical structures using the λ_2 criterion by Jeong & Hussain (1995). For comparison, Fig 3(a) shows the undisturbed mean flow. Note that the x- and y-directions are scaled with the nozzle height b to show the spreading of the wall jet in the streamwise direction. If only single frequency disturbances are introduced, Figure 3(b), a very regular, staggered double row of vortices develops. In addition, the figure shows that the temperature distribution is governed by the local, unsteady convection. The structures near the wall turn clockwise, convecting high temperature fluid away from the wall on the upstream side while convecting low temperature fluid towards the wall on the downstream side. The outer row of vortices, turning counterclockwise, enhances this flow pattern. If, in addition, subharmonic forcing is introduced, vortex pairing occurs, Fig. 3(c). This leads to a doubling of the size of the structures, significant thickening of the wall jet, and consequently an increase in heat transfer. Increasing the amplitude of the subharmonic moves the vortex pairing upstream, Figure 3(d).

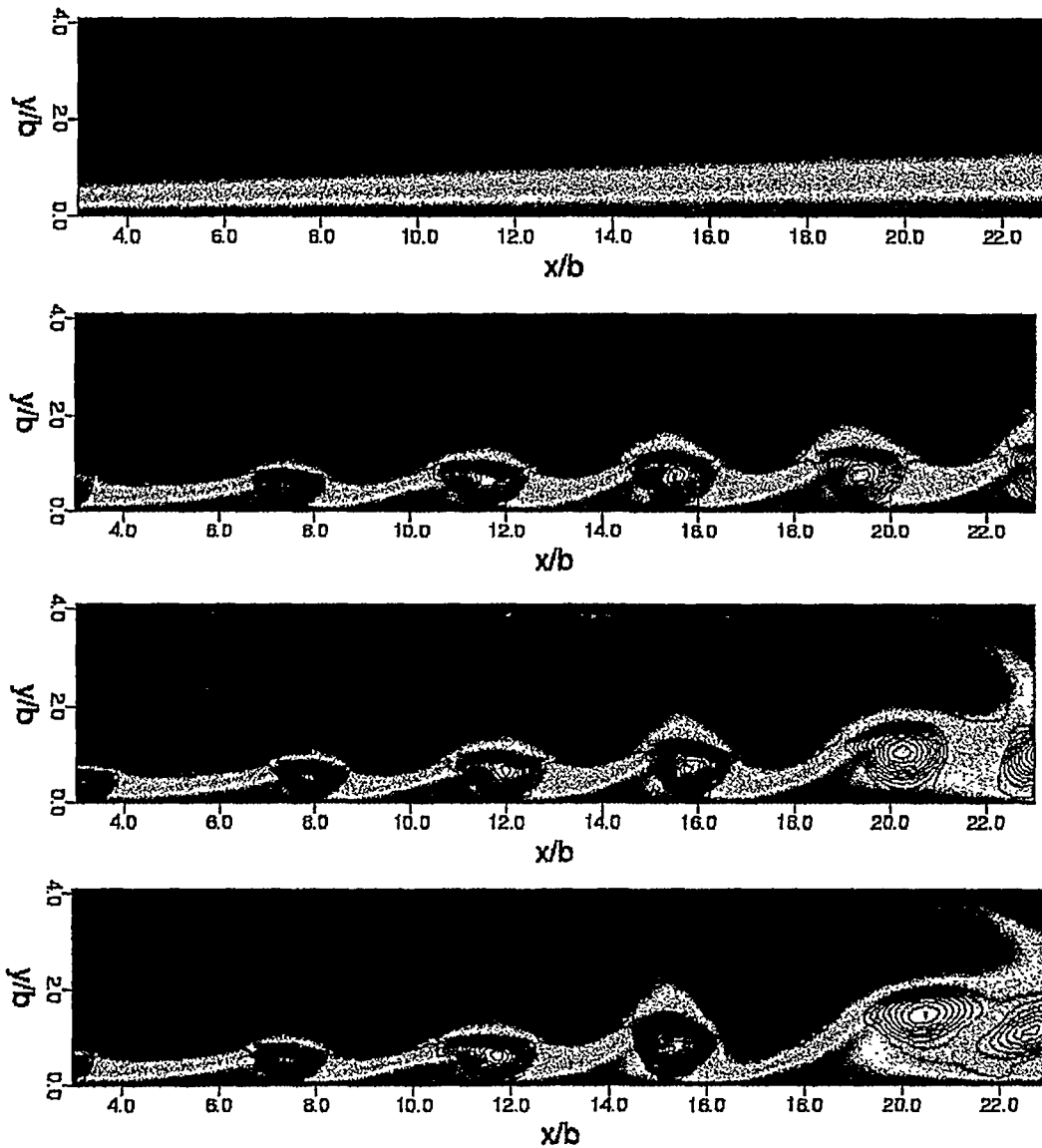


Figure 3. Instantaneous temperature distribution and structures in the flow field. a) Undisturbed base flow, b) Case03, c) Case06, d) Case07.

The effect of the large structures in the flow can be described quantitatively by a local increase in viscosity and thermal conductivity. Typically, these quantities are written as a Reynolds stress, $\overline{u'v'}$, and an eddy thermal diffusivity, $\overline{v't'}$. A comparison of both quantities is shown in Fig. 4. The agreement between the three results is very good. The figure shows negative Reynolds stress near the wall, which is another manifestation of the skin friction reduction due to the structures in the flow field. In the right graphs, the eddy thermal diffusivity is shown. The strong peak near the wall coincides with the reduced temperature gradient around the inflection point in the temperature profile. These results clearly demonstrate that the large structures in the flow are responsible for the changes in skin friction as well as wall heat transfer.

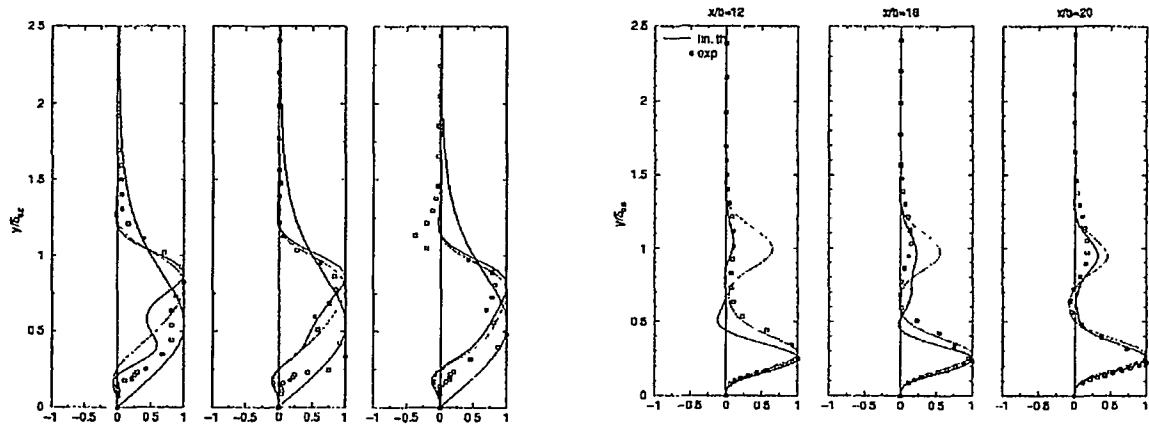


Figure 4. Normalized $\overline{u'v'}$ (left) and $\overline{v't'}$ (right), Case01. Comparison of simulations (- - -), linear theory (...), and experiments (\square).

The fact that the time mean wall shear stress was reduced while the time mean heat transfer was increased is a powerful refutation of the Reynolds analogy for steady flows and points out that intelligent control of convective flows may have a profound impact on rates of transport. In some cases, it may be possible that those transport rates may be significantly influenced while minimizing the penalty usually associated with the pressure drop in a heat transfer device. We next turn our attention to the turbulent wall jet which has greater application but also significantly greater challenges than the laminar jet.

THE STRONG TURBULENT WALL JET

The strong turbulent wall jet is characterized by having a mean jet velocity to free stream velocity ratio greater than about two. The heat transfer in the steady turbulent wall jet has been extensively studied. Seban (1960) and Seban and Back (1961) measured the heat transfer coefficient and the effectiveness for the wall jet with variable slot heights and mass-velocity ratios. It was found that, for mass-velocity ratios of less than unity (weak wall jet), the effectiveness followed a power law decay with downstream distance. The power depended on blowing ratio. For mass-velocity ratios of greater than unity, the heat transfer coefficient could be expressed simply in terms of the slot Reynolds number and the relative downstream distance of the slot. This simple behavior of heat transfer coefficient arose from its primary dependence on the flow immediately adjacent to the wall. In contrast, the effectiveness was related to the velocity distribution in the external part of the boundary layer, between the velocity maximum and the free-stream value, and this distribution depended more critically on the blowing ratio and system parameters. Myers et al (1963a,b) predicted the maximum velocity decay, jet thickness, and the shear stress, and compared with those results analyzed by momentum-integral methods. Myers et al (1963b) studied heat transfer under the condition of a step change in wall temperature with jet Reynolds numbers ranging from 16,600 to 38,100. Mitachi et al (1974) reviewed some of these investigations and proposed an analytical solution to the temperature field using a mixing length turbulence model. Under the condition of constant heat flux, Nizou (1981) attempted to supplement the relation between heat transfer and skin friction for turbulent wall jets. He found that St/C_f increased slightly along with X/b , hence confirming the applicability of the Reynolds-Colburn analogy.

The use of externally introduced forcing in the turbulent wall jet was demonstrated by Katz et al (1992). They excited the turbulent wall jet by a loud speaker at different frequencies and amplitudes. They found that forcing had no appreciable effect on the rate of spread of the jet nor on the decay of its maximum velocity, but this external excitation caused a significant local reduction of skin friction, and enhanced the two-dimensionality and periodicity of the coherent motion. For a turbulent wall jet with an external freestream, Zhou et al (1993a) summarized their experimental data, together with other available data from the literature, and collapsed them onto a set of universal curves independent of Re and the thickness of the upstream boundary layer. In the natural turbulent wall jet without forcing, Zhou et al (1993b) observed a frequency factor of approximately 1.7 between the inner layer and outer layer which depended on the velocity ratio R unless the two models were coupled. In the case of weak excitation, Zhou et al (1996) found that, the skin friction was reduced by about 7% between $X/b = 100$ and 200 and the intensity of $\overline{u'^2}$ was significantly increased by forcing. The excitation also increased the intensity of $\overline{v'^2}$ in the outer region, but did not affect the spanwise fluctuations $\overline{w'^2}$.

Stability Considerations

A theoretical stability analysis was performed to gain insight into the stability of the strong heated turbulent wall jet and understand the mechanisms that might be exploited for its control, Likhachev (2000). Unlike the laminar wall jet, the theoretical analysis pointed out that the turbulent wall jet has no strong dominant modes but rather responds over a wider frequency spectrum. The propagation and amplification of the small-amplitude disturbance waves were modeled as linear instabilities of the mean velocity and temperature profiles. Because the flow is incompressible and experimental temperature difference is small, temperature can be treated as a passive scalar. The influence of incoherent turbulent fluctuations on the large-scale external perturbations was taken into account with an eddy viscosity model that was consistent with the mean flow. Since the Reynolds number based on the local maximum value of the eddy viscosity is not sufficiently large, non-parallel effects should be considered in the stability calculations. The multiple-scales expansion method was used in conjunction with similarity laws of the mean flow to predict the influence of the jet growth on the linear stability characteristics. Calculations of the perturbation behavior were made for a variety of imposed frequencies. It was shown that some significant experimental conclusions based on local measurements could be attributed to the divergence of the flow. In particular, the existence of different predominant frequencies in the outer and inner regions of the turbulent wall-jet flow can be attributed to non-parallel effects rather than to nonlinear effects or to the possible existence of another mode of instability. A comparison of the stability calculations with the experimental data and the Large-Eddy Simulations is ongoing.

Experimental Measurements

The experiments were performed in a thermally controlled, closed return, low speed, air wind tunnel shown in Fig. 5. The wind tunnel provided a thermally controlled, low speed main flow at a velocity U_∞ of 5.0 m/s and temperature T_∞ of 23.7 °C. The test section was 711 mm wide, 165 mm high and 2,362 mm long. A slot type wall jet apparatus was used which essentially duplicates the design of Zhou et al. (1993a) used in the study of a turbulent wall jet with forcing. The wall jet is introduced tangentially just upstream of the isothermal surface. Flow is delivered by a 0.5 hp centrifugal blower. The flow enters an air-water heat exchanger followed by a diffuser that decelerates the flow into a plenum chamber. The plenum chamber is fitted with an acoustic speaker that is used to introduce controlled disturbances (forcing) into the jet. Three screens of 30, 40 and 50 mesh size and a contraction having a variable area

ratio complete the apparatus. In the present experiments, the jet contraction ratio is 18:1 resulting in a jet slot width b of 5.0 mm and a jet exit velocity U_j of 21.0 m/s. The jet temperature T_j of 23.7 °C was held constant by an air-water heat exchanger and a recirculating chiller.

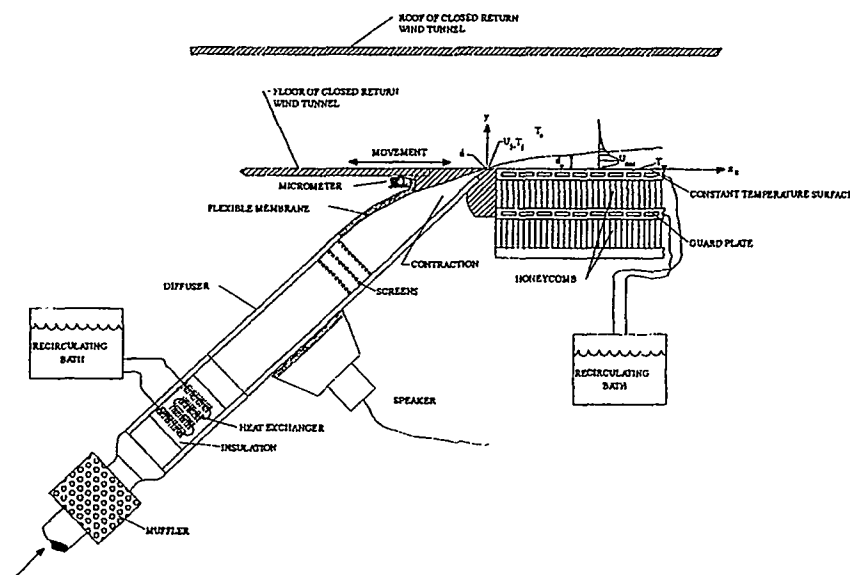


Figure. 5 Experimental apparatus

An isothermal heat transfer surface is located downstream of jet exit plane, and has an unheated starting length of $X/b = 7$. This surface consists of a 19-mm thick, 508 mm wide and 1219-mm long highly polished aluminum tooling plate, which is held at constant temperature by means of, heated water from a recirculating chiller that flows through milled slots inside the plate. A 50.8-mm thick sheet of honeycomb is placed beneath the plate and serves as an insulator and as a rigid support for the top plate. Another plate with heated flow is placed beneath the honeycomb to stabilize any backside thermal losses. The excited jet flow passes along with a 50.8-mm diameter aluminum Coanda cylinder and flows tangentially over this heat transfer surface. The side and top walls of the test section are fabricated of Plexiglas to allow visualization studies to be accomplished.

The measurements of streamwise velocity and temperature were conducted using two side-by-side (12 mm apart in spanwise direction) standard DISA 55-P11 single hot and cold wire probes, which were held by a well-designed probe holder. Both the hot and cold bridges were manufactured by AA Lab System (model AN-1003). The cold wire was calibrated against a NIST traceable lab standard thermistor probe, and the hot wire probe was calibrated in the exit of a thermally controlled vertical axisymmetric jet against a standard Pitot tube and an MKS Baratron pressure transducer. Due to temperature gradients in the flow field, the hot wire output voltage required temperature compensation. The hot wire output voltage was thus calibrated at different velocities for the range of temperatures, which were used in the experiment. A polynomial relationship between voltage and temperature for each velocity was produced and used to find the temperature compensated voltage by iteration. Using this method, the actual velocity can be found due to the small temperature difference between T_w and ambient. In order to observe the effects of external forcing on the velocity and temperature fields, pressure fluctuations were artificially introduced into the wall jet with a 304.8-mm loud speaker placed in the diffuser section. Four frequencies, 37.5Hz, 75.0Hz, 100Hz, and 105Hz, and two amplitudes, 5% and 10%, were chosen in present experiments.

Detailed experiments were performed to first determine the time averaged mean flow and heat transfer characteristics of an unforced, plane turbulent wall jet flowing over an isothermal surface that was

heated above the jet and ambient temperature. All experiments were performed in air. A jet velocity of 21.0 m/s and free-stream velocity of 5.0 m/s formed the base case for the measurements. Figure 6 shows the mean velocity profiles, comparing the unforced case to forcing at 100 Hz, 10 % amplitude. The near wall profiles shown in Fig. 7 accentuate the decrease in the near wall gradient and hence the wall shear stress when forcing is introduced. The near wall temperature profiles, Fig. 8, do not show appreciable changes, except at far downstream distances. Subsequently, the wall friction coefficient, C_f , decreases at all downstream distances, with forcing at all frequencies, Fig. 9, but the wall Stanton number exhibits only modest changes, Fig. 10. Although these results have not yet been studied in great detail, a significant clue as to the insensitivity of the wall heat transfer to forcing is provided by examination of the fluctuating temperature distribution, Fig. 11. It is seen that even at a 10% forcing amplitude, the near wall fluctuating temperatures are not strongly influenced. Because t' is a primary component of the turbulent heat flux, $v't'$, one plausible explanation is that the two-dimensional structures in the outer shear layer do not necessarily cascade downwards at sufficiently small scales to augment the near wall heat transfer. This is an area currently under intense study.

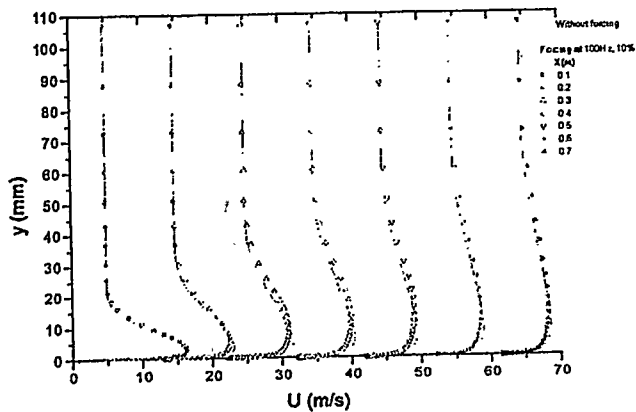


Figure 6. Mean velocity profiles with and without forcing

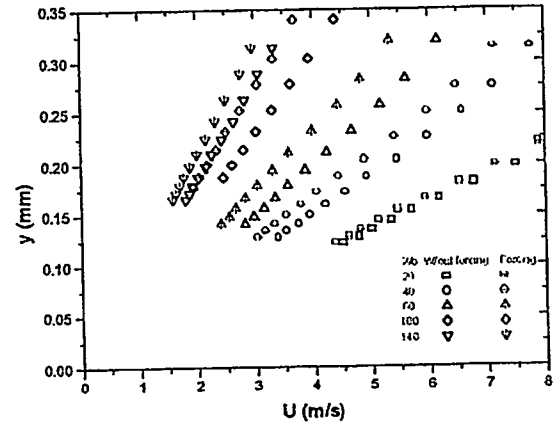


Figure 7. Mean velocity profiles near the wall

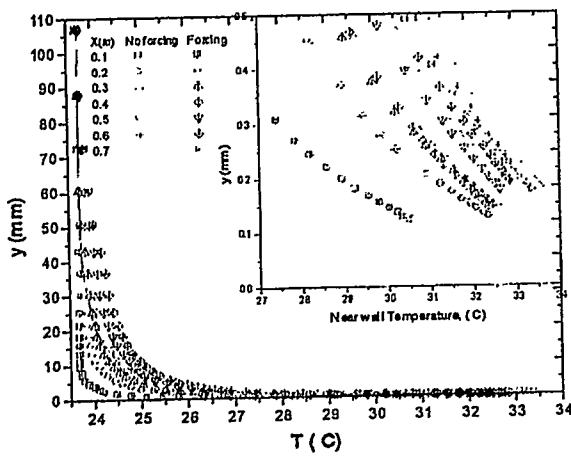


Figure 8. Mean temperature profiles with and without forcing

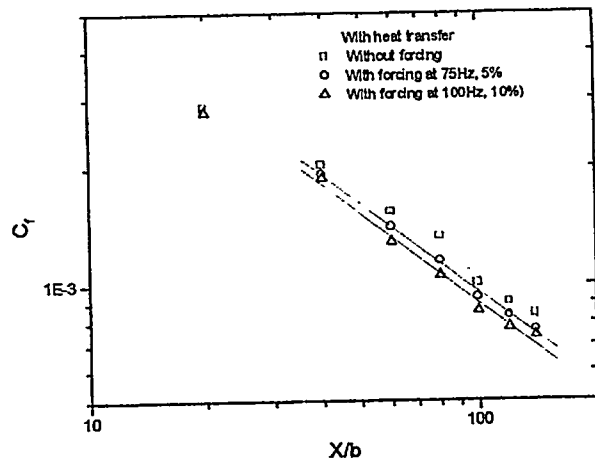


Figure 9. Wall friction coefficient with forcing

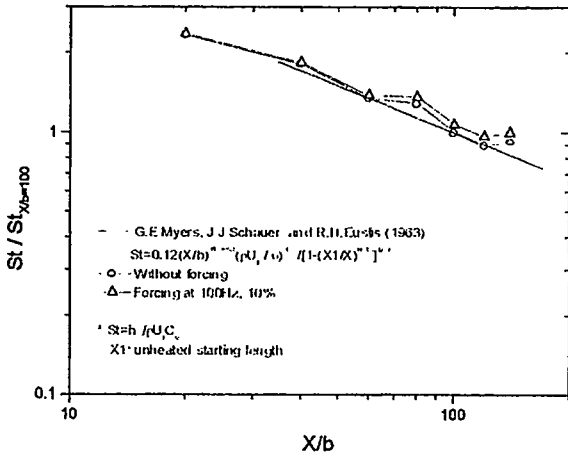


Figure 10. Normalized Stanton Number

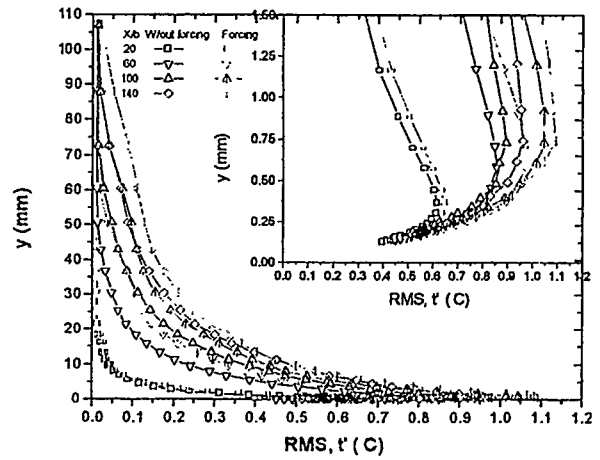


Figure 11. Fluctuating temperature

Computational Results

The DNS code described previously was used to investigate the effect of large coherent structures on the turbulent wall jet. A state-of-the-art two-equation turbulence model was implemented in the code. This necessitated the development of an accurate and robust solver for the $k-\epsilon$ equations. The code has been tested for the flat plate boundary layer and the turbulent wall jet mean flow. Figure 12 shows the turbulent mean velocity profile in outer coordinates. Excellent agreement with the theoretical and experimental data is achieved. In inner coordinates (Fig. 14), a slight discrepancy in the maximum velocity exists, but the overall agreement with the theoretical curves and the experiments is very good. In Figs. 13 and 15, the mean temperature profile is shown in outer as well as wall coordinates. Very good agreement is achieved between the measurements and the computations. For comparison, various logarithmic laws found in the literature are included in the figure.

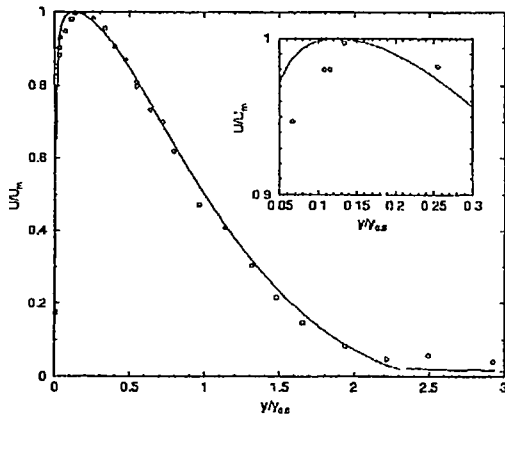


Figure 12. Mean velocity profile in outer coordinates

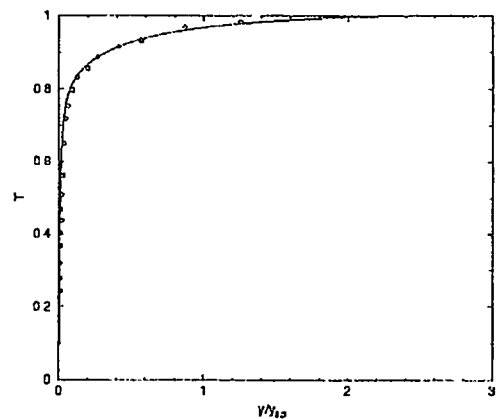


Figure 13. Mean temperature profile in outer coordinates

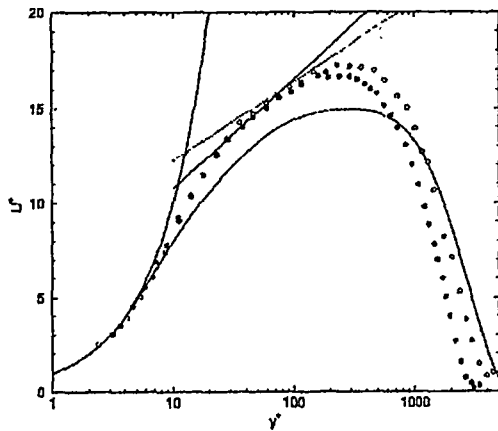


Figure 14. Mean velocity profile in wall coordinates

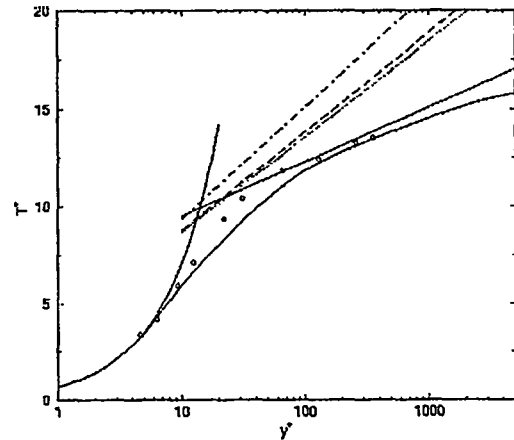


Figure 15. Mean temperature profile in wall coordinates

CONCLUSIONS

In order to understand the heat and momentum transfer associated with complex unsteady film-cooling problems, the plane, laminar, wall jet was investigated experimentally, theoretically, and numerically for the constant wall temperature boundary condition and with no free-stream. When forcing is introduced, two staggered rows of vortical disturbances develop. At high amplitudes, these structures increase the mixing within the wall jet, which in turn increases the spreading rate and reduces the skin friction. In addition, the large structures entrain cold fluid from the ambient, and hot fluid is convected away from the wall, which leads to an increase in the effective thermal diffusion. Locally, the highly unsteady flow field leads to the development of very high wall temperature gradient and in the mean to an inflection point in the temperature profile and an increase in the wall heat transfer. It is found that forcing both the principal and subharmonic modes is most efficient.

Experimental investigations of the turbulent wall jet show that forcing at all frequencies generally decreases the wall friction because the growth rate of the jet increases. Locally, the decrease in wall friction does not seem to have a comparable effect on the wall heat transfer. The wall heat transfer is not strongly influenced by the forcing, possibly because the outer shear layer vortices that dominate the flow when forcing is introduced do not necessarily produce the small scale turbulence in the inner region that is so important in scalar transport. Preliminary computational investigations of the turbulent wall jet show that the turbulence model is capable of predicting the turbulent mean flow accurately. In the next step, disturbances will be introduced to investigate the effect of large, coherent structures on the mean flow characteristics of the turbulent wall jet. Towards this end, preliminary investigations have been initiated. Qualitatively, the effect of the structures on the turbulent flow is very similar to the laminar flow.

ACKNOWLEDGMENTS

This work was supported by the United States Department of Energy under grant number DE-FG03-93ER14396.

REFERENCES

1. Jeong, J. and Hussain, F., 1995. "On the Identification of a Vortex," *Journal of Fluid Mechanics*, 285: 69-94.
2. Katz, Y., Horev, E. and Wygnanski, I., 1992, "The Forced Turbulent Wall Jet", *Journal of Fluid Mechanics*, 242: 577-609.
3. Likhachev, O., 1998, "Resonant-triad Interaction in a Wall Jet," *Physics of Fluids*, Vol. 10, 3: 627-636.
4. Likhachev, O. A., Quintana, D. L. and Wygnanski, I., 1999, "On the Stability of a laminar Wall Jet with Heat Transfer," *Journal of Flow Turbulence and Combustion*, 62: 137-162.
5. Likhachev, O., 2000, "On Harmonic Perturbations in a Turbulent Wall Jet," manuscript in preparation.
6. Mitachi, K. and Ishiguro, R., 1974, "Heat Transfer of Wall Jets (1st report: Theoretical Discussions of the Temperature field)," *Heat Transfer, Japanese Research*, 27-40.
7. Myers, G.E., Schauer, J.J. and Eustis, R.H., 1963, "Plane Turbulent Wall Jet Flow Development and Friction Factor," *Journal of Basic Engineering*, Trans. of the ASME, 47-54.
8. Myers, G.E., Schauer, J.J., and Eustis, R.H., 1963, "Heat Transfer to Plane Turbulent Wall Jets," *Journal of Heat Transfer*, Trans. of the ASME, 209-214.
9. Nizou, P.Y., 1981, "Heat and Momentum Transfer in a Plane Turbulent Wall Jet," *Journal of Heat Transfer*, Transactions of the ASME, 103: 138-140.
10. Seban, R.A., 1960 "Heat Transfer and Effectiveness for a Turbulent Boundary Layer With Tangential Fluid Injection," *Journal of Heat Transfer*, 303-312.
11. Seban, R.A. and Back, L.H., 1961, "Velocity and Temperature Profiles in a Wall Jet," *Int. J. Heat Mass Transfer*, 1961, 3: 255-265.
12. Seidel, J. and Fasel, H. F., 2000, "Numerical Investigations of Heat Transfer Mechanisms in the Forced Laminar Wall Jet," in press, *J. Fluid Mechanics*.
13. Quintana, D.L., Amitay, M., Ortega, A. and Wygnanski, I., 1997, "Heat Transfer in the Forced Laminar Wall Jet," *Journal of Heat Transfer*, Trans. of the ASME, 119: 451-459.
14. Zhou, M. D., Heine, C. and Wygnanski, I., 1993, "The Forced Wall Jet in an External Stream," *AIAA* 93-3250.
15. Zhou, M.D. and Wygnanski, I., 1993, "Parameters Governing the Turbulent Wall Jet and External Stream," *AIAA Journal*, 51(5): 843-853.
16. Zhou, M.D., Heine, C. and Wygnanski, I., 1996, "The Effects of Excitation on the Coherent and Random Motion in a Plane Wall Jet," *Journal of Fluid Mechanics*, 310:1-37.

OPTIMIZATION OF HEAT TRANSFER EFFECTIVENESS IN HETEROGENEOUS MEDIA

V.S. Travkin, I. Catton and K. Hu
 University of California, Los Angeles
 Mechanical and Aerospace Engineering Department
 Los Angeles, CA 90095-1597

ABSTRACT

Developments of Volume Averaging Theory (VAT) to describe transport phenomena in heterogeneous media are applied to optimization of heat dissipation from a heterogeneous media. The media is an unspecified porous (heterogeneous) layer and the optimization process is accomplished with rigor using the idea of scaled energy transport. The enhancement of heat transport is stated mathematically in a way that the lower scale conventional pin heat transport enhancement and the performance of the total device are incorporated for optimization. The problem is addressed in three steps: 1) solution of a two-temperature problem with inclusion of experimental data correlations, 2) statistical design of experiments (simulating the problem) for problems with many optimization parameters, and 3) optimization of 2D heterogeneous volumetric heat removal by conduction and convective exchange. The analysis distinguishes certain classes of distributed parameter optimization statements whose solutions determine global "in-class" upper limits of heat enhancement (for a given set of physical assumptions).

1. INTRODUCTION

Development of a VAT mathematical basis and models for optimization of a heterogeneous, hierarchical scaled media began with work by Travkin, Gratton and Catton [1] and is followed by a series of papers [2-4] documenting the development of a method that is applicable to a wide variety of transport phenomena ranging from fluid mechanics to crystal photonic band-gap problems [5], clearly demonstrating the interdisciplinary nature the multi-scale VAT description of transport phenomena. The theoretical development of transport phenomena in heterogeneous media with multiple scales has now been brought to the level where a specific application can be chosen for demonstration. The application chosen is enhancement of heat transfer dissipation from a heterogeneous media while minimizing the frictional resistance (a problem of importance to all designers of heat exchangers). This problem has been under investigation for more than 3 decades and in spite of its longevity and importance as a problem, it has not been satisfactorily treated.

A majority of past investigations focused on solutions to a specific optimization task with a very limited number of spatial parameters to be varied, usually a fixed geometric configuration, that they tuned in their search for a maximum level of heat exchange (see, for example, Bejan and co-authors [6,7] and references therein). This approach is a "single-scale" approach yielding an optimum for a certain morphology and flow intensity without giving an explanation for why it was achieved. Without an explanation, there is no guidance on how to change the design to improve its performance. For each new morphology, the experiment, whether real or numerical, needs to be performed again. In the heat exchanger industry there are countless research studies devoted to this problem.

In this work we outline how earlier studies [1-5] can be applied to a practical application. The present treatment of the heat exchange optimization process can be applied to any specific hierarchical heterostructure with the aim to optimize its performance. What has been done is a demonstration of the only heterogeneous media modeling tool that combines both mathematical and morphological descriptions in one problem statement.

2. VAT EQUATIONS IN THE FORM OF CONTROL EQUATIONS

The averaged laminar momentum equation

$$\nu \frac{\partial}{\partial z} \left(\langle m(z) \rangle \frac{\partial \tilde{U}(z)}{\partial z} \right) + U_{MCOnv} + U_{MFriction} - U_{MDrag} = \frac{1}{\rho_f} \frac{\partial (\langle m(z) \rangle \tilde{p})}{\partial x}, \quad (1)$$

is "controlled" by the three morphological terms that are defined as the "morpho-convective" fluctuation field distribution based term

$$U_{MCOnv}(\hat{u}, \hat{w}, \partial S_w, \Delta \Omega_f, \Delta \Omega_s) = \frac{\partial}{\partial z} (\langle -\hat{u} \hat{w} \rangle_f), \quad (2)$$

the interface surface skin friction term

$$U_{MFriction}(U, \partial S_w, \nu) = \frac{\nu}{\Delta\Omega} \int_{\partial S_w} \frac{\partial U}{\partial x_i} \cdot \vec{ds}, \quad (3)$$

and the solid phase drag resistance term

$$U_{MDrag}(p_j, \partial S_w) = \frac{1}{\rho_f \Delta\Omega} \int_{\partial S_w} p \vec{ds}, \quad (4)$$

where the second left hand side term $\partial \left(\langle -\hat{u} \hat{w} \rangle_f \right) / \partial z$ presents cross-fluctuations effect. The presence of the vertical velocities - W and \tilde{W} , or $\hat{w} = W - \tilde{W}$, seen in the first term, do not exist at the macrolevel because z direction momentum transport is only present locally close to obstacles. In traditional (homogeneous) one-scale shape optimization approaches these three terms are not presented (see, for example, Ledezma et al. [7]) and, as a result, optimization methods are very restricted in their value and clearly the macroscopic behavior cannot be related to the bottom scale enhancement.

The laminar fluid energy equation is

$$c_{pf} \rho_f \langle m \rangle \tilde{U} \frac{\partial \tilde{T}_f}{\partial x} = k \frac{\partial}{\partial x} \left[\frac{\partial \langle m \rangle \tilde{T}_f}{\partial x} \right] + k \frac{\partial}{\partial z} \left[\frac{\partial \langle m \rangle \tilde{T}_f}{\partial z} \right] + T_{fMConvX} + T_{fMConvZ} + T_{fMSurfX} + T_{fMSurfZ} + T_{fMExchange}. \quad (5)$$

with the five additional control terms being

$$T_{fMConvX}(\hat{T}_f, \hat{w}, \Delta\Omega_f, \Delta\Omega_s) = c_{pf} \rho_f \frac{\partial}{\partial x} \left(\langle m \rangle \left\{ -\hat{T}_f \hat{u} \right\}_f \right), \quad (6)$$

$$T_{fMConvZ}(\hat{T}_f, \hat{w}, \Delta\Omega_f, \Delta\Omega_s) = c_{pf} \rho_f \frac{\partial}{\partial z} \left(\langle m \rangle \left\{ -\hat{T}_f \hat{w} \right\}_f \right), \quad (7)$$

$$T_{fMSurfX}(k, T_f, \partial S_w) = k \frac{\partial}{\partial x} \left[\frac{1}{\Delta\Omega} \int_{\partial S_w} T_f \vec{ds} \right], \quad (8)$$

$$T_{fMSurfZ}(k, T_f, \partial S_w) = k \frac{\partial}{\partial z} \left[\frac{1}{\Delta\Omega} \int_{\partial S_w} T_f \vec{ds} \right], \quad (9)$$

$$T_{fMExchange}(k, T_f, \partial S_w) = \frac{k}{\Delta\Omega} \int_{\partial S_w} \frac{\partial T_f}{\partial x_i} \cdot \vec{ds}, \quad (10)$$

Finally, the solid phase energy equation has the similar additional terms. In the turbulent regime, the momentum, fluid energy and solid energy equations are similar to what are shown but with an increased number of control terms and more complexity. They are not reproduced here and can be found in [2,4,5]. Some discussion about how they will be dealt with is found in the final section of this paper.

The control equations are made general by non-dimensionalization with the following scaling, see Fig. 1,

$$S_w = S_w^* S_{wm}, \quad z = z_m z^*, \quad z_m = \frac{4m_0}{S_{wm}}, \quad \tilde{U} = u_m u^*, \quad T_m = \frac{z_m Q_0}{K T_m}, \quad \nu = z_m u_m \nu^*, \quad \langle m(z) \rangle = m_0 \langle m^* \rangle, \\ c_d = C_d^* c_{dm}, \quad c_{dm} = \frac{2u_m^2}{u_0^2}, \quad \frac{1}{\rho_f} \frac{d\langle p \rangle_f}{dx} = -\frac{u_m^2}{z_m}, \quad k_{fm} = z_m u_m c_{pf} \rho_f, \quad k_f = k_f^* z_m u_m c_{pf} \rho_f, \quad k_s = k_s^* z_m u_m c_p \rho_s.$$

The parameters resulting for laminar flow through a morphology that is constant normal to the flow direction are given in the following table with there possible ranges. These parameters are at the discretion of the designer of a heat transfer device and can be used for optimization.

Name	variable	min	max	Physical meaning of the parameter
L_{3N}	$= Re_{mf} c_{dm} C_d^* S_w^*$	10^{-5}	5×10^7	influence of media resistance to flow
L_{MAN}	$= Re_{mf} (1/m_0)$	10^{-3}	10^5	media Reynolds number
L_{P5}	$= \frac{1}{Pe_m} = \frac{z_m u_m}{a_f}$	2.1	2×10^7	Peclet number, $Pe = \left(\frac{4m_0}{S_{mw}} \left(-\frac{z_m}{\rho_f} \frac{d\langle p \rangle}{dx} \right)^{1/2} \right) / a_f$
L_{P6}	$= \alpha_L^* S_w^* = \frac{\alpha_L S_w}{\alpha_{Lm} S_{Lm}}$	1.0	10^8	heat exchange between phases, $\alpha_L^* S_w^* = \frac{\alpha_L S_w}{u_m c_p \rho_f S_{wm}}$
L_{P7N}	$= \frac{Pe_m}{A_k (L_{MA} - 1)} \alpha_L^* S_w^*$	0	10^{20}	parameter from solid phase energy equation
L_{B8}	$= \frac{A_k}{Pe_m} = A_k L_{P5}$	10^{-3}	10^{12}	parameter from II kind BC, see [8]

There are six nondimensional control parameters and functions, denoted Medium Specific Control Functions (MSCF), that control the heat and momentum transport in the selected porous medium and that can be modified to optimize the performance. The two terms with the broadest range also have the greatest influence on the outcome. If the morphology functions denoting porosity, $\langle m(z) \rangle$, and specific surface area, $S_w(z)$, are coordinate specific, then the equations and parameters sets are different yielding eight control parameters instead of six. A similar exercise for turbulent flow with $\langle m \rangle = const$, $S_w = const$ will yield eight optimization parameters.

3. PRELIMINARY OPTIMIZATION METHODS

Some simulation results using VAT based transport and closure models for flow in a channel with rib roughened walls, spherical beads, round tube banks and square tube banks yielded optimal configurations. The morphology models used in the numerical simulations are shown in Fig.1 (see [9]).

The parameters chosen for simulation of flow across spherical beads in a channel were pitch, $P = 20mm$, channel height, $2h = 200mm$, and bead diameter, $0.001mm < d_p < 20mm$. When the diameter of the beads is large, the disturbance of the porosity across the channel is large and the flow resistance plays an important role. As a result the disturbance of the velocity profile is large. When the porosity approaches unity the disturbance of velocity profile disappears and the velocity distribution approaches the theoretical distribution. From a physical viewpoint, this is obvious. When there are no obstacles in the channel, the channel the results are consistent with the theoretical results in contrast with some other models.

The pitch chosen of the rods are the same as those for the beads. The height of the rods is the same as channel height. The porosity is easily varied from 0 to 1.0. by ranging the tube dimension, d_p . The friction factor for flow across square tube banks and circular tube banks were developed from the micromodeling results of Souto & Moyno [10] and Watanabe [11] respectively.

By application of SVAT closure models to some general morphology models (orifices and plane slits), in limiting cases, it was demonstrated earlier [1-3,8,9] that both the transport model and the closure scheme are reasonable. At the same time, studying the limiting cases of porosity in the channel highlighted mistakes in other studies. The numerical results demonstrate how the simplest morphological properties of a porous layer such as porosity function and specific surface along with closure models naturally affects the transport features and that it can be helpful in the development of optimized morphologies.

Fig. 2 shows the dependence of the effectiveness number, E_{ff} , on the porosity for different morphologies at different Reynolds numbers. E_{ff} is a combination of the Nusselt number, the friction factor and the pore Reynolds number,

$$E_{ff} = \frac{Nu}{Re_{por} f^{1/3}}, \text{ with } Nu = \frac{\tilde{\alpha} d_{por}}{k_f}, Re_{por} = \frac{4 \langle m \rangle \tilde{u}}{\nu S_w} \text{ and } f = \frac{d_h}{2 \rho_f \tilde{u}^2} \left(\frac{\Delta P}{L} \right) \quad (11)$$

Fig 2 shows how E_{ff} increases as the porosity of the channel decreases. When the porosity decreases, the beads inside the channel play a more important role in increasing the heat transfer while increasing the flow resistance. (for channel filled with regularly arranged spherical beads, the porosity of the channel has a lower limit of 0.4). Fig. 3 and 4 clearly demonstrates an optimum value of E_{ff} . When the porosity is higher than some critical value, the porous media play a more important role in increasing the heat transfer than in increasing the drag resistance. But when the porosity is too low, the drag resistance will be high and E_{ff} will approach 0 when the porosity approaches 0.

When the problem becomes multi-dimensional, 6D or 8D, according to [12-15], it is convenient to use the statistical design of experiment (DOE) methodology. An optimal response surface was found in two steps. First, numerical simulation was carried out based on statistical selection of the parameter values. Second a statistical analysis of the results was used to develop a response surface. This procedure was implemented using a commercial computer code based on DOE.

When the optimization variable is chosen, in our case E_{ff} , the variables are systematically defined, see the table of parameters developed above. Next, the numerical experiment design type is selected, e.g. a classical two level,

mixed level, or nested level. The design type used in this work is the classical two level design. The classical two level designs are based on standard orthogonal arrays that contain two levels for each experimental variable. It enables estimation of the effects of some or all terms in a second order model of the general form

$$E_{ff} = a_0 + a_1X_1 + a_2X_2 + \dots + a_nX_n + a_{11}X_1^2 + a_{12}X_1X_2 + \dots + a_{n,n-1}X_nX_{n-1} + a_{nn}X_n^2$$

The independent variables X_1, X_2, \dots, X_n are the design variables $L_{3N} \dots L_{138}$. Based on the design type and design variables, experiment design options will be created. Each option is a set of input parameters for numerical simulation. Description of what was done to obtain the "experimental results" from the VAT based laminar or turbulent transport equations for flow in a specific porous media is described elsewhere (see [8,9]).

After numerical simulation, the numerical results are rigorously analyzed using statistical analysis tools and graphics tools. These tools include nonlinear response/error analysis, experimental error analysis, regression analysis, residuals analysis, two dimensional graphing, three dimensional response surface graphing, and multi response optimization. One of the response surfaces of our study is shown in Fig. 5. The three dimensional figure shows E_{ff} as a function of two variables L_{P2} and L_{M4} (these were chosen for simplicity from the eight independent variables analyzed) when the other variables are fixed. Although limited by the range of the variables, the optimum point is shown on the figure, and the trend of the response surface clearly shown in Fig. 5.

4. TWO- AND THREE-SCALE OPTIMIZATION STUDY

Closure of the turbulent regime VAT equations for a porous flat channel also requires closure of additional terms in the governing equations. This is done (as for laminar regime) using Direct Numerical Modeling (DNM). The four terms arising in the momentum equation are

$$\frac{\partial}{\partial z} \left(\left\langle \widehat{K}_m \frac{\partial \widehat{u}}{\partial z} \right\rangle_f \right), \frac{\partial}{\partial z} \left(\left\langle -\widehat{u} \widehat{w} \right\rangle_f \right), \frac{1}{\Delta\Omega} \int_{\partial S_w} (K_m + \nu) \frac{\partial \bar{U}}{\partial x_i} \cdot \vec{ds}, \frac{1}{\rho_f \Delta\Omega} \int_{\partial S_w} \bar{p} \cdot \vec{ds}, \quad (12)$$

the seven terms in the fluid temperature equation

$$\frac{\partial}{\partial x} \left(\left\langle \widehat{K}_r \frac{\partial \widehat{T}_f}{\partial x} \right\rangle_f \right), \frac{\partial}{\partial z} \left(\left\langle \widehat{K}_r \frac{\partial \widehat{T}_f}{\partial z} \right\rangle_f \right), c_{pf} \rho_f \frac{\partial}{\partial x} \left(\langle m \rangle \left\{ -\widehat{T}_f \widehat{u} \right\}_f \right), c_{pf} \rho_f \frac{\partial}{\partial z} \left(\langle m \rangle \left\{ -\widehat{T}_f \widehat{w} \right\}_f \right), \quad (13)$$

$$\frac{\partial}{\partial x} \left[\frac{(\tilde{K}_r + k)}{\Delta\Omega} \int_{\partial S_w} \bar{T}_f \cdot \vec{ds} \right], \frac{\partial}{\partial z} \left[\frac{(\tilde{K}_r + k)}{\Delta\Omega} \int_{\partial S_w} \bar{T}_f \cdot \vec{ds} \right], \frac{1}{\Delta\Omega} \int_{\partial S_w} (K_r + k) \frac{\partial \bar{T}_f}{\partial x_i} \cdot \vec{ds} \quad (14)$$

and five terms in the solid phase temperature equation

$$\frac{\partial}{\partial x} \left[\left\langle \widehat{K}_s \frac{\partial \widehat{T}_s}{\partial x} \right\rangle_s \right], \frac{\partial}{\partial z} \left[\left\langle \widehat{K}_s \frac{\partial \widehat{T}_s}{\partial z} \right\rangle_s \right], \frac{\partial}{\partial x} \left[\frac{\{K_s\}_s}{\Delta\Omega} \int_{\partial S_{w12}} T_s \cdot \vec{ds}_1 \right], \frac{\partial}{\partial z} \left[\frac{\{K_s\}_s}{\Delta\Omega} \int_{\partial S_{w12}} T_s \cdot \vec{ds}_1 \right], \frac{1}{\Delta\Omega} \int_{\partial S_{w12}} K_{s,r} \frac{\partial T_s}{\partial x_i} \cdot \vec{ds}_1 \quad (15)$$

The mathematical implementation needed to obtain closure of the momentum resistance terms, for example, for optimization of the morphology of straight rib fins, see Fig. 6a,b; is dictated by the geometry of the fins. For example, if $\vec{ds} = \vec{n} ds$, $\vec{n} = (-i, 0, 0)|_{\partial S_{wL}}$ and $\vec{n} = (i, 0, 0)|_{\partial S_{wR}}$, then the surface integral over the ∂S_w in each of the intermediate REV's not including portions of the free volume above the fins and those at the bottom of the solid phase of the channel will be, for the x-coordinate frictional resistance component,

$$\begin{aligned} \frac{1}{\Delta\Omega} \int_{\partial S_w} (K_m + \nu) n_i \cdot \frac{\partial U_j}{\partial x_i} ds &= \left(\frac{1}{\Delta\Omega} \int_{\partial S_w} (K_m + \nu) \left(n_x \frac{\partial U}{\partial x} + n_y \frac{\partial U}{\partial y} + n_z \frac{\partial U}{\partial z} \right) ds \right) i = \\ &= \left(\frac{-1}{\Delta\Omega} \int_{z_{kL}}^{z^{(k+1)L}} \left[(K_m + \nu) \frac{\partial U}{\partial x} \right] \Big|_{\partial S_{wL}} dz + \frac{1}{\Delta\Omega} \int_{z_{kR}}^{z^{(k+1)R}} \left[(K_m + \nu) \frac{\partial U}{\partial x} \right] \Big|_{\partial S_{wR}} dz \right) i. \end{aligned} \quad (16)$$

The calculation of the form drag portion of resistance loss in momentum VAT equation is done in the same

mode

$$\frac{1}{\rho_f \Delta \Omega} \int_{\partial S_w} \bar{p} \vec{ds} = \frac{1}{\rho_f \Delta \Omega} \int_{\partial S_w} \bar{p} (\vec{n} ds) = \left(\frac{-1}{\rho_f \Delta \Omega} \int_{z_{kL}}^{z^{(k+1)L}} \bar{p}|_{\partial S_{wL}} dz \right) \mathbf{i} + \left(\frac{1}{\rho_f \Delta \Omega} \int_{z_{kR}}^{z^{(k+1)R}} \bar{p}|_{\partial S_{wR}} dz \right) \mathbf{i}. \quad (17)$$

This is the classical form drag portion of the total kinetic energy loss (shown here only for the x-component). Closure of other terms in the VAT equations are based on the specific two- or three scale morphologies chosen.

Our analysis of many existing morphological solutions has led us to conclude that the scaled hierarchical VAT description gives us the ability to find an optimum morphology that cannot be improved when the selection of fluids and solid phase materials has been made, and the pressure drop through the media is specified. Given these initial conditions (restrictions), it is possible to find a morphology that cannot be improved based on two scale heat transport meaning that there is no other solid phase configuration that can be more efficient than the one that has been found.

5. SUMMARY

In this brief paper we have illustrated a method hierarchical optimization of two- and three scale heat transport in a heterogeneous media. It is shown how traditional governing equations developed using rigorous VAT methods can be used to optimize surface transport processes in support of heat transport technology.

The difficulty in treating a multiparameter (more than 3) problem, even linear, are well known to be very difficult to overcome using a parameter sorting process. The combination of VAT based equations and the theory of statistical design to was used to effectively begin treating 6D or 8D optimization volumes.

We have shown how a two scale heterogeneous heat transfer optimization problem can be solved using exact procedures for closure of additional differential and integral VAT terms. This method is shown to be as simple as calculating the appropriate integrals over the morphologies with coordinate surfaces of interfaces pertinent to a morphology of interest. For more complex or even unknown morphologies, as initial spacial morphologies the mathematical methods were outlined in detail. These three tasks were carried out, albeit for some elementary morphologies, for the first time.

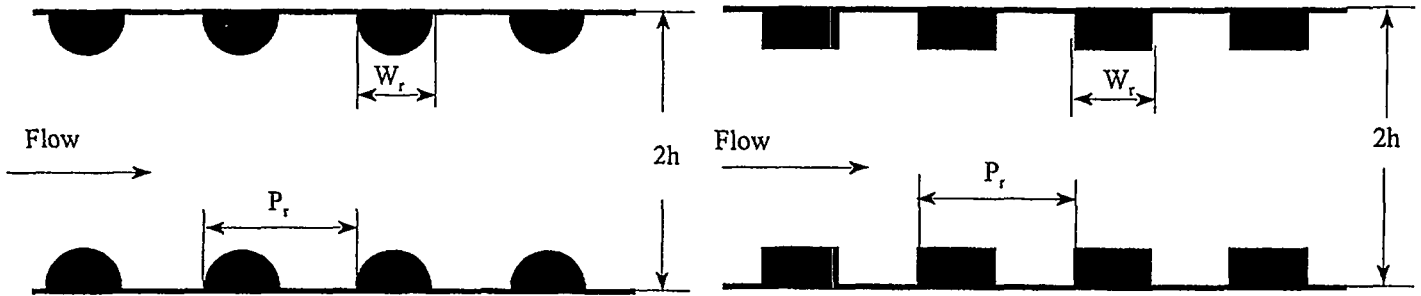
6. ACKNOWLEDGMENT

This work was sponsored by the U.S. Department of Energy, Office of Basic Energy Sciences under the Grant DE-FG03-89ER14033 A002.

7. REFERENCES

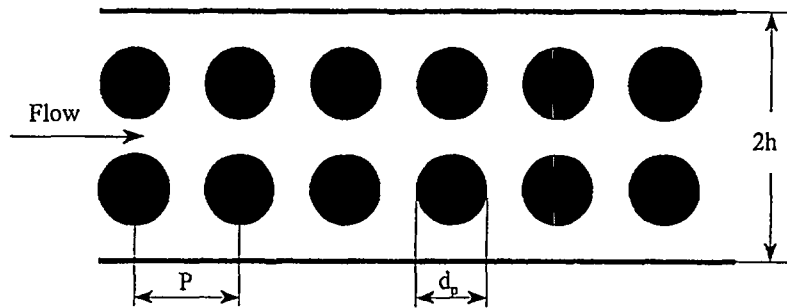
1. Travkin, V.S., Gratton, L., and Catton, I. (1994), "A Morphological-Approach for Two-Phase Porous Medium-Transport and Optimum Design Applications in Energy Engineering," *Proceedings of the Twelfth Symposium on Energy Engineering Sciences*, Argonne National Laboratory, Conf. -9404137, pp. 48-55.
2. Gratton, L., Travkin, V.S., and Catton, I. (1996), "The Influence of Morphology upon Two- Temperature Statements for Convective Transport in Porous Media," *Journal of Enhanced Heat Transfer*, Vol. 3, No. 2, pp.129-145.
3. Catton, I. and Travkin, V.S. (1997), "Homogeneous and Non-Local Heterogeneous Transport Phenomena with VAT Application Analysis", *Proceedings of the 15th Symposium on Energy Engineering Sciences*, Argonne National Laboratory, Conf. - 9705121, pp. 48-55.
4. Travkin, V.S. and Catton, I., (1998a), "Porous Media Transport Descriptions - Non-Local, Linear and Nonlinear Against Effective Thermal/Fluid Properties", in *Advances in Colloid and Interface Science*, Vol. 76-77, pp. 389-443.
5. V.S.Travkin and I. Catton, (2000), "Transport Phenomena in Heterogeneous Media Based on Volume Averaging Theory", in print *Advances in Heat Transfer*, Vol. 34.
6. Bejan, A. and Morega, A.M. (1993), "Optimal Arrays of Pin Fins and Plate Fins in Laminar Forced Convection," *Journal of Heat Transfer*, Vol. 115, pp. 75-81.
7. Ledezma, G., Morega, A.M., and Bejan, A. (1996), "Optimal Spacing Between Pin Fins with Impinging Flow," *Journal of Heat Transfer*, Vol. 118, pp. 570-577.
8. Travkin, V.S. and Catton, I. "A Two-Temperature Model for Turbulent Flow and Heat Transfer in a Porous Layer," *J. Fluids Eng.*, 117, 181 (1995).
9. V. S. Travkin, I. Catton, and K. Hu (1998), "Channel Flow In Porous Media In The Limit As Porosity Approaches Unity", in *Proc. ASME HTD-Vol. 361-1*, Vol. 1, pp. 277-284.
10. Souto, H.P.A. and Moyne, C., (1997), "Dispersion in Two-Dimensional Periodic Media. Part II. Dispersion Tensor", *Phys. Fluids*, Vol. 9, No. 8, pp. 2253-2263.

- 11 Watanabe, H., 1989, Drag coefficient and voidage function on fluid flow through granular packed beds, *International Journal of Engineering Fluid Mechanics*, Vol. 2, No. 1, pp. 93-108.
12. Atwood, C. L. (1969), "Optimal and Efficient Designs of Experiments", *Annals of Mathematical Statistics*, Vol. 40, No. 5, pp. 1570.
13. Box, G. E. P and Draper, N. R. (1987), *Empirical Model Building and Response Surfaces*, John Wiley & Sons, New York.
14. Diamond, W. J. (1981), *Practical Experiment Designs for Engineers and Scientist*, Wadsworth, Inc.
15. Montgomery, D. C., (1991), *Design and Analysis of Experiments*, 3rd Edition, John Wiley & Sons, New York.

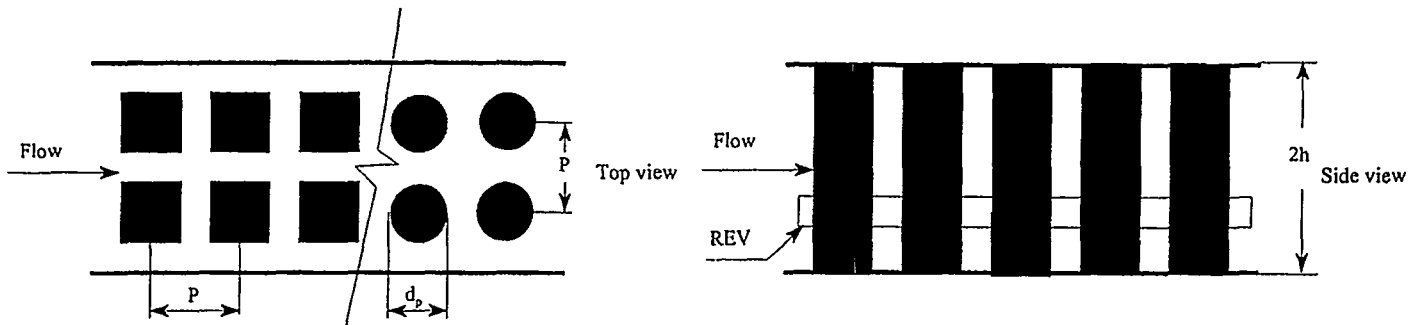


a. Two dimensional semi-cylindrical rib type roughness model

b. Two dimensional rectangular rib type roughness model



c. Channel flow across the lattice of spherical beads



d. Channel flow across rectangular and circular tube banks

Fig. 1 Some channel flow morphologies

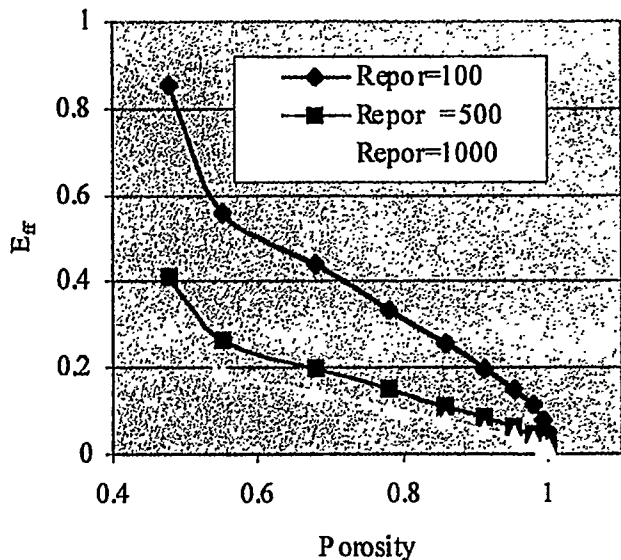


Fig. 2. Channel effective number versus porosity for flow across spherical beads.

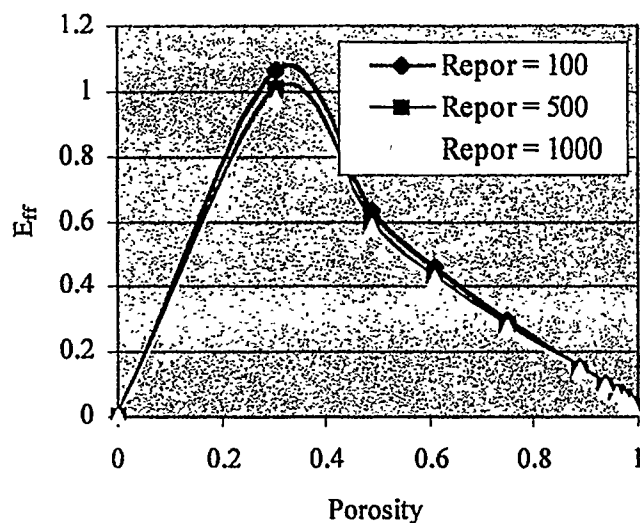


Fig. 3. Channel effective number versus porosity for flow across square tube banks.

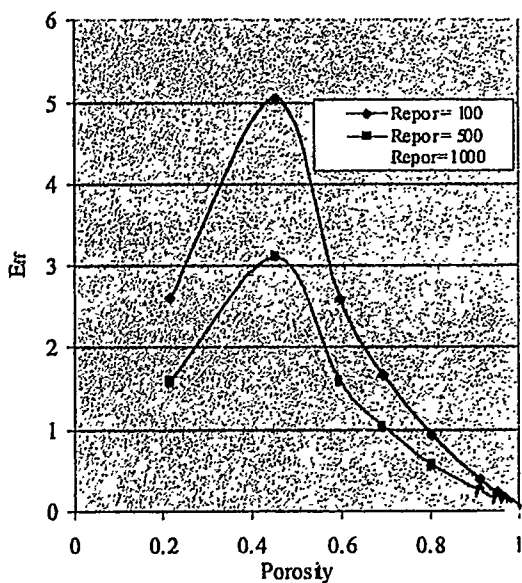


Fig. 4. Channel effective number versus porosity for flow across circular tube banks.

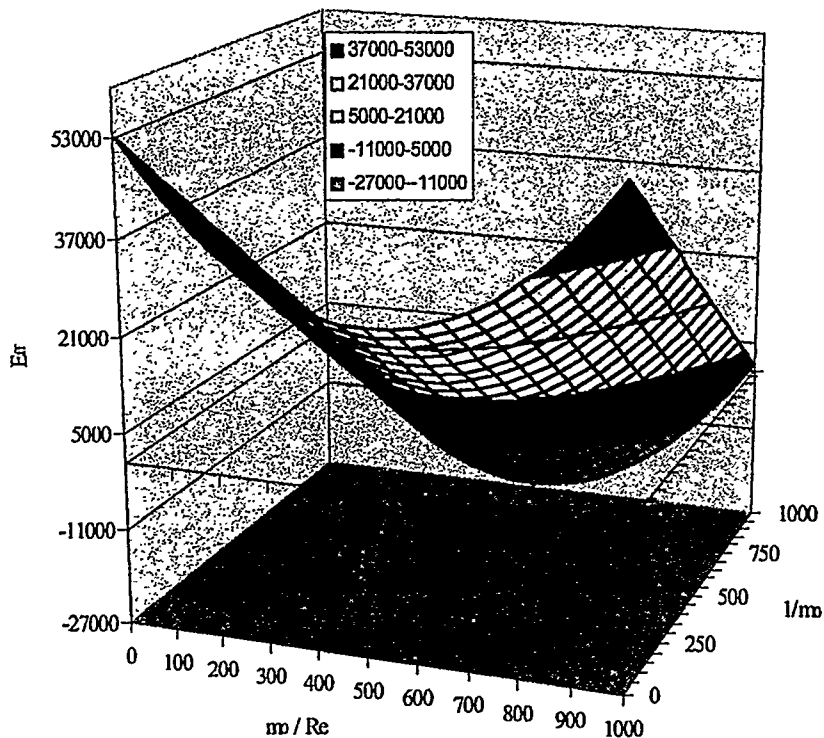


Fig. 5 Channel flow across circular tube banks optimization response surface

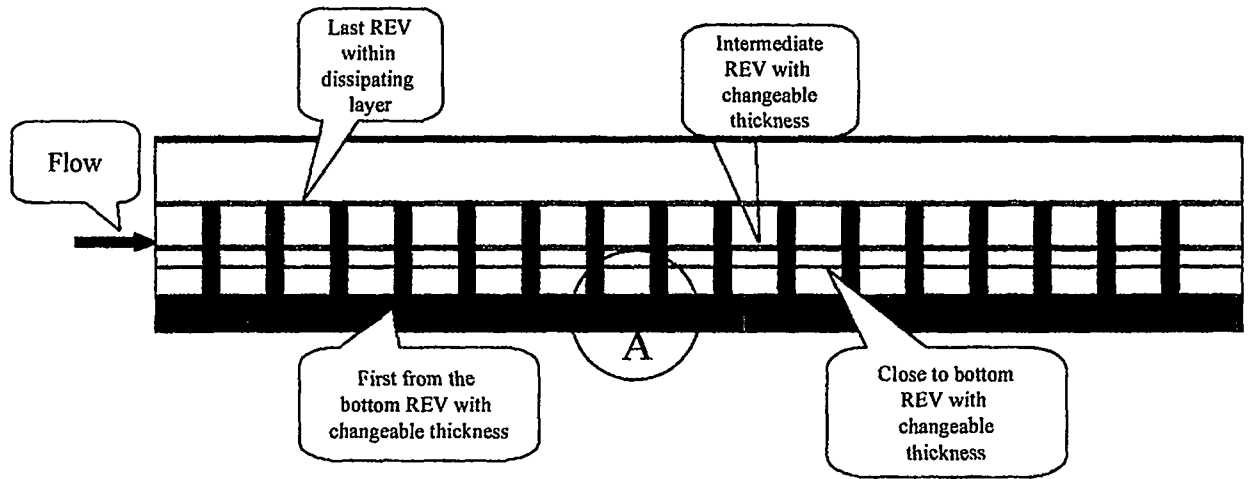


Fig. 6 a Flat Channel with Regular Heat Dissipation Layer
 - in each phase averaging done separately

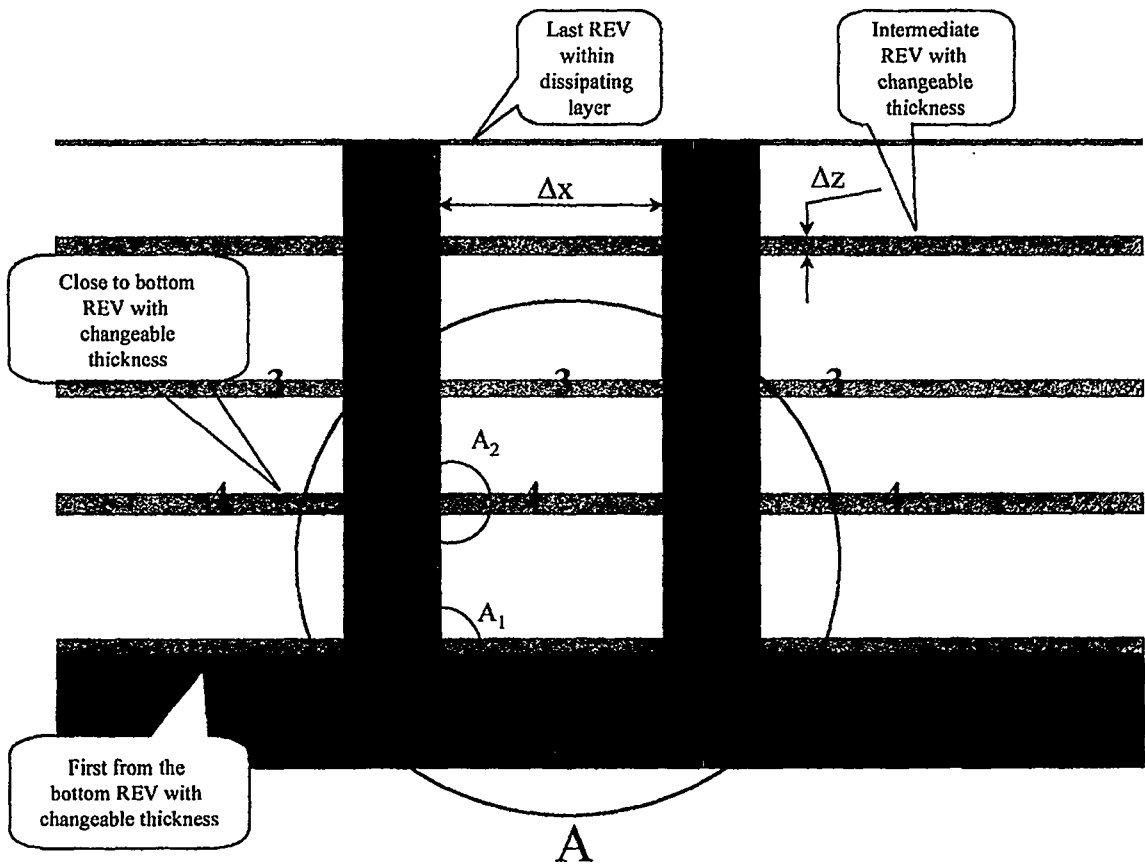


Fig. 6 b Solid phase temperature 1 and 2 and fluid phase 3 and 4 integrates in volumes separately for each REV and then represents point temperatures in the next scale of the problem

USE OF HOT-FILM ANEMOMETRY TECHNIQUE IN HORIZONTAL BUBBLY TWO-PHASE FLOW

Alaa Iskandrani and Gunol Kojasoy

University of Wisconsin-Milwaukee
Department of Mechanical Engineering
Milwaukee, Wisconsin 53201, U. S. A.

ABSTRACT

Utility of the hot-film anemometry technique in a horizontal bubbly flow-pattern is examined. It is shown that a single probe can be used for identifying the gas and liquid phases. Analyzing the nature of the voltage signal, a signal processing scheme is developed for measurements of time-averaged local void fraction distribution as well as for the measurements of local mean axial velocity and turbulent intensity in the liquid phase. The signal processing scheme is optimized so it can be used in a very high void-fraction region toward the top of the pipe, which is the unique characteristic of bubbly two-phase flow in horizontal channels. To verify the accuracy of the proposed method combined effects of the local void fraction and liquid velocity measurements are checked against the global measurements of liquid flow rate. The results are found to be satisfactory within the experimental uncertainties. Furthermore, the area-averaged void fraction obtained from the hot-film probe measurements compared well with the quick-closing valve technique measurements. The results show that the hot-film probe method is accurate and reliable for the local measurements of void fraction, liquid velocity and turbulent intensity in horizontal bubbly flow provided that the data is processed properly. Some results of the local measurements of time-averaged void fraction, axial mean velocity and turbulent intensity at relatively low and high gas flows are also presented for a horizontal air-water bubbly flow in a 50.3 mm ID pipe.

INTRODUCTION

Void fraction is considered one of the most important parameters in gas-liquid two-phase flows from an engineering point of view. Several methods are available at present to measure void fraction. These are photographic, light attenuation, ultrasonic attenuation, double-sensor probe, impedance tomography, and Laser-Doppler Anemometer (LDA). These methods for measuring the void fraction are effective only in certain idealized cases. The photographic and light attenuation methods cannot be used with opaque walls and are limited to transparent dispersed two-phase flows with volumetric void fraction less than a few percent [1]. The ultrasonic method is not restricted to such conditions, and thus expands the measurement of the void fraction beyond the presently available range of fluids and non-opaque systems [2]. However, the ultrasonic attenuation method has a major limitation due to the reduction of the measurement certainty because of the scattering echoes, and thus it is

restricted to low void fraction bubbly systems. The X-ray computed tomography, impedance tomography and ring-type conductance transducer were used to determine the cross-sectional or volume averaged void fraction [3]. However, the local void fraction can not be measured by such technique.

Several attempts have been made to extend the use of LDA to bubbly flows [1,4]. In a very recent work of Suzanne et al. [5], it was concluded that at void fraction greater than about 2% the LDA signal is no longer suitable because of the increase of the beam interruption rate by the bubble crossing. In this case the hot-film anemometry was recommended.

It is to be noticed that with the exception of the work of Kocamustafaogullari and Wang [6], all of the bubbly flow experiments were carried out in *vertical* flow channels. Even in the case of well-studied vertical flow configurations, experimental results from fairly diverse sources are controversial regarding the void fraction distributions and the effects of the bubble size and flow conditions causing void profile transformation from a saddle shape into a convex shape. The difficulties in obtaining completely similar general results undoubtedly stem from our lack of understanding of the mechanisms involved in determining the internal structure of bubbly flow. Furthermore, due to basic internal structural differences between the vertical and horizontal bubbly flows, it is impossible to extend the vertical bubbly flow results to horizontal bubbly flows.

In light of the above discussion, it is evident that much experimental work is still necessary to attain a thorough physical understanding of the internal structure of horizontal bubbly two-phase flows. In view of the intention to measure local variables in a horizontal bubbly two-phase flow with local void fraction possibly ranging from 0-65%, it is unavoidable that a probe method must be used. In this context, an experimental investigation has been underway at the University of Wisconsin-Milwaukee to study the air-water bubbly two-phase flow characteristics along horizontal flow channels using the hot-film probe technique.

The primary purpose of this research is to show that the hot-film anemometry technique can be successfully used in horizontal bubbly two-phase flows

- to identify liquid and gas phases (phase separation), from which the local volume fraction can be evaluated,
- to evaluate the local time-averaged, axial liquid phase mean and turbulent fluctuating velocities,
- to measure the local void fraction and local bubble passing frequency of the two-phase flow, and finally,
- to investigate the dependence of the local parameters on other flow variables.

2. HOT-FILM ANEMOMETRY TECHNIQUE

2.1 Principle of Measurement

Hsu et al. [7] and Delhaye [8] were the first to study the response of hot-film probes in a liquid-gas two-phase flow. Since then, this technique has been used extensively [9-14] in vertical bubbly flow pattern. However, only limited efforts were made to examine two-phase flow characteristics in large scale experimental programs in horizontal bubbly flow channels.

In principle, the hot-film probe provides information about the flow field by relating the changes in this field to changes in the heat transfer at the probe tip surface. As the fluid flows past the constant temperature hot-film probe, changes in the fluid velocity, including turbulence fluctuations, cool the sensor at different rates. These changes in cooling rates result in voltage changes in the anemometer. In the case of an air-water two-phase flow, very sharp variations occur in the anemometer voltage output as the probe tip goes through a gas-liquid interface because the heat-transfer characteristics of air is completely different than water. A typical sensor output for two-phase bubbly flow is illustrated in Fig. 1. As seen in this figure the sensor encounters both liquid and small gas bubbles several times in a very short period. After the sharp initial drop, caused by the probe piercing the front of a bubble, the voltage gradually continues to decrease while the sensor stays inside the bubble. This is due to the evaporation of a thin film of liquid that remains on the sensor. On the other hand, the output signal from the probe shows a very sharp increase to the previous voltage level upon exiting the gas bubble due to wetting of the sensor. It is interesting to notice that, when the liquid wets the sensor, the signal rebuilds after a very short period during which it exhibits an overshoot. This is usually the case because the hot-film anemometer circuitry tends to overcompensate the voltage increase when liquid suddenly envelopes the tip of the probe.

In the upper portion of the pipe, the probe encounters plenty of bubbles, or partial bubbles hits, where the residence time in gas bubbles and liquid is too short to show the basic output characteristics of the probe and

consequently becomes harder to analyze such signals. When the probe is in the gas, the signal is no longer representative of the velocity, it is thus necessary to remove this part of the signal as discussed in the next section.

2.2 Signal Processing

2.2.1 Phase Separation

The first requirement in evaluating a two-phase flow with a hot-film probe is the ability to identify and differentiate the gas and liquid phases on a record of the anemometer signal. A number of investigators have reported utility of the hot-film anemometry in two-phase flows. In these investigations a variety of bubble detection techniques, consisted of detecting the voltage changes associated with a change in phase, have been used.

In the present investigation, Farrar et al. [15] and Lewis [16] methods were combined to develop a reliable detection technique based on an interactive amplitude and threshold procedure. This new technique tackled the inherent problems in high-speed, high void fraction bubbly flows. Serious problems associated with previous methods when applied to a horizontal bubbly flow can be summarized as follows: Firstly, very small bubbles or partial bubble hits produce signals that do not fall below the voltage level corresponding to the lowest continuous liquid phase velocity fluctuations. Therefore, they can not be detected. Secondly, the overshoot in the hot-film signal results in a significant negative slope during the decay process following the overshoot. This may be interpreted as being due to the passage of a bubble front interfaces. The overshooting may cause serious errors in time-averaged void fraction calculation or it might cause major incorrect evaluation of turbulence.

The voltage output was recorded on disk. The derivative of this output signal with respect to time was then calculated. This derivative represents the slope of the output signal. By plotting the anemometer output and the slope on the same time scale, the effects of a bubble striking the probe can be seen as in Fig. 2a & b. For each bubble passage, the slope signal shows a sharp negative spike for the nose of the bubble followed by a sharp positive spike for the tail of the bubble. The power required to heat the sensor in the gas phase is considerable less than in the liquid phase. Similarly, the positive spike in the slope signal is a result of the increase in power required to maintain the sensor temperature as the probe reenters the liquid phase. From here, it is a matter of determining the proper threshold values to detect the spikes in the slope signal.

The first threshold is used to determine the rear of the gas bubble. Its value must be positive. This slope threshold value is the most important because it has the largest magnitudes and is unaffected by any of the flow characteristics. Therefore, it is the easiest to detect. Its value should distinguish between the peaks caused by liquid interface and those from the turbulent fluctuations. The turbulence slope values were of a magnitude of less than 250. By plotting the anemometer output voltage data and the corresponding slope, as seen in Fig. 2a & b, the positive value of the slope can be recorded for each liquid slug occurrence by visual inspection. This was done for experimental data covering the entire range of gas and liquid flow rates. The rear of bubble was found to cause a positive peak with a magnitude greater than 500. This value was used as the threshold for the bubble rear detection or liquid slug beginning. When this threshold value is reached or exceeded, in the positive plane, the phase separation step signal, δ , is set equal to unity indicating the liquid phase (Fig. 2c).

Similarly, a second threshold value was found for the negative spike caused by the probe hitting a gas bubble. These negative peaks were found to have a magnitude greater than 300 in the negative plane. It is obvious from Fig. 2b that the magnitude of this slope is usually smaller than the previous one, because the drop in the voltage occurs gradually. So it is harder to detect and easier to be feigned by the turbulence fluctuations. This is why a conservative value of -500 has been used as a bubble front detection threshold. This value is used to identify the bubbles only with relatively clear tail voltage signal. The principal slope is going to be incorporated to double check the validity of the negative slope as discussed later.

To ensure that all bubbles have been detected and to take care of the overshooting, the program works backward whenever the first threshold occurs to indicate a start of liquid phase. Since this threshold is very distinct and impossible to miss, it sets up the base for the further signal analysis. The signal processing program works backwardly forcing all data to be gas until another first threshold value or a third threshold event (whatever comes first) takes place. The third assigned slope threshold value is of importance when the second threshold bubble start detection fails. Because some bubbles, small ones in particular, introduce intermediate negative slope, which may be hard to differentiate from velocity fluctuations negative slopes, the third slope threshold makes the detection of gas phase more lenient. Therefore its value is set to -250. This, in its absolute plane, is much less than the slope associated with interface passage but slightly greater than the slope of most velocity fluctuations. In this way we get a narrower band of liquid voltage signal, which results in detecting smaller bubbles. The third threshold works in conjunction with an amplitude threshold, which will be discussed in the next section.

When the entire data signal has been analyzed in this way, the program returns the phase separation step signal. This signal is used for the void fraction analysis and helps to assign the liquid phase data used for velocity analysis. One problem with the above method, and any other method involving an immersed probe in the two-phase flow, is as described by Wang et al. [17], the probe deforms and deflects the bubbles prior to piercing. This would lead to an underestimation of the void fraction.

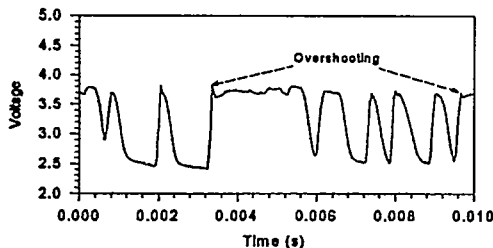


Figure 1. A Typical Hot-Film Output in a Horizontal Bubbly Flow

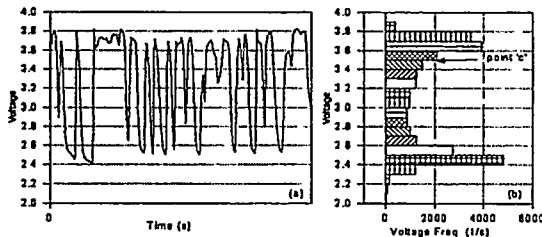


Figure 3. Determination of Threshold Voltage: (a) Sample Voltage Output; (b) Probability Density Function for Voltage Output.

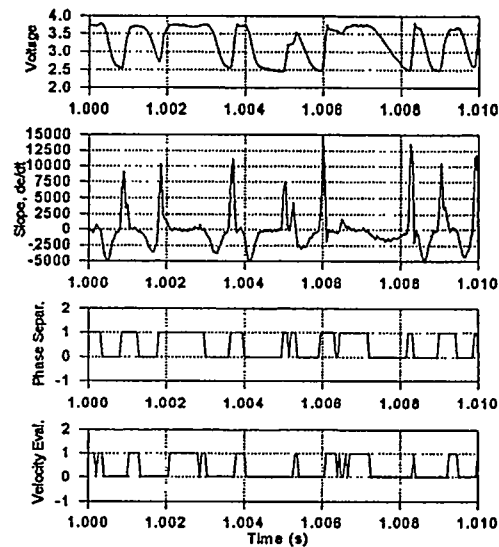


Figure 2. Anemometer Output and Signal Processing: (a) Anemometer Output Signal ; (b) Slope of Voltage Output ; (c) Phase Separation Step Signal ; (d) Velocity evaluation function.

2.2.2 Determination of Proper Data Set for Velocity Analysis

In the preceding section it was demonstrated that the proposed bubble detection technique can identify the starting and ending times of virtually every bubble event within hot-film signal. Nevertheless, using all identified liquid phase data for velocity analysis causes significant error. Similar to the phase separation method another method has been developed to identify the proper data set that should be used in liquid velocity data processing. The back-bone threshold value for this task is the voltage amplitude threshold. Unlike the previous technique, this one is only of practical use if a method of automatically determining suitable values for the amplitude can be identified. This was achieved by using the probability density function (pdf). Fig. 3 shows the digitized pdf corresponding to a large sample of hot-film probe data obtained at a certain probe position in a typical bubbly flow. A sample of the hot-film signal from which it was obtained is also shown in the figure. The pdf is observed to have a bimodal shape consisting of two peaks separated by a low level plateau region. The upper peak represents the high voltage associated with liquid phase, while the lower peak represents the low voltage associated with gas phase. In the current program the lower peak, which is located near the bottom of the hot-film signals, is not determined and thus our pdf is truncated to accommodate only the large peak. This peak corresponds to the voltage/velocity associated with the continuous phase turbulence. A point on the voltage scale of the pdf slightly below that corresponding to position "c" on Fig. 3 is an ideal choice for voltage amplitude threshold since it will be low enough to avoid mistaking any turbulence velocity fluctuations and high enough to detect the majority points in gas phase.

After identifying the amplitude threshold value internally by the computer program, the points with voltage higher than this threshold value and their slopes within the first and second threshold slopes are only considered for velocity analysis. The data points associated with over-shooting, at the rear of bubbles, are excluded again by proceeding backwards. By working backwards, the current point is compared with the previous few points. If the current point voltage is higher than the voltage threshold value and its slope is lower than the second slope, then it

is identified as overshooting provided that the immediate preceding points have the massive positive slope. In Fig. 2d, the velocity evaluation step signal is shown for the corresponding anemometer output voltage, slope, and phase separation. In this figure, unity indicates acceptable data point for velocity analysis, zeros are not admissible points and should be excluded from any further velocity analysis.

2.3 Statistical Processing of The Data

Although the actual voltage change in a hot-film probe signal due to the probe encountering the bubble is not important or accurate, the time that the probe is exposed to the bubble can be used to determine the local time-averaged void fraction, α , at any point, r . It is defined as a time-average of the concentration, $\delta(r,t)$, by:

$$\alpha(r) \equiv \lim_{T \rightarrow \infty} \frac{1}{T} \int_0^T (1 - \delta(r,t)) dt \quad (1)$$

where, δ , as a function of the space coordinate, r , and time, t , is equal to 0 if the probe sensor is in the gas phase and equal to 1 if the sensor is in the liquid phase. Equation (1) can be written in discrete form as follows:

$$\alpha(r) = \frac{1}{T} \sum_{i=1}^N (t_{2i} - t_{2i-1}) \quad (2)$$

where i indicates the i^{th} gas bubble and t_{2i-1} and t_{2i} define the time when the probe enters into the gas bubble and liquid, respectively, the number of gas bubbles passing the probe sensor in the total sampling time, t , is n .

The local mean axial liquid velocity and the values of turbulent fluctuations were calculated by using

$$U_{\text{mean}}(r) = \frac{1}{N} \sum_{k=1}^N u_k(r,t) \quad (3)$$

and

$$u'(r) = \sqrt{\frac{1}{N} \left[\sum_{k=1}^N [u_k(r,t) - U_{\text{mean}}(r)]^2 \right]} \quad (4)$$

respectively. In Eqs. (3) and (4), $u_k(r,t)$ is the instantaneous axial velocity for the k^{th} data point in the liquid phase, and N is the total number of data points in the liquid phase of the digital sample, $k = 1 \dots N$. To remove the error caused by the intermittent wave motion, the time-based filtering process was developed in calculating turbulence fluctuations, Iskandrani [18].

3. EXPERIMENTAL RESULTS AND DISCUSSIONS

A sample of the time-averaged local void fraction, α , liquid-phase mean axial velocity, U_{mean} , and the turbulence structure as presented by the turbulent velocity, u' , and turbulent intensity defined as $(u'/U_{\text{mean,local}})$, are described in Figures 4 and 5 for relatively low and high values of $\langle j_g \rangle$. The single-phase liquid flow measurements of axial velocity and turbulence structure corresponding to the same liquid flow rates, i.e., the same superficial velocity, $\langle j_g \rangle$, as the respective two-phase flow, are also shown on these figures as a reference. When the two-phase flow profiles are compared in these figures, it is evident that the void fraction, mean axial velocity, and turbulence structure distributions have similar behaviors. More detailed observations can be made in the following sections.

3.1 Void Fraction Profiles

As described above, the time-averaged local void fraction measurement is calculated by Eq. (2). The void fraction distributions are illustrated in Figures 4c and 5c. It is evident from these figures that the void fraction distribution shows a sharp decrease toward the bottom of the pipe and practically becomes zero at a certain probe position r/R , indicating the existence of a liquid layer free of voids except near the wall of pipe, where the profile of void fraction starts to build up again. This liquid layer thickness decreases by increasing gas flow rates at a given liquid flow. It covers a liquid region between $r/R = 0.2$ and $r/R = -0.8$ at $\langle j_g \rangle = 0.25$ m/s and between $r/R = -0.1$ to $r/R = -0.8$ at $\langle j_g \rangle = 0.8$ m/s, as shown in Figures 4c and 5c.

Bubbles tend to migrate toward the upper wall under the dominating influence of buoyancy force. Thus, the void fraction under all test conditions generally showed distinct peak near the top wall at about $r/R \approx 0.8$ to 0.9 . This range corresponds to 2.5-5.0 mm distance from the wall. This observation is more pronounced at high gas flow rates, since at low gas flow rates the void fraction profile peaks at the wall itself, or too close to not reachable by the finite probe size. This peak which appears in most cases, can be attributed to the increased hydraulic resistance of the liquid path between the bubble and wall which may cause a sharp decline in void fraction. This phenomena is identical to the one that has been observed in vertical bubbly two-phase flows [9, 10, 17] and in horizontal bubbly flow [6] using double-sensor resistivity probe.

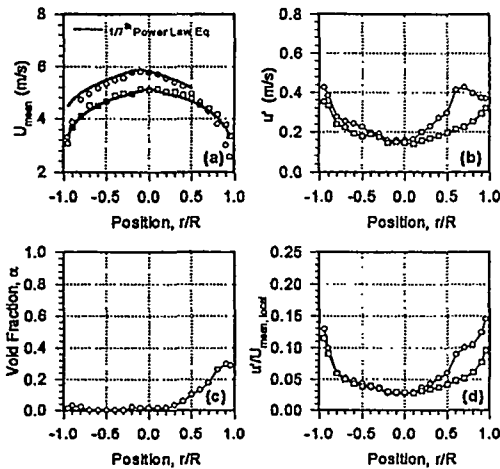


Figure 4. Two-Phase Flow Data for $\langle j_p \rangle = 4.4 \text{ m/s}$ and $\langle j_g \rangle = 0.25 \text{ m/s}$:
 (a) Local Mean Velocity; (b) Local Turbulence Velocity;
 (c) Local Void Ffraction; (d) Turbulent Intensity
 Distribution.

□ Single-phase data; ○ Two-phase data

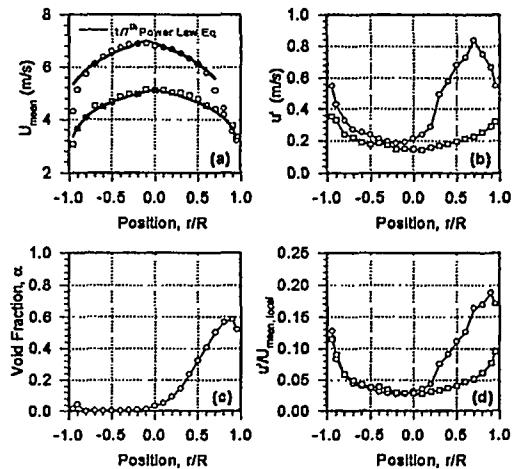


Figure 5. Two-Phase Flow Data For $\langle j_p \rangle = 4.4 \text{ m/s}$ and $\langle j_g \rangle = 0.80 \text{ m/s}$:
 (a) Local Mean Velocity; (b) Local Turbulence Velocity;
 (c) Local Void Ffraction; (d) Turbulent Intensity
 Distribution.

□ Single-phase data; ○ Two-phase data.

3.2 Mean Velocity Profiles

The mean velocity profiles as documented on Figures 4a & 5a show asymmetric character with the largest velocities located at the bottom part of the pipe. The degree of asymmetry is shown to decrease with increasing liquid flows or decreasing gas flow. An interesting feature of the velocity profile is that the velocity distribution within the bottom liquid layer exhibits a fully-developed turbulent flow character as demonstrated by the 1/7th power law profile. The 1/7th power law was fitted by the experimentally measured maximum velocity located in the liquid layer. Obviously, the maximum velocity in this 'liquid layer' occurs slightly off the pipe centerline (i.e. $-0.2 \leq r/R \leq 0$). It is interesting to note that although the value of this maximum velocity increases as either the gas or liquid flow rate increases, the location of the maximum remains almost unchanged.

It is evident that within the high population bubble region at the upper portion of the pipe the mean liquid velocity decreases sharply towards the upper pipe wall. Its values go even below the single-phase profile. This sharp drop in the liquid velocity may be attributed to two reasons. Firstly, when the bubbles present they induce additional turbulence which is called the bubble induced turbulence. As a result a sharp increase in turbulence due to presence of bubbles naturally reduces the mean local velocity. Secondly, increased bubble population toward the top of the pipe creates an additional resistance to liquid flow resulting in retardation of the liquid mean velocity in this region. These combined retardation of increased bubble population turbulence and the resistance to the liquid flow results in considerable reduction of the mean liquid velocity toward the top of the tube. On the other hand, the reduction of the liquid mean velocity in this region causes considerable increase of velocity in the rest of the pipe to maintain the overall continuity requirement. This observation is most pronounced at low liquid flow rates, since in this case bubbles are concentrated at the uppermost part of the pipe and plenty of room for the liquid (i.e. easier path) to flow.

3.3 Turbulence Structure

The turbulence structure is presented in terms of the axial turbulent fluctuation and the turbulent intensity as defined by $(u'/U_{\text{mean,local}})$. The turbulence fluctuations, u' , always increases when the gas introduced as seen in Figures 4b & 5b. In the lower part of the pipe, the slight increase is compared to the single-phase profile. However, at the upper part of the pipe where the population of bubbles is high, it substantially increases until it peaks and then drops down abruptly in the region next to the wall.

It is interesting to notice that the location where u' starts to build up is exactly the location where α distribution initiated to take off. Moreover, the level of void fraction profile determines the level of turbulence velocity. This indicates that the liquid turbulent velocity, u' , is a strong function of bubble population, i.e., bubble induced turbulence. This observation is similar to what is observed in vertical bubbly flow [11] and others that turbulent kinetic energy increases strongly with void fraction.

Figures 4d & 5d of turbulence intensity $(u'/U_{\text{mean,local}})$ further verify our results of u' values. The surprising identical trend of turbulence intensity in the lower part of the pipe between single-phase and two-phase confirm the liquid layer existence. That means introducing air has no effect on turbulence intensity in the liquid layer. On the other hand, the intensity increases rapidly as void fraction increases. It is very interesting to notice that $u'/U_{\text{mean,local}}$ is function of α for a certain setting of $\langle j_g \rangle$ and $\langle j_l \rangle$, unlike u' which is a function of the relative velocity too. This result is similar to the one reached by Lance and Bataille [11] for vertical bubbly flows. The $u'/U_{\text{mean,local}}$ profiles peaks next to the wall very similar to void fraction profiles. However, next to the lower pipe wall they are negligibly higher than single phase profiles because of the interactions of bubble-induced and wall-induced turbulence.

4. SUMMARY AND CONCLUSIONS

The internal phase distribution of concurrent, air-water bubbly flow in a 50.3 mm ID transparent horizontal pipeline have been experimentally investigated by using the hot-film anemometry technique. The gas volumetric superficial velocity changed from 0.25 to 0.8 m/s while the liquid volumetric superficial velocity kept fixed at 3.8 m/s. The time-averaged local values of the void fraction, the mean liquid velocity, and the liquid turbulence fluctuations were measured.

An improved digital processing method based on a combination of amplitude and slope thresholds has been developed to identify the phases in the hot-film anemometer output signal due to the passage of bubbles in a high-speed bubbly two-phase flow. This technique has proved successful in identifying virtually all bubble passages, including partial hits and very small bubbles and in determining the appropriate signal data for velocity analysis. The method has the advantage of incorporating the probability density function of the anemometer output signal to obtain automatically suitable value for the voltage amplitude threshold.

The experimental results indicate that the void fraction has a local maximum near the upper pipe wall. For the horizontal bubbly flow, the observed time-averaged local void fraction can reach as high as 65%. It was found that increasing the gas flow rate at fixed liquid flow rate would increase the local void fraction.

The axial liquid mean velocity showed a relatively uniform distribution except near the upper pipe wall, where a sharp reduction in velocity was noticed. The local mean liquid velocity and turbulence fluctuations increased with gas flow rate. It was also concluded that the local turbulent intensity is mainly a function of local void fraction.

ACKNOWLEDGMENTS

The work reported in this paper was performed under the auspices of the U.S. Department of Energy, Office of Basic Energy Sciences. The authors gratefully acknowledge the support of the U.S. DOE/BES under the direction of Dr. R. Price and Dr. R. Goulard.

REFERENCES

1. K. OHBA and T. ITOH, "Light Attenuation Technique for Void Fraction Measurement in Two-phase Bubbly Flow-II," *Experiment. Technol. Report*, Osaka Univ. 28 (1449) (1978)
2. H. P. BENSLEER, J. M. DELHAYE and C. FAVREAU, "Measurement of Interfacial Area in Bubbly Flows by Means of Ultrasonic Technique," *Proc. the Nat. Heat Transfer Conf.*, Pittsburgh, PA.(1987)
3. H. LEMONNIER and J. F. PEYTRAUD, "Is 2-D Impedance Tomography a Reliable Technique for Two-Phase Flow?" *OECD Meeting on Instrumentation*, Santa Barbara, CA. (1997)
4. T. G. THEOFANEOUS and J. SULLIVAN, "Turbulence in Two-phase Dispersed Flows," *J. Fluid Mech.* 116, 343 (1982)
5. C. SUZANNE, K. ELLINGSEN, F. RISSO and V. ROIG, "Local Measurement in Turbulent Bubbly Flows," *Nucl. Eng. and Des.* 184, 319 (1998)
6. G. KOCAMUSTAFAGULLARI and Z. WANG, "An Experimental Study on Local Interfacial Parameters in a Horizontal Bubbly Two-Phase Flow," *Int. J. Multiphase Flow* 17, 553 (1991)
7. Y. Y. HSU, F. F. SIMON and R. W. GRAHAM, "Application of Hot-Wire Anemometry for Two-phase Flow Measurements such as Void Fraction and Slip Velocity," *Proc. ASME Winter Meeting*, Philadelphia, PA.(1963)
8. J. M. DELHAYE, *Hot-Film Anemometry in Two-Phase Flow: Two-Phase Flow Instrumentation*, B. W. LE TOURNEAU and A. E. BERGLES, Eds., ASME, (1969)
9. A. SERIZAWA, I. KATAOKA and I. MICHIIYSHI, "Turbulence Structure of Air-Water Bubbly Flow-I. Measuring Techniques," *Int. J. Multiphase Flow* 2, 221 (1975a)
10. A. SERIZAWA, I. KATAOKA and I. MICHIIYSHI, "Turbulence Structure of Air-Water Bubbly Flow-II. Local Properties," *Int. J. Multiphase Flow* 2, 235 (1975b)
11. M. LANCE and J. M. BATAILLE, "Turbulence in the Liquid Phase in a Uniform bubbly Air-Water Flow," *J. Fluid Mech.* 222, 95 (1995)
12. T. J. LIU and S. G. BANKOFF, "Structure of Air-Water Bubbly Flow in a Vertical Pipe-I. Liquid Mean Velocity and Turbulence Measurements," *Int. J. Heat Transfer* 36, 1049 (1993a)
13. T. J. LIU and S. G. BANKOFF, "Structure of Air-Water Bubbly Flow in a Vertical Pipe-II. Liquid Mean Velocity and Turbulence Measurements," *Int. J. Heat Transfer* 36, 1061 (1993b)
14. T. HIBIKI, S. HOGSETT and M. ISHII, "Local Measurement of Interfacial Area, Interfacial Velocity and Liquid Turbulence in Two-Phase Flow," *OECD Meeting on Instrumentation*, Santa Barbara, CA. (1997)
15. B. FARRAR, A. L. SAMWAYS, J. ALI and H. H. BRUNN, "A Computer-Based Hot-Film Technique for Two-Phase Flow Measurements," *Meas. Sci. Technol.* 6, 1528 (1995)
16. S. LEWIS, *Use of Hot-Film Anemometry in Horizontal Slug Flow*, M.S. thesis at the University of Wisconsin-Milwaukee (1996)
17. S. K. WANG, S. J. LEE, O. C. JONES, JR. and R. T. LAHEY, JR, "Three-Dimensional Turbulence Structure and Phase Distribution Measurements in Bubbly Two-Phase Flow," *Int. J. Multiphase Flow* 13, 327 (1987)
18. A. ISKANDRANI, *Use of Hot-Film Anemometry in Horizontal Two-Phase Bubbly Flow*, M.S. thesis at the University of Wisconsin-Milwaukee (1997)

MICRO FOUR-SENSOR PROBE METHOD FOR INTERFACIAL AREA MEASUREMENT AND AREA TRANSPORT EQUATION

M. Ishii and S. Kim

School of Nuclear Engineering, 1290 NE
Purdue University, W. Lafayette, IN 47907-1290

ABSTRACT

A newly developed micro four-sensor conductivity probe is presented. The new probe is applicable to a wide range of two-phase flow and capable of acquiring the time-averaged local two-phase flow parameters of various types of bubbles. The data acquired by the probe are categorized into two groups in view of the two-group fluid particle transport; namely spherical/distorted bubbles as group 1 and cap/Taylor bubbles as group 2. Benchmark experiment employing the image analysis method is performed to validate the probe method, and a good agreement is observed. The data obtained by the probe in the bubbly and bubbly to slug transition condition is compared with the one-group interfacial area transport equation.

1. INTRODUCTION

In the two-phase flow system, the interfacial area concentration (a_i) and the void fraction (α) are two of the key geometric parameters in fluid particle transport and heat transfer capability. In view of detailed assessment of the given two-phase system, many two-phase system analysis codes employ the formulation using the two-fluid model[1], which is based on the detailed treatment of the phase interactions at the interface. However, since the two-fluid model solves the conservation equations for each phase separately, the phase-interaction terms arise. They are expressed in terms of a_i and the driving force such that

$$\text{(Interfacial Transfer Term)} \sim a_i \times \text{(Driving Force)}. \quad (1)$$

Therefore, the closure relation for the a_i is indispensable for accurate assessment of the two-phase flow system using the two-fluid model. In efforts of solving this closure problem in the two-fluid model, Kocamustafaogullari and Ishii[2] established the foundation in developing the interfacial area transport equation. It was followed by recent efforts by Wu et al.[3] and Kim[4]. Nevertheless, in order to evaluate the existing model, the detailed local measurement of the two-phase flow parameters should be established.

The conductivity probe was first proposed by Neal and Bankoff[5] accounting for the fundamental differences in conductivity between water and air. With the acquired signals from the multi-sensor probe, the local time-averaged two-phase flow parameters, such as α , and a , can be acquired. The double sensor conductivity probe has been employed in dispersed bubbly flow conditions, whereas the four-sensor probe has been applied in cap or slug flow conditions.

The measurement principle of the multi-sensor conductivity probe in obtaining the local time-averaged a_i , is based on the definition given by Ishii[1], such that

$$\bar{a}_i' = \frac{I}{\Delta T} \sum_j \left(\frac{I}{|v_i \cdot n_i|} \right)_j \quad (2)$$

where j denotes the j^{th} interface which passes a local point during the time interval, ΔT . Here, v_i and n_i are the bubble interfacial velocity and unit surface normal vector of the j^{th} interface, respectively. In view of this, Kataoka et al.[6] formulated a mathematical method to determine the local time-averaged a_i for both double-sensor and four-sensor probes. In the application of the double-sensor probe, it was suggested that

$$\bar{a}_i'(x_0, y_0, z_0) = 2N_i \frac{I}{|v_i| \cos \phi} \quad (3)$$

where N_i is the number of bubbles which pass the point (x_0, y_0, z_0) per unit time, and ϕ is the angle between the unit normal of the bubble interface and its interfacial velocity. In formulating equation (3), however, it was assumed that the bubbles are spherical in shape, and every part of the bubble has equal probability of being intersected by the probe. The application of the four-sensor probe, on the other hand, is important when the size of the bubbles become larger and they are no longer spherical in shape. In the four-sensor conductivity probe, the local a_i is acquired by acquiring three components of interfacial velocity. For example, when the directions of the three independent probes are chosen as the x , y , and z axes, the time-averaged a_i can be acquired[6] by

$$\bar{a}_i' = \frac{I}{\Delta T} \sum_j \left[\left(\frac{I}{v_{s1j}} \right)^2 + \left(\frac{I}{v_{s2j}} \right)^2 + \left(\frac{I}{v_{s3j}} \right)^2 \right]^{1/2} \quad (4)$$

Therefore, unlike the double-sensor probe technique, no hypothesis for the bubble shape is necessary in the mathematical formulation to calculate the local a_i .

In previous studies[7,8], however, some major shortcomings have been reported in applying the four-sensor conductivity probe, which had prevented the probe from being used in practice. These shortcomings included missing bubble signals and deformation of the bubble interface.

2. DEVELOPMENT OF THE MICRO FOUR-SENSOR CONDUCTIVITY PROBE METHOD

To minimize the limitations of the conventional probe, new designs are sought for the new probe configuration. Both the conventional and the newly designed four-sensor probes are illustrated in Figure 1. The significant reduction in the cross-sectional measurement area of the newly designed probe and its sharply tapered tips of the sensors can effectively minimize both the number of missing bubbles and the deformation of passing bubble interfaces. The new probe also accommodates the double-sensor probe capability in the four-sensor configuration, such that it can be applied in two-phase flow regimes spanning over bubbly, cap, slug, and churn-turbulent flow.

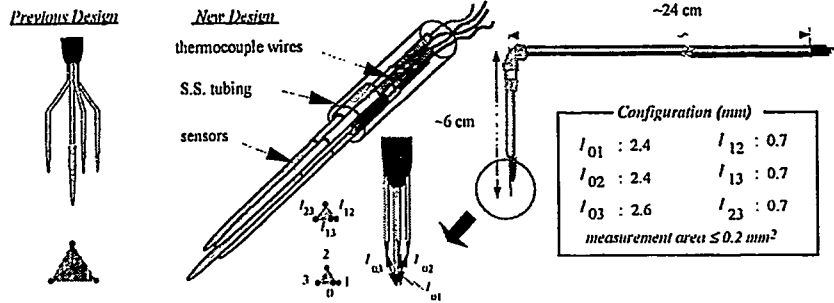


Figure 1. Schematic diagrams of the conventional and newly designed conductivity probes.

Furthermore, in the new signal processing scheme, the signals are categorized into signals of spherical, distorted, cap, and Taylor bubbles based on the bubble chord length information acquired by the common sensor (sensor 0 in Figure 1). In the present experiments, spherical and distorted bubbles are categorized as group 1, and the cap and Taylor bubbles are categorized as group 2. In identifying the bubble types, the maximum distorted bubble limit and the spherical bubble limit given by Ishii[9], and Ishii and Zuber[10] are used as criteria, such that

$$D_{ds} = 4 \sqrt{\frac{2\sigma}{g\Delta\rho}} N_{\mu_f}^{1/3}; \text{ spherical bubble limit where } N_{\mu_f} = \frac{\mu_f}{\left(\rho_f \sigma \sqrt{\frac{\sigma}{g\Delta\rho}}\right)^{1/2}} \quad (5)$$

and

$$D_{d_{\max}} = 4 \sqrt{\frac{\sigma}{g\Delta\rho}}; \text{ maximum distorted bubble limit} \quad (6)$$

Recently, in view of the double-sensor probe application, Wu and Ishii[8] suggested a correction method accounting for the missed interfaces. In this study, they considered the effects of the lateral movement of the bubbles and the probe tip spacing (l_{01} in Figure 1). By determining the calibration factor f , the formula given by Kataoka et al.[6] was improved as

$$\bar{a}'_i = f_{total} \left(\frac{2N_b}{\Delta s \Delta T} \right) \left(\frac{\sum_j (\Delta t_j)}{N_b - N_{miss}} \right) \text{ with } f_{total} = 2 + \left(\frac{v'_b}{\bar{v}_b} \right)^{2.25} \text{ for } \Delta s = 0.36 D_b \sim 0.86 D_b \quad (7)$$

where N_b is the number of total bubbles obtained, v'_b is the fluctuation of bubble velocity, \bar{v}_b is the average bubble velocity obtained by effective signals, and Δt_j , ΔT , Δs are the time delay obtained by effective signals for the j^{th} bubble interface, total sampling time at a local point, and distance between two tips of the sensors, respectively. For bubble sizes varying from 0.6 to 1.4 times the mean bubble size, it was found that the a_i calculated by equation (7) would result in a statistical error of $\pm 7\%$ for a sample size of approximately 1,000 bubbles[8].

For bubbles whose shapes are not spherical, the local time-averaged a_i is obtained by the signals acquired from the four sensors. Unlike the double-sensor method, the corrections for the defective signals from the distorted and cap bubbles are made in two steps in estimating the local a_i , such that

$$\bar{a}_{i,tot} = \bar{a}_{f,eff} \left(\frac{N_{tot}}{N_{f,eff}} \right) + \bar{a}_{r,eff} \left(\frac{N_{tot}}{N_{r,eff}} \right) \quad (8)$$

where $\bar{a}_{i,eff}$ is the average a_i calculated with effective bubble signals, N_{eff} is the number of effective bubble signals, N_{tot} is the total number of bubbles counted by the common sensor, and subscripts f and r denote front and rare bubble interfaces, respectively. Furthermore, in order to account for the

missing signals due to the steep interface of Taylor bubbles near the wall, the correction method by Ishii and Revankar[7] is employed such that

$$\bar{a}_{i,miss} = N_{miss} \cdot \frac{t_b}{\Delta T} \cdot \frac{\bar{l}_s}{A_s} \quad (9)$$

where N_{miss} is the number of missing Taylor bubble interface, t_b is the residence time of the missing bubble signals, ΔT is the total sampling time, \bar{l}_s is the average distance between three independent sensor pairs (i.e., l_{12} , l_{13} , and l_{23} in Figure 1), and A_s is the measurement area of the probe.

3. BENCHMARK OF THE PROBE

Two separate benchmark experiments employing the image analysis method are performed in order to validate both the double-sensor and the four-sensor method. The benchmark experiments for the double-sensor probe is performed in a transparent air-water vertical rectangular flow duct[11]. A computer code developed by Zhang and Ishii[12] is used to process the captured images to obtain the location and the diameter of each bubble. The typical result from the double-sensor probe benchmark experiment is shown in Figure 2. The relative percent difference between the two-methods is within $\pm 10\%$. Considering the limitation of the image method near the edge of the viewing window, the results from both measurement methods agree well.

In benchmarking the four-sensor probe, on the other hand, an adiabatic air-water two-phase flow loop of 5.08-cm ID with 375-cm in height is employed. Bubbles are generated through stainless steel hypodermic tubes of 0.12-mm in ID, which are arranged in a 20x20 square matrix. The probe is traversed by a micrometer at a fraction of 1.27-mm from the center to the wall of the test tube. In the present experiment, the gas flow rates are varied by $j_g=0.052$, 0.179, and 0.432-m/s while the liquid flow rate is fixed at $j_l=0.321$ -m/s. The data acquired by the probe is then benchmarked by the images of Taylor bubbles captured in the test loop as shown in Figure 3. From the captured images, the contour of the Taylor bubble is calculated with respect to the slug length assuming symmetric front and flat rear interfaces. The agreement between the calculated values and the experimental data is quite acceptable in both α and a_i . Some deviations may be due to the errors in estimating the Taylor bubble chord-length and to the fact that the image analysis assumes the smooth and symmetric front and flat rear interfaces.

4. EVALUATION OF THE ONE-GROUP INTERFACIAL AREA TRANSPORT EQUATION

The objective of developing the interfacial area transport equation is to replace the flow regime dependent correlations for the a_i in the thermal-hydraulic system analysis. The approach employing such correlation does not dynamically represent the changes in interfacial structure, such that it can not only induce non-physical oscillations in system behavior but limit the code accuracy. Therefore, improvements in the treatment of interfacial structure and flow regime transition will greatly enhance the capability of the system analysis codes. In what follows, the one-group interfacial area transport equation applicable to the two-phase flow in a round tube geometry is presented along with the evaluation results against the data acquired by the newly developed probe. For the detailed formulation procedures and the mechanistic modeling, however, authors recommend the readers to refer to references[3,4] given earlier.

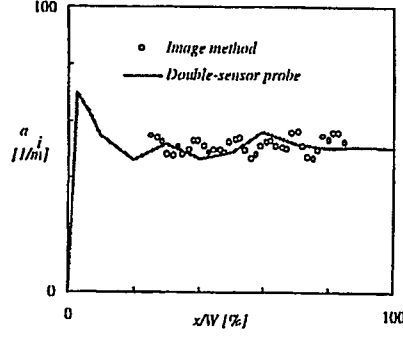


Figure 2. Typical results obtained from the comparison between the α_i measured by the double-sensor probe and that from image analysis. Here, W =half-width of the total flow duct width in the x -direction.

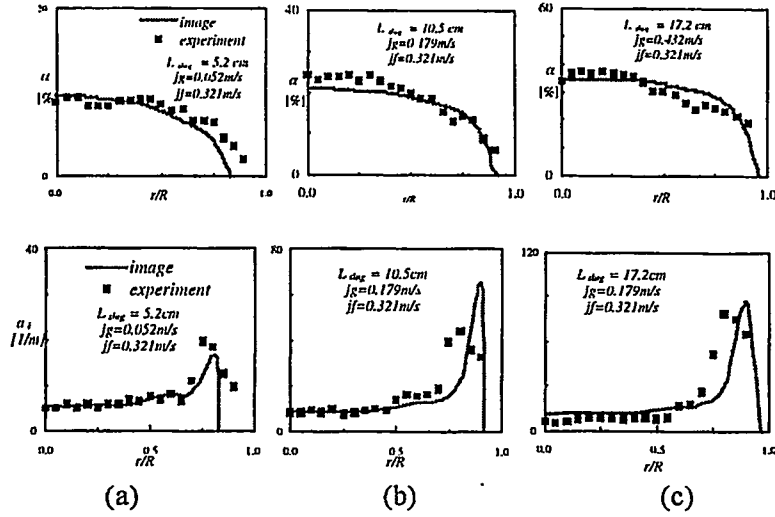


Figure 3. Comparison of the α and α_i between the experimental data and the values calculated based on the image analysis for flow conditions; j_f fixed at 0.321-m/s and j_g varied at (a) $j_g = 0.052$ -m/s, (b) $j_g = 0.179$ -m/s, and (c) $j_g = 0.432$ -m/s

In developing the one-group interfacial area transport equation, the source and sink terms are established through mechanistic modeling of major bubble interaction phenomena in the bubbly flow regime. These include the number source/sink rates stemming from; disintegration due to turbulent impact (TI), coalescence through random collision driven by turbulent eddies (RC), and coalescence due to the acceleration of the following bubble in the wake of the preceding bubble (WE). The one-group interfacial area transport equation is then given by

$$\frac{\partial a_i}{\partial t} + \nabla \cdot (a_i v_i) = \frac{2}{3} \left(\frac{a_i}{\alpha} \right) \left(\frac{\partial \alpha}{\partial t} + \nabla \cdot \alpha v_g \right) + \frac{1}{3\psi} \left(\frac{\alpha}{a_i} \right)^2 [R_{TI} - R_{RC} - R_{WE}] + \pi D_{bc}^2 R_{ph}^3 \quad (10)$$

where, the source and sink terms in the right hand side of the equation are given by

$$R_{TI} = C_{TI} \left(\frac{nu_t}{D_b} \right) \exp \left(-\frac{We_{cr}}{We} \right) \sqrt{1 - \frac{We_{cr}}{We}}, \text{ when } We > We_{cr} \quad (11)$$

$$R_{RC} = C_{RC} \left[\frac{n^2 u_r D_b^2}{\alpha_{max}^{11/3} (\alpha_{max}^{11/3} - \alpha^{11/3})} \right] \left[1 - \exp \left(-C \frac{\alpha_{max}^{11/3} \alpha^{11/3}}{\alpha_{max}^{11/3} - \alpha^{11/3}} \right) \right] \quad (12)$$

$$R_{WE} = C_{WE} C_D (D_b) n^2 D_b^2 u_r (D_b), \quad (13)$$

Here, the C_{TI} , C_{RC} , and C_{WE} are coefficients to be determined through experiments, and We_{cr} and α_{max} are the critical Weber number over which the bubble disintegrates and the maximum packing limit, respectively. In benchmarking the model against the data, equation (10) is averaged over the channel cross-sectional area to simplify the evaluation procedure. This assumes all parameters exhibit radially uniform profiles, so that the covariance terms are negligible. Furthermore, noting from the experimental data that the bubble size across the flow duct at a given axial level is nearly uniform, the α_i weighted bubble interfacial velocity is approximated by the void weighted bubble velocity. The local data are acquired in air-water vertical co-current adiabatic two-phase through the 2.54-cm ID and 5.08-cm ID tubes. In both test sections, the local measurements are made by traversing the conductivity probe in radial direction at three axial locations. The flow conditions of the present experiments are summarized in Table 1.

Table 1. Experimental conditions for the data employed in the model evaluation

Tube ID [cm]	Run No.	j_g [m/s]	j_f [m/s]
2.54	1-1	0.055	0.262
	1-2	0.078	0.262
	1-3	0.041	0.872
	1-4	0.143	0.872
	1-5	0.046	1.750
	1-6	0.257	1.750
	1-7	0.051	3.490
	1-8	0.201	3.490
	1-9	0.702	3.490
5.08	2-1	0.242	0.986
	2-2	0.321	0.986
	2-3	0.471	2.010
	2-4	0.624	2.010
	2-5	1.106	5.000
	2-6	1.790	5.000

In the present study, the coefficients in the model are determined based on the acquired data. In highly turbulent flow conditions, the *TI* and *RC* mechanisms are assumed to be dominant, whereas in low Reynolds number flow condition, *WE* is assumed to be dominant compared to *RC*. Furthermore, the constant C in *RC*, which accounts for the effective range of influence of eddies in driving bubbles to collisions, is assumed to be 3. In estimating the critical Weber number, it is varied from 2.3 to 8, based on the previous studies [13,14]. Then, the coefficients were determined by finding the values, which yield the best agreement with the experimental data. They were given by: $C_{WE}=0.002$; $C_{RC}=0.004$; $C=3.0$; $\alpha_{max}=0.75$; $C_{TI}=0.085$; and $We_{cr}=6.0$.

The results of the model evaluation are shown in Figure 4. The overall agreement between the model and the data is good within the measurement error of approximately $\pm 10\%$. Some deviations in transition flow conditions are observed due to the error associated with the presence of the group 2 bubbles. Nevertheless, it is of noteworthy that the one-group interfacial area transport equation generally predicts well in the wide range of bubbly flow conditions in different sizes of pipe flow.

The characteristic contributions from the individual source or sink terms to the total change in a_i are also plotted in Figure 5. Under the given flow conditions, the bubble expansion due to the pressure change (*EXP*) plays an important role in the increase in a_i . The contribution from the *TI* mechanism depends mainly on the given flow condition, such as liquid Reynolds number and the fluid particle Weber number, such that it is significant in Run 1-9, whereas it is minimal in Run 2-3. It can be also seen that the dominant mechanism among bubble coalescence mechanisms is attributed to *RC*.

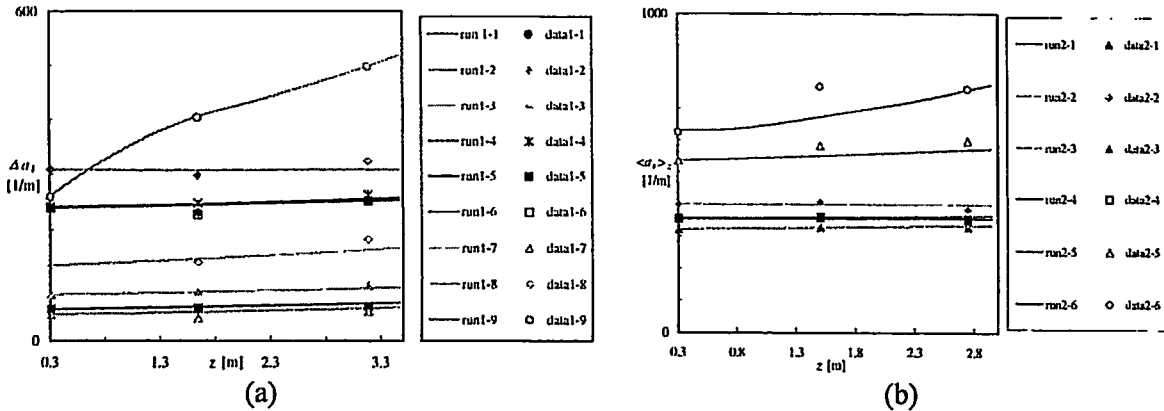


Figure 4. Evaluation of the Model with Experimental Data. (a) Data obtained in 2.54-cm ID pipe. (b) Data obtained in 5.08-cm ID pipe.

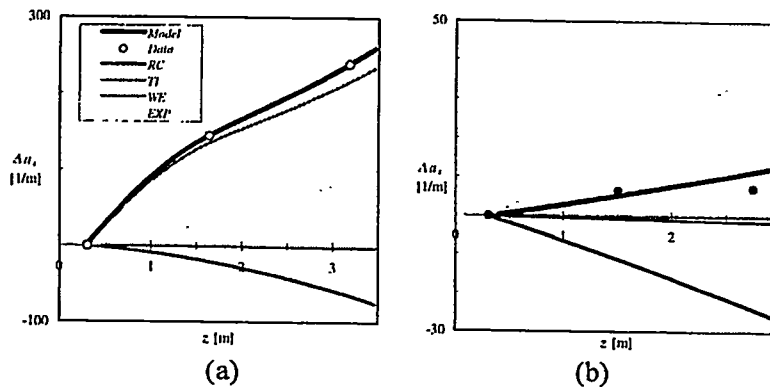


Figure 5: Contribution of individual bubble Interaction mechanisms to total change in a_i . (a) Run 1-9: $j_g=0.702\text{-m/s}$ and $j_f=3.49\text{-m/s}$ in a round pipe of 2.54-cm ID. (b) Run 2-3: $j_g=0.471\text{-m/s}$ and $j_f=2.010\text{-m/s}$ in a round pipe of 5.08-cm ID.

5. SUMMARY AND CONCLUSIONS

The newly designed micro four-sensor conductivity probe and its signal processing scheme are presented. The new probe not only minimizes the bubble deformation and missing bubble phenomena, but also accommodates the capability of a double-sensor probe for small bubbles. This feature enables one to establish the database for the two-group bubble transport. The signal processing scheme accounts for the missing and non-effective signals and is constructed such that the two-phase flow parameters of the different types of bubbles can be separated and categorized accordingly. A good agreement is observed in the benchmark test employing the image analysis method, which assesses both the newly designed probe and the measurement principles in the signal processing.

The one-group interfacial area transport equation applicable to the adiabatic air-water bubbly flow in round tubes is established. The development of the a_i along the flow path predicted by the model agrees well with the data. Active fluid particle interactions are well demonstrated through the sensitivity analysis on individual source and sink terms, which reflects the dominant mechanisms at various flow conditions. Under the present experimental conditions, the RC mechanism plays a dominant role in bubble coalescence as a sink term, whereas the contribution from the TI mechanism varies depending on the Reynolds number and the particle Weber number.

ACKNOWLEDGEMENTS

The authors wish to express their sincere appreciation to Drs. R. Goulard and R. Price of DOE/BES for their support. This study was performed at Purdue University under the auspices of the U.S. Department of Energy.

REFERENCES

1. M. Ishii, *Thermo-Fluid Dynamic Theory of Two-Phase Flow*, Collection de la Direction des Etudes et Recherches d'Electricite de France, Eyrolles, Paris (1975)
2. .Kocamustafaogullari and M. Ishii, Foundation of the interfacial area transport equation and its closure relations, *Int. J. Heat Mass Transfer*, **38**, No. 3, pp. 481-493 (1995)
3. Q. Wu, S. Kim, M. Ishii, and S. G. Beus, One-group interfacial area transport in vertical bubbly flow, *Int. J. Heat Mass Transfer*, **41**, Nos. 8-9, pp. 1103-1112 (1998)
4. S. Kim, Interfacial area transport equation and measurement of local interfacial characteristics, *Ph.D. Thesis*, School of Nuclear Engineering, Purdue University, Dec. 1999 (1999)
5. L. G. Neal and S. G. Bankoff, A high resolution resistivity probe for determination of local void properties in gas-liquid flow, *AIChE J.*, **9**, pp. 490-494 (1963)
6. I. Kataoka., M. Ishii, and A. Serizawa, Local formulation and measurements of interfacial area concentration in two-phase flow, *Int. J. Multiphase Flow*, **12**, No. 4, pp. 505-529 (1986)
7. M. Ishii and S. T. Revankar, Measurement of interfacial area using four-sensor probe in two-phase flow, *Purdue University Technical Report*, PU NE-91-1 (1991)
8. Wu, Q. and Ishii, M., Sensitivity study on double-sensor conductivity probe for the measurement of interfacial area concentration in bubbly flow, *Int. J. Multiphase Flow*, **25**, No. 1, pp. 155-173 (1999)
9. M. Ishii, One-dimensional drift-flux model and constitutive equations for relative motion between phases in various two-phase flow regimes, Argonne National Laboratory Report, ANS-77-47 (1977)
10. M. Ishii and N. Zuber, Drag coefficient and relative velocity in bubbly, droplet or particulate flows, *AIChE J.*, **25**, p 843 (1979)
11. Q. Wu, S. Kim, D. McCreary, M. Ishii, and S. G. Beus, Measurement of interfacial area concentration in two-phase bubbly flow, *ANS Transactions*, 1997 ANS Winter Meeting, Albuquerque, NM, Nov. 10-20, TANSO 77, p. 437 (1997)
12. G. Zhang and M. Ishii, Isokinetic sampling probe and image processing system for droplet size measurement in two-phase flow, *Int. J. Heat and Mass Transfer*, **38**, p. 2019 (1995)
13. M. J. Prince, and H. W. Blanch, Bubble coalescence and break-up in air-sparged bubble columns, *AIChE J.*, **36**, No. 10, pp. 1485-1499 (1990)
14. M. Ishii and T. C. Chawla, Local drag laws in dispersed two-phase flow, *Argonne National Laboratory Report*, ANL-79-105, NUREG/CR-1230 (1979)

THEORY OF SUBCOOLED BOILING

S. G. Bankoff¹ and S. H. Davis²
Chemical Engineering Department¹
Eng. Sci. and Applied Math. Department²

Northwestern University
Evanston, IL 60208 USA

ABSTRACT

A broad theoretical attack has been made on all phases of subcooled boiling, as evidenced by the publication or submittal of five papers in leading journals in the 1999-2000 period. For details, the reader is referred to these publications. Here we give a broad outline. These have included nucleate, transition and film boiling. Nucleate boiling is perhaps the most interesting, because of the enormous steady heat fluxes attainable ($>30 \text{ MW/m}^2$), but also the most complex and difficult. An analogous, but somewhat simpler, problem is that of a vapor bubble confined between two parallel plates, one of which is heated and the other cooled. Simultaneous evaporation and condensation occurs. This latent heat transport is thought to be the dominant heat transfer mode in subcooled nucleate boiling. There is a transition region between the nearly-circular advancing bubble front in the parallel-plate (or thin capillary tube) problem, behind which an ultrathin liquid film is deposited, and thus evaporates on the heated wall. The initial thickness of this film depends on the bubble front velocity. By asymptotic matching of the transition region with the curved interface, it was established that this thickness is proportional to $(Ca)^{2/3}$, where the capillary number, Ca , is a dimensionless bubble velocity. Previously, it had been thought that it was proportional to $(Ca)^{1/2}$. Another study showed that on imperfect (coated) surfaces, it was possible to obtain on a stable, microscopically-thin (1-3 nm) liquid film on the heated wall, owing to the combined presence of conjoining and disjoining presences in an apolar liquid. These arise from molecular dispersive forces from the top and bottom of the coating. This permits stable good wetting, resulting in complete utilization of the locally-available coolant. This may resolve a 50-year old puzzle as to how such enormous heat fluxes are possible.

The stirring action of a growing and collapsing bubble while attached to the heating wall was simulated by considering a periodically-oscillating wedge with constant apex angle with a heated wall in a semi-infinite liquid. The linearized equation was solved by transform methods and Floquet analysis, and showed multiple vortices developing and migrating.

Film boiling, in which a thin vapor layer is interposed between the subcooled liquid and the hot solid, is also important for its negative aspects in nuclear reactor accidents and burnout of heat transfer equipment. The equilibrium base state has traditionally been taken to be a quiescent uniform vapor film. However, as the wall temperature is progressively reduced, a nonlinear bifurcation takes place, which may be supercritical (bounded) or subcritical (possibly unbounded). By integrating along the nonlinear branches, some fascinating phenomena are revealed, such as stable or unstable, steady states or traveling waves, and hysteresis loops. Convection in the film parallel to the plate leads to accumulation points for vapor, which are incipient bubbles.

At a later stage liquid tongues penetrate the horizontal film, making contact with the solid surface. These contacts may grow or shrink, depending upon, among other things, the evaporation rate and the liquid downflow rate. A wetting/dewetting map was thus constructed, giving the neutral stability line for the onset of transition boiling, and the minimum film boiling temperature.

INTRODUCTION

Significant new insights have been published in the past year on subcooled boiling, in which the bulk liquid is below the saturation temperature. Subcooled boiling can reach steady heat fluxes above 30 MW/m^2 [1] in a relatively simple device, which makes it the heat transfer mode of choice in several high-heat-flux applications. A major barrier to the further densification, and hence miniaturization, of computer chips is the need for steady heat removal from concentrated sources. Plasma studies, leading towards eventual realization of fusion energy, and intense photon beams for material property studies (Argonne National Lab) are other sources of very large steady heat fluxes. On the other side of the coin, operation at such high fluxes implies that instabilities, leading to film boiling rather than nucleate boiling, are of concern because of possible equipment damage, melting and even vapor explosions, as in the Chernobyl accident. Despite a large number of investigations over the past half-century, knowledge of the mechanics of flow and heat transfer in boiling systems is based on small-scale experiments and phenomenological models. These have been useful, but our approach represents a new attack on the problem.

SUBCOOLED NUCLEATE BOILING

In highly-subcooled nucleate boiling, enormous numbers of tiny bubbles grow and collapse while attached to the heating surface. Because they never detach, the bulk liquid remains free of vapor, in contrast to the usual situation in saturated boiling. Despite this important simplification, experimental information remains scarce, since the bubble maximum radii are of order 1-mm, with millions of bubbles with lifetimes of order 1 ms. There has therefore been a controversy for the past 50 years concerning the principal mechanism for this extraordinary heat transfer. One might suppose that it lies in the latent heat transport by the vapor, but this has been discounted on the basis of visual vapor volumetric generation rate, and calculation of evaporation rate from the thin liquid microlayer at the base of the growing bubble. Alternative possibilities include stirring of the liquid between the bubbles and quenching of the dry solid when the liquid returns after bubble collapse. The former mechanism has been studied by Tilley, et al. [2] However, it is readily shown that neither of these possibilities can account for average surface heat transfer coefficients of the order of $1 \text{ MW/m}^2 \text{ K}$. On the other hand, condensation heat transfer rates of $60\text{-}80 \text{ MW/m}^2$ were measured by Bankoff and Mason [3] at the surface of an oscillating bubble resulting from the injection of steam in

a turbulent water stream, with similar dimensions and cycle, so that the latent heat mechanism seems plausible. But how was the required vapor rate to be achieved?

The assumption has been that the thin liquid microlayer at the base of the growing bubble remains immobile once it has been deposited by the advancing bubble front. A simpler analog to the bubble growing in an infinite sea of liquid is a bubble confined between two parallel plates, one of which is heated and the other cooled. If the microlayer remains locally immobile as it evaporates, the film can become discontinuous, since the local time of dryout depends on the film thickness that was deposited at that location when the bubble passed over it at some previous time. Wilson, Bankoff and Davis [4] found, by asymptotic matching of the transition region to the curved bubble front, that the local thickness at deposition was proportional to the capillary number (or dimensionless bubble wall velocity) to the $2/3$ power, instead of square root, as previously assumed. Furthermore, in a long tube the bubble wall velocity can be discontinuous more than once.

This was a first step towards the computation of a single bubble, and of an array of bubbles, growing and collapsing on a heated wall in subcooled nucleate boiling.

The next clue was provided by a study by Bankoff and Oron [5] of the dryout of an evaporating ultrathin film on a coated hot surface. A model by Vold [6] for a pure, apolar, isothermal liquid acting on a coated colloidal particle, was extended to the case of a thin film of non-isothermal apolar liquid acting on a coated (oxide, organic material or other contaminant) solid evaporating to dryness. This leads to a two-term van der Waals exponent pair in the evolution equation, corresponding to simultaneous conjoining/disjoining pressures resulting from attractions from the bottom and top of the coating for the vapor-liquid interface. This is in contrast to the [3,9] exponent pair usually used, which leads to attraction, but not repulsion until the solid surface is actually reached. With the [3,4] potential a stable liquid precursor film is produced, which may be 1-3 nm in thickness. This would correspond to complete wetting. Furthermore, hydrodynamic, rather than adsorption/desorption, equations are appropriate for films of this thickness. The apparently dry area, which appears on the heated surface, grows and pushes the remaining liquid into drops surrounded by ultrathin film. Because of the enormous evaporation rates from the ultrathin film, the drops shrink, acting as reservoirs under the difference in conjoining pressures, until they disappear. All liquid quickly then evaporates. This is in contrast to the case considered by Burelbach, Bankoff and Davis [7] for a poorly-wetted surface, in which local dryout occurs as soon as the free-surface wave reaches the solid surface. Very little of the liquid has been evaporated at that point. With a wetted surface the process is efficient, in that all of the coolant is utilized. It appears that this may explain the 50-year old paradox, but more data are needed to test this theory.

Practical Significance

Wettability of the heating surface thus may be important in determining the efficiency of high-flux heat transfer. This may call for special surface treatment.

TRANSITION BOILING

Once film boiling is established a relatively quiet film of vapor separates the heated surface from the bulk liquid. However, close to the minimum film boiling temperature, tongues of liquid penetrate the film and touch the surface. The contact is generally unstable, and the tongues retract. However, a critical condition exists under which the contacts spread and cover the surface. This is known as transition boiling, leading to full-fledged nucleate boiling. Joo, Davis and Bankoff [8] offered a simple hydrodynamic theory for this process, in which an inviscid liquid column flows downwards, being simultaneously evaporated at the solid surface. For the first time a phase diagram was produced which showed the critical condition for wetting/dewetting as a function of liquid downflow rate and solid thermal resistance, other factors being held constant. Extensions are

intended which will take into account capillary effects in spreading and explore the parameter space more fully.

Practical Significance

This is the first map which has been published for wetting/dewetting of hot dry surfaces under a vapor layer, which marks the onset of transition boiling and the minimum film boiling temperature. Long-range conjoining/disjoining pressures, as above (Oron and Bankoff [5,9], together with capillary effects, need to be brought in.

FILM BOILING

Before the stable film actually produces down-flowing tongues of liquid, there is a critical heat flux at which the smooth quiescent vapor film surface becomes unstable. At this point a bifurcation takes place, which may be supercritical or subcritical. Exploration by Panzarella, Davis and Bankoff [10] of these nonlinear branches reveals the existence of stable or unstable steady states or traveling waves, possible existence of hysteresis loops, and accumulations of vapor which are the precursors to bubble formation and removal. Weakly-nonlinear stability analyses of this type, leading at the third order to Landau-Ginsberg equations for the nonlinear growth of the wave amplitude are well-known, but have never been applied previously to film boiling. This is the first rigorous exploration into the nature of film dynamics in horizontal film boiling.

OTHER WORK

Other work published in the past year supported by this grant was a study of a slender dry patch on an inclined plate in a draining liquid film by Wilson, Duffy and Davis [11], relevant to the dewetting problem, spreading and imbibition of a viscous liquid on a porous base by Hocking and Davis [12], and the dewetting of hot coated surfaces by Bankoff and Oron [13].

ACKNOWLEDGMENT

This work was supported by the Department of Energy.

REFERENCES

1. F. C. GUNTHER, "Photographic Study of Surface-Boiling Heat Transfer to Water with Forced Convection," *Jet Propulsion Laboratory*, Pasadena, CA, Progress Report No. 4-120 (1950).
2. **B. S. TILLEY, S. G. BANKOFF and S. H. DAVIS, "Unsteady Stokes Flow near an Oscillating Heated Contact Line", *J. Fluid Mech.*, submitted.
3. S. G. BANKOFF and J. P. MASON, "Heat Transfer from the Surface of a Steam Bubble in Turbulent Subcooled Stream", *AIChE J.* 8, 63-65 (1962).
4. S. K. WILSON, S. H. DAVIS, and S. G. BANKOFF, "The Unsteady Expansion and Contraction of a Long Two-dimensional Vapour Bubble Between Superheated or Subcooled Parallel Plates", *J. Fluid Mech.* 391, 1-27 (1999).
5. *A. ORON and S. G. BANKOFF, "Dewetting of a Heated Surface by an Evaporating Liquid Film under Conjoining/Disjoining Pressures", *J. Colloid and Interf. Sci.*, 218, 152-166 (1999).

6. M. J. VOLD, "The Effect of Adsorption on the van der Waals Interaction of Spherical Colloidal Particles", *J. Colloid Sci.*, 16, 1-12 (1961).
7. J. P. BURELBACH, S. G. BANKOFF and S. H. DAVIS, "Nonlinear Stability of Evaporating/Condensing Films", *J. Fluid Mech.* 195, 463-494 (1988).
8. S.W. JOO, S. H. DAVIS and S. G. BANKOFF, "Hydrodynamic Model for Transition Boiling". *J. Fluid Mech.*, 402, 195-201 (2000).
9. *A. ORON and S. G. BANKOFF, "Dewetting of Coated Hot Surfaces" (2000). *Proc. IUTAM Symposium on Nonlinear Waves in Multiphase Flow* (in press).
10. C. H. PANZARELLA, S. H. DAVIS and S. G. BANKOFF, "Nonlinear Dynamics in Horizontal Film Boiling". *J. Fluid Mech.*, (2000) 402, 164-194.
11. S. K. WILSON, B. R. DUFFY and S. H. DAVIS, "On a Slender Dry Patch in a Liquid Film Draining under Gravity Down an Inclined Plane". *Euro. J. Appl. Math* (in press).
12. L.M. HOCKING and S. H. DAVIS, "Spreading and Imbibition of a Viscous Liquid on a Porous Base. Part II" (2000). *Phys. Fluids* (in press).

* Partial support from US-Israel Binational Science Foundation

**Partial support from National Science Foundation

COMPLEX DYNAMICS IN LARGE ARRAYS OF FLUID-ELASTIC OSCILLATORS

F.C. Moon, *Cornell University, Ithaca, New York USA*

M. Kuroda, *Mechanical Engineering Laboratory, MITI, Tsukuba, Ibaraki, Japan*

Abstract

New experiments on the dynamics of 90 and 300 elastic oscillators in a steady cross flow are described. Unlike the single row dynamics, which lead to limit cycle behavior, multi-row arrays seem to exhibit chaotic though not necessarily, low dimensional dynamics, at a critical flow value. With increasing flow velocity however, organized wave-like structures appear to develop. Experimental models of this type may serve to help understand complex dynamics in large array heat exchange systems. It may also be a model to understand wind crop dynamics and damage.

INTRODUCTION

Fluid-elastic vibrations occur in heat exchanger systems, agricultural crop-wind interactions and bio-mechanical problems such as ciliated epithelia. Classic problems include the flow of fluid through tube structures and around tubes and have generally focused on linear dynamics. In this study we discuss experimental nonlinear dynamics of a large array of up to 300 cylinders in a cross flow. The rod-like structures are cantilevered at a base and free to vibrate at the top. (Figure 1) The coupling between rods consists of fluid forces and contact when the vibration amplitude becomes too large. The fluid forces are of two types; fluid-elastic nearest neighbor forces equivalent to springs and dampers, and non-nearest neighbor forces produced by vortices leaving the forward rows of cylinders and effecting the dynamics of the rearward rows of cylinders.

Observations of the tip vibration dynamics reveal complex patterns of motions of the rods, some of which appear nearly stationary, others vibrate in a straight-line motion in-line and at an angle to the upstream flow and others vibrate in elliptical patterns sometimes associated with rod to rod contact. While the rod frequencies lie close to their natural frequencies, the phases and types of motion, i.e., stationary, straight-line and elliptic show no regular pattern and change in time. It is important to emphasize that the linear theory would predict $2 \times N \times M$ eigenmodes for a $N \times M$ array of rods. However, no

clear modal pattern emerges as the wind tunnel velocity is increased. Thus, we have sought to apply entropy measures of complexity to describe the dynamics.

DESCRIPTION OF EXPERIMENT

The wind tunnel is a low turbulence system with a 25.6 cm x 25.6 cm cross section. The 17.1 cm long rods were steel with a diameter of 1.59 mm and a spacing between rod centers of 3.2 mm or a gap equal to the rod diameter. The Reynolds number based on the rod diameter ranges from 200-900. Although the base holes are precisely regular, the spacing of the ends of the rods varied slightly from a periodic spacing due to small initial curvature in the rods. The data reported in Figures 2,3 are for a 3 row by 30 rod array, as shown in Figure 1. However, another experiment involves 10 rows of 30 rods. Dynamic data are obtained by instrumenting one or two rods as well as video taping of the motion of the ends of the rods of the entire array. Also photographic images with a shutter speed on the order of the vibration period for 10 Hz were taken. The wind speeds ranged from 0-10 m/s, but no significant dynamics were observed below 2 m/s.

The 90 rod experiments were extended to 300 rods of the same diameter and spacing with 10 rows of 30 rods. In these experiments, the flow behind the 10 row array in a cross flow was measured with a pitot tube. The results are shown in Figure 4. The data shows that the array acts as a porous rigid object in the flow with most of the flow directed around the sides and over the top of the rods. There still is significant flow through the array however. In addition an accelerometer was fixed to the middle rod in the last row. Power spectra and probability distribution of accelerations were also measured. Video data was recorded to show the wave-like structures in the flow.

RESULTS

To describe the vibration patterns in the 90 rod array photographs were taken at different wind speeds from the onset of vibrations, around 2 m/s to 9 m/s. We use an entropy measure based on three symbols corresponding to the three types of motion; stationary, straight-line and elliptical orbits. A typical pattern is shown in Figure 3. Although the states of each rod varied in time, it was found by observation of the video records that the photographic pattern gave a good sample of the average patterns.

In Figure 2, we show the number of rods in straight-line and elliptical orbits as a function of wind speed. Clearly, one can see an onset of motion at a critical speed and the growth of the number of rods in elliptical motions. This may be related to the greater

incidence of rod impact at the higher wind velocities. The data also shows hysteresis for increasing and decreasing flow.

Data was also taken for the array at an angle to the flow direction. The same phenomena occurs as in the head-on flow case except near the 90 degree flow case where there are 30 rows of 3 rods each. In this case, there is very little motion as the array seems to act as an airfoil and directs the flow around the array instead of through it.

For the 300 rod array, velocity measurements (Figure 4) show that the collective action of the rods screens the flow, forcing a large fraction around the sides and over the top. However there is no indication that the edge rods experience more or less vibration. Video pictures clearly show that all the rods participate, sometimes in wave-like motion transverse to the flow direction. Also the accelerometer data on one of the rods, (Figure 5) shows bursting phenomena probably related to impact between the rods as the flow velocity is increased. We are trying to be able to take data from the video records in order to obtain more collective dynamic measurements.

ENTROPY MEASURES

Several pattern entropy measures were used, based on the entropy measure

$$S = \sum p_n \log(1/p_n)$$

where p_n is a probability measure of a certain spatial pattern occurring. These measures of local cluster pattern show an increase in entropy with flow velocity.

REFERENCES

1. Coutts, M.P., Grace, J. (1995) Editors. *Wind and Trees* Cambridge University Press, Cambridge, U.K.
2. Finnigan, J.J. (1979) "Turbulence in Waving Wheat" *Boundary Layer Meteorology* 16, 181-211.
3. Finnigan, J.J., Mulhearn, P.J. (1978), "Modeling Waving Crops in a Wind Tunnel", *Boundary-Layer Meteorology* 14, 253-277
4. Grace, J. (1977) *Plant Response to Wind* Academic Press, London

5. Inoue, E., 1955, Studies of Phenomena of Waving Plants ("HONAMI") Caused by Wind". *Agric. Meteorol. (Japan)* 11, 18-22.
6. Lunley, J.L. & Panofsky, H.A. 1964, *The Structure of Atmospheric Turbulence*, Wiley-Interscience, NY 239.
7. Moon, F.C. (1992) *Chaotic and Fractal Dynamics* J. Wiley & Sons, N.Y.
8. Moon, F.C., Kuroda, M. (2000), "Complexity Measures in Large Arrays of Fluid Elastic Oscillators" *Chinese J. mechanics* (to appear).
9. Niklas, K.J. (1992), *Plant Biomechanics*, Chapters 7,9. University of Chicago Press.
10. Williams, G. P. (1999), *Chaos Theory Tamed*, Joseph Henry Press, Washington, D.C.
11. Raynor, G.S. "Wind and Temperature Structure in a Coniferous Forest in a Contiguous Field", *Forest Science* 17 (3), 351-363.
12. Thothadri, M., Moon, F.C. (1998) "Helical Wave Oscillations in a Row of Cylinders in a Cross-Flow" *J. Fluids and Structures* 12, 591-613.
13. Thothadri, M., Moon, F.C. (1999) "An Investigation of Nonlinear Models for a Cylinder Row in a Cross Flow" *J. Pressure Vessel Technology*; ASME 121, 133-141.

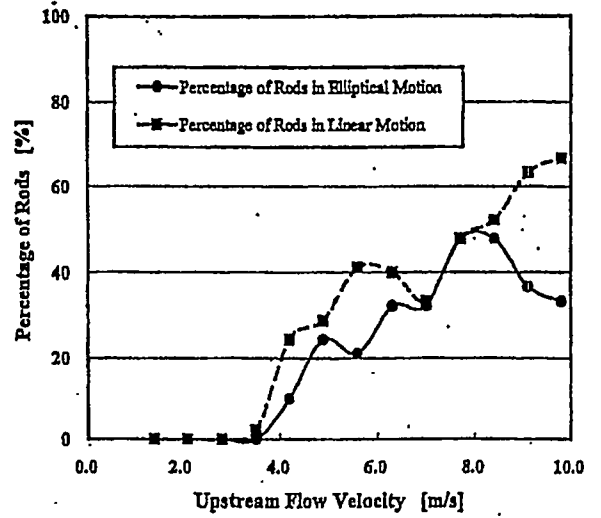
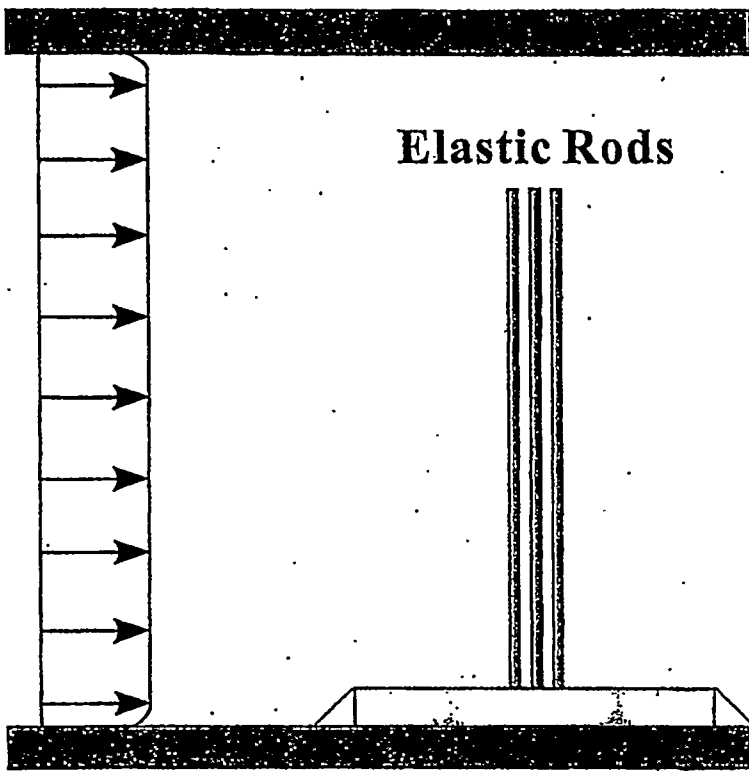


Fig. 1 Schematic diagram of the experimental setup Fig. 2 Percentages of the rods in straight-line motion and those in elliptical motion

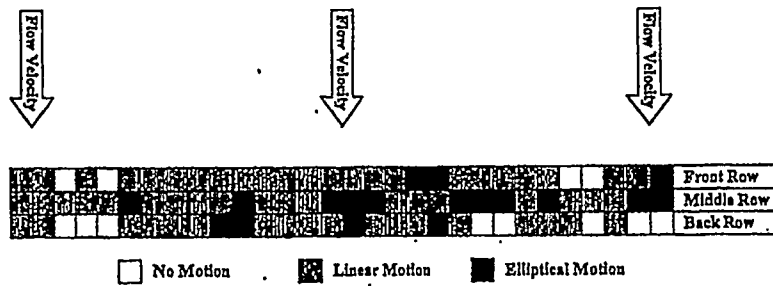


Fig. 3 Spatial pattern at flow velocity 5.6 M/S

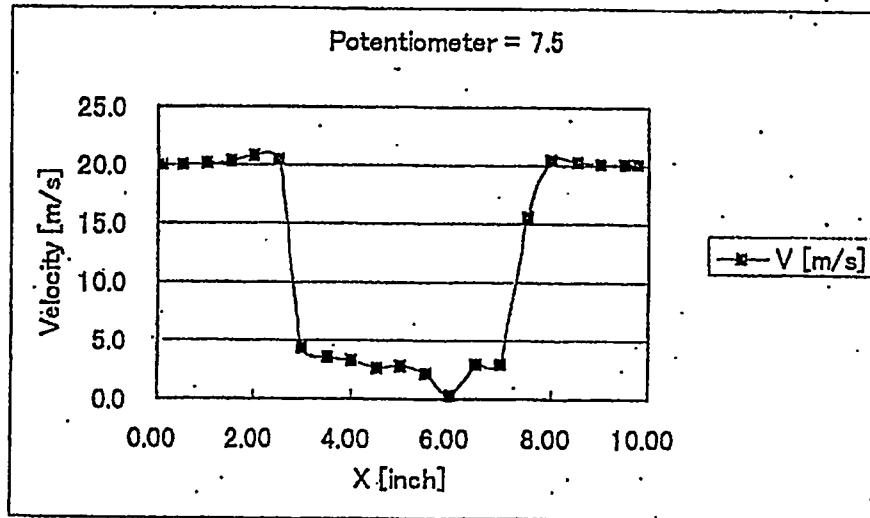
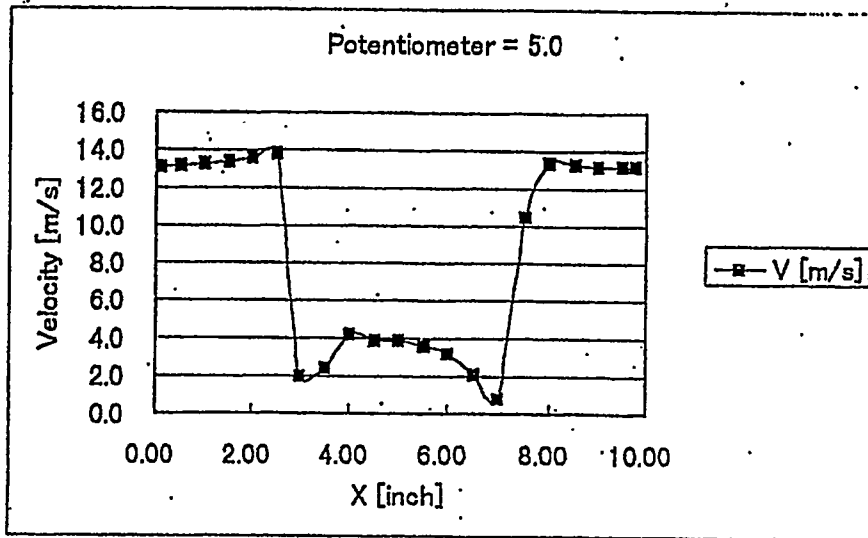


Fig. 4

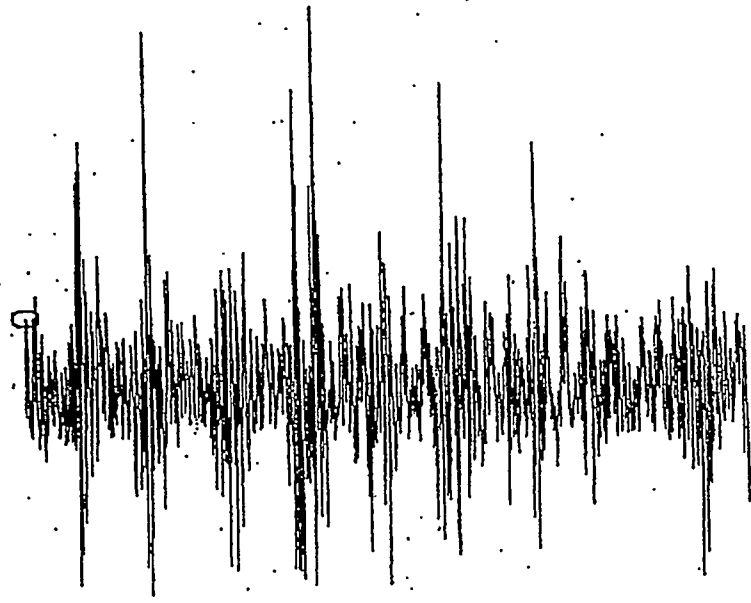


Fig. 5

ROBUST FOREWARNING OF DYNAMICAL CHANGE FROM SINGLE-CHANNEL SCALP EEG DATA

V. Protopopescu, L. M. Hively, and P. C. Gailey

Oak Ridge National Laboratory
Oak Ridge, TN 37831, USA

ABSTRACT

We present a robust, model-independent technique for measuring changes in the dynamics underlying nonlinear time-serial data. We define indicators of dynamical change by comparing distribution functions on the attractor via L_1 -distance and χ^2 statistics. We validate these measures against model data and then we apply them to clinical single-channel, scalp EEG data with the objective of capturing the transition between non-seizure and epileptic brain activity in a timely, accurate, and non-invasive manner. We find a clear superiority of the new metrics in comparison to traditional nonlinear measures as discriminators of dynamical change.

INTRODUCTION

Nonlinear processes are ubiquitous. Examples include: brain and heart waves; electrical transients in power systems; fluid (air or water) flow over the surfaces of automobiles, airplanes, or submarines; weather and climate dynamics; machine tool chatter; nuclear reactor instabilities; fusion plasma instabilities; earthquakes; turbulent flow in conduits; fatigue and stress crack growth; and planetary or satellite motion. Typically, nonlinear data arise from a virtual "black box" with little or no knowledge of the underlying system, its dimensionality, or noise contamination. More often than not, traditional nonlinear analysis requires some assumptions about the underlying dynamics. For example, calculation of Lyapunov exponents or Kolmogorov entropy implicitly assumes that the process can at least be modeled as a (low dimensional) dynamical system. At a more fundamental level, one may ask whether the data arises from a stationary process. It is very likely that complex systems, such as the weather or the brain, could not be well modeled by low dimensional, stationary dynamics over long times.

The technologist must frequently distinguish or quantify differences between nonlinear states that are apparently similar, but actually different. Inherent nonlinearity and high levels of noise in most real-life systems make condition or state comparisons extremely difficult or even impossible with linear or traditional nonlinear analyses. New measures are needed that are less affected by noise and at the same time are more sensitive to structural or parametric changes in the underlying dynamics.

We describe a new model-independent method for measuring dynamical change in nonlinear, possibly nonstationary data. The dynamics of reference and test cases are represented as discrete distributions of the density of points in reconstructed phase space during different time windows. Variability is captured by the visitation frequency at various regions of phase space as described by the distribution function. The method quantifies differences in these reconstructed dynamics by comparing the distribution functions. We make no specific assumption about stationarity, because no dynamical properties are inferred from the reconstructed attractor. The system dynamics may change within the time window, but such variability presents no problem for our technique, which measures dynamical change over a variety of length scales, and over a wide range of time scales. Moreover, our method allows measurement of dynamical change that that occurs continuously or intermittently.

Recently, Moeckel and Murray [1] discussed similar concepts for measuring the “distance” between attractors from time-delay reconstructions. In this context, our method provides continuous measures of change, in contrast to stationarity tests for whether or not *any* statistically significant change has occurred. Due to their continuous nature and their independence from assumptions about stationarity, our measures are particularly useful for analysis of physiological data. We illustrate the practical use of the technique for such data, namely analysis of single-channel, scalp EEG for forewarning of epileptic seizures.

TRADITIONAL NONLINEAR MEASURES

We assume that an unknown scalar signal, x , is sampled at equal time intervals, τ , starting at time, t_0 , yielding a sequence of N points, $x_i = x(t_0 + i\tau)$. Dynamical process reconstruction [2] uses d -dimensional time-delay vectors, $y(i)=[x_i, x_{i+\lambda}, \dots, x_{i+(d-1)\lambda}]$, for a system with d active variables and time lag, λ . The choices of lag and embedding dimension, d , determine how well the reconstruction unfolds the dynamics for a finite amount of noisy data. A proper reconstruction allows calculation of nonlinear measures that are consistent with the original dynamics. Below, we use three traditional measures, for comparison to our phase-space indicators of dissimilarity.

The mutual information function is a nonlinear form of auto-correlation function. Mutual information was devised by Shannon and Weaver [3], and applied to time series by Fraser and Swinney [4]. Mutual information measures the information (in bits) that can be inferred from one signal about a second signal, and is a function of the time delay between the measurements. Univariate (bivariate) mutual information measures information within the same (different) data stream(s) at different times. Here, we use the first minimum, M_1 , in the univariate mutual information function. M_1 measures the average time separation (in time-steps) that decorrelates two points in the time series.

The correlation dimension, D , measures process complexity and is a function of scale length, δ , in the data. Here we use the maximum-likelihood correlation dimension developed by Takens with modifications for noise by Schouten et al. [5,6].

The Kolmogorov entropy, K , measures the rate of information loss (bits/s). Positive, finite entropy generally is considered to clearly indicate chaotic features. Large entropy implies a stochastic, totally

unpredictable process. Entropy measures the average time for two points on an attractor to evolve from a small initial separation to more than a specific (large) distance, $\delta > \delta_0$. We use maximum-likelihood entropy by Schouten et al. [7].

Noise corrupts all real data. In addition, finite precision computer arithmetic truncates model data. Thus, we choose a finite-scale length that is larger than the noise, $\delta_0 = 2a$, at which to report K and D , corresponding to finite-scale dynamical structure. Our choice of length scale balances local dynamics (typically at $\delta \leq 3a$) against avoidance of excessive noise (typically at $\delta \leq a$). The symbol, a , denotes the absolute average deviation as a robust indicator of variability⁵ in the time serial data:

$$a = (1/N) \sum_{i=1}^N |x_i - \underline{x}|. \quad (1)$$

where symbol \underline{x} denotes the mean of x_i . Thus, our values of K and D have smaller values than expected for the zero-scale-length limit.

NEW MEASURES OF DYNAMICAL CHANGE

Traditional nonlinear measures characterize global features by averaging or integrating over the data. Such measures describe the long-term behavior but poorly indicate dynamical change. Greater discrimination is possible by more detailed analysis of the reconstructed dynamics. The natural (or invariant) measure on the attractor provides a more refined representation of the reconstruction, describing the visitation frequency of the system dynamics over the phase space. We begin by converting each signal value, x_i , to one of S different integers, $\{0, 1, \dots, S-1\}$:

$$0 \leq s_i = \text{INT}[S(x_i - x_{\min})/(x_{\max} - x_{\min})] \leq S-1. \quad (2)$$

Here, x_{\min} and x_{\max} denote the minimum and maximum values of x_i , respectively, over the reference case only and INT is a function that rounds a decimal number to the closest lower integer. For $x_{\min} \leq x_i \leq x_{\max}$, the inequality $0 \leq s_i \leq S-1$ holds trivially. We take $s_i(x_i = x_{\max}) = S-1$ in order to maintain exactly S distinct symbols and to partition the phase space into S^d hypercubes or bins. We then discretize the distribution function on the attractor, by counting the number of phase-space points occurring in each bin. We denote the population of the i -th bin of the distribution function, P_i , for the base case, and Q_i for a test case, respectively. For this work, we iteratively vary each parameter (S , d , N , etc.) with the others fixed, to obtain optimum sensitivity of the measures to changes in process dynamics. A systematic method to determine optimal values for these parameters is the subject of future work.

We use an embedding window, $M_1 = (d-1)\lambda$. Here, the first minimum in the mutual information function, M_1 , is measured in timesteps. We obtain an integer value for the lag from the previous equation by $\lambda = \text{INT}[0.5 + M_1/(d-1)] \geq 1$, thus constraining the largest value of dimensionality to $d \leq 2M_1 + 1$.

We compare the distribution function of a test state to the reference state, by measuring the dissimilarity between P_i with Q_i via the χ^2 statistics and L_1 distance:

$$\chi^2 = \sum_i (P_i - Q_i)^2 / (P_i + Q_i), \text{ and} \quad (3)$$

$$L = \sum_i |P_i - Q_i|. \quad (4)$$

The summations include all of the populated cells in the phase space. The sum in the denominator of Eq. 3 is based on a test for equality of two multinomial distributions. Proper application of these measures requires a rescaling so that the total population of the test case distribution function is the same as the total population of the base case.

By connecting successive phase-space points as indicated by the dynamics, $y(i) \rightarrow y(i+1)$, we construct a 2d-dimensional phase-space vector, $Y(i)=[y(i), y(i+1)]$. Thus, we obtain a discrete representation of the process flow [8]. This approach extends the method to capture more dynamical information using pair-wise connectivity between successive d-dimensional states. We use base-S arithmetic to assign an integer identifier $j \equiv I_i$ for the i-th phase-space state, using $I_i = \sum_{m=1}^{d-1} s_i(m) S^{m-1}$. The sum runs from $m=1$ to $m=d$, corresponding to successive components of the d-dimensional phase-space vector. The symbol, $s_i(m)$, denotes the m-th component of the i-th phase-space vector. The numeric identifier for the sequel phase-space point is $k \equiv I_{i+1}$. Then, we can define the measure of the dissimilarity between these two connected phase-space states, as before, via the L_1 -distance and χ^2 statistics:

$$\chi_c^2 = \sum_{jk} (P_{jk} - Q_{jk})^2 / (P_{jk} + Q_{jk}), \text{ and} \quad (5)$$

$$L_c = \sum_{jk} |P_{jk} - Q_{jk}|. \quad (6)$$

P_{jk} and Q_{jk} denote the distribution functions for the base case and test case, respectively, in the connected phase space. The summations in both equations run over all of the populated cells in the connected phase space. The subscript, c, denotes the connected measures, which are stronger metrics than the non-connected versions, according to the following inequalities [9-10]: $\chi^2 \leq L$, $\chi_c^2 \leq L_c$, $L \leq L_c$, and $\chi^2 \leq \chi_c^2$.

VALIDATION

We test the discriminating power of our measures on chaotic regimes of the Lorenz system [9] and of the Bondarenko model [11]. The latter model mimics high-dimensional EEG dynamics via a system of delay-differential equations. The Lorenz model reads [12]:

$$\begin{aligned} dx/dt &= a(y - x) \\ dy/dt &= rx - y - xz \\ dz/dt &= xy - bz. \end{aligned} \quad (7)$$

As stated before, some traditional nonlinear measures are good indicators of a bifurcation or transition to chaos. However, transitions between two chaotic regimes are poorly detected by these measures, especially for relatively small changes in the parameter that underlies the transition. Therefore we focus on detecting dynamical changes within a region where the Lorenz system is known to behave chaotically, namely [13]: $a = 10$, $b = 8/3$, and $25 \leq r \leq 90$. We compute various nonlinear measures versus r , by analyzing only the time serial values of z . The results of this analysis are as follows [9]. The correlation dimension, D , varies erratically from 1.7 to 2.15 over the whole range of r . The Kolmogorov entropy, K , also varies irregularly from 0.03 to 0.05. The value of M_1 , increases somewhat monotonically, but step-wise as r rises, so that relatively large variations in r are poorly indicated (e.g., constant for $60 \leq r \leq 72$). In sharp contrast, as r rises from 25 to 90, the PS and CPS measures increase almost monotonically from zero to rather large values. The values of L and χ^2 essentially coincide over the whole range because the measures are dominated by (C)PS domains that are populated only for the base case ($Q_i > 0$ for $R_i = 0$) and only for the unknown ($R_i > 0$ for $Q_i = 0$), for which the two measures become analytically equivalent.

We also assess the phase-space measures by testing them on the Bondarenko neuron model [11], which is a coupled set of time-delayed ordinary differential equations:

$$du_i/dt = -u_i(t) + \sum_{j=1}^M a_{ij} f(u_j(t - \tau_j)), \quad (8)$$

The signal from the i -th neuron is $u_i(t)$. The indices, i and j , run from 1 to $M=10$ for ten neurons. The matrix, a_{ij} , is a set of coupling coefficients having uniformly random values, $-2 \leq a_{ij} \leq 2$. The time delay is a constant, $\tau_j = 10$. The function, $f(x) = c \tanh(x)$, simulates nonlinear neural response to signals from neighboring neurons. We concentrate on measuring dissimilarity within a region where the Bondarenko system is known to behave chaotically [11]: $5 \leq c \leq 16$. We use one of the ten neuron signals for dissimilarity detection. The results of this analysis are as follows [10]. The correlation dimension varies erratically between 3.5 and 8.5 as c increases from 5 to 16. Over the same range of c , the Kolmogorov entropy rises almost monotonically from 0.025 to 0.16. The location of the first minimum in the mutual information function, M_1 , also varies erratically as c increases. In sharp contrast, as c rises from 5 to 16, the (connected) phase space measures increase almost monotonically over several orders of magnitude. As before, the values of L and χ^2 essentially coincide over the whole range because the measures are dominated by phase space bins that are populated only for the base case $P_i > 0$ for $Q_i = 0$ and only the test case $P_i > 0$ for $Q_i = 0$, for which the two measures become analytically equivalent.

Analysis of these two analytical models of chaotic dynamics shows continuous change in the phase-space measures, which increase monotonically by four orders of magnitude over a reasonable parameter range. Over this same parameter range, the phase-space measures of condition change consistently outperform the traditional nonlinear measures, which are indistinguishable from noise or vary erratically by a factor of two. These results provide confidence that the phase-space measures are useful for noisy clinical EEG data.

EEG DATA ANALYSIS AND RESULTS

We analyze a fixed channel of scalp EEG with 12-bit precision at a sampling rate of 512 Hz. Table 1 summarizes these nine datasets with monitoring periods of 1380-3115 seconds. The clinical seizures begin at 966-2775 seconds. We also analyze digital scalp EEG from other clinical sites, sampled at 200 Hz with 10-11 bits of precision. These data have 23-32 channels with monitoring periods of 2,217-20,000 seconds. The clinical seizures begin at times that range over 1,930-15,750 seconds. Only one clinically designated channel was examined in each of these eleven datasets, as shown in Table 1.

We choose $N=22,000$ data points for each cutset to balance better time discrimination (smaller N) against higher statistical power (larger N). We next remove muscular artifacts (e.g., eye blinks) with a zero-phase quadratic filter [9-10]. We designate the first ten non-overlapping time windows (cutsets) as base cases. We then compare each base case cutset to every test case cutset to obtain average values for χ^2 and L (and a corresponding standard deviation of the mean). We find that $d=3$ and $S=22$ are adequate for this data. The value of M_1 comes from the base case period of (nonseizure) data.

The substantial disparity in range and variability of the conventional and phase-space measures makes them difficult to compare and interpret. To remove this disparity and compare all the measures on a consistent basis, we renormalize the nonlinear measures as follows. For each nonlinear measure, V , we define V_i as the value of nonlinear measure for the i -th cutset. The variable, V , is in turn D , K , M_1 , χ^2 , etc. We obtain the mean, \underline{V} , of V_i over the ten non-overlapping base case cutsets. The corresponding sample

standard deviation is denoted by σ . Then, the renormalized form is $U(V) = |V_i - \bar{V}|/\sigma$. For an indication of change, we use $U > U_c = 3.09$, corresponding to a false positive probability of $<10^{-3}$ in Gaussian random data. We require two or more consecutive occurrences of a positive indication to avoid spurious false positives, corresponding to a joint false positive probability of $<10^{-6}$ in Gaussian data.

Table 1: Summary of EEG datasets

Dataset #	# Channels	Seizure (s)	Tot Time (s)	Channel	Sample Rate (Hz)
109310	16	2775	3115.3	13	512
109314	16	2480	2742.4	13	512
119230	16	2491	2917.4	13	512
119234	16	2560	2649.6	13	512
62723t	16	2620	3060.8	13	512
69212	16	2356	2547.8	13	512
73305d	16	1245	1380	13	512
c8492d	16	966	1603.6	13	512
wm12sd	16	1041	1428.6	13	512
szpr00	23	5236	5401	Fp2	200
szprec	32	1930	2217	F7	200
szpr03	32	1932	2217	T4	200
szpr04	23	3794	3963	T4	200
ezpr05	23	4888	6000.2	T4	200
emu02	27	4320	15,006	F4	200
emu03	27	13,200	16,228	C3	200
emu04	27	15,750	18,423	C4	200
emu14	27	4080	20,000.2	F4	200
emu18	27	4200	18,000.2	T3	200
emu26	27	13,987	16,224	Fp1	200

Table 2 summarizes the forewarning times for each renormalized nonlinear measure over the twenty EEG datasets. A negative value of forewarning time corresponds to an indication after seizure onset. Starred (*) values indicate that no condition change was detected by this measure. Bold entries denote the earliest time of change. These results are assessed as follows. The phase space measures provide the earliest seizure forewarning in 11, 10, 14, and 13 datasets for L , L_c , χ_c^2 , and χ^2 , respectively. Moreover, the phase-space measures provide pre-seizure indications in all twenty cases. In sharp contrast, the traditional nonlinear measures only give the earliest forewarning of a seizure in 1, 1, and 3 instances for K , M_1 , and D , respectively. These same traditional measures provide no forewarning of a seizure in 7, 8, and 6 cases, respectively. The total number of instances of earliest-forewarning times exceeds twenty, because more than one measure can simultaneously detect condition change. We note that the forewarning time (10 seconds) for dataset #wm12sd is too short to be clinically useful. In addition, the forewarnings of more than one hour (datasets # emu003, emu004, emu026) are too long to be clinically useful. These results show that the phase space measures are much superior to the conventional nonlinear

measures as pre-seizure indicators of condition change for a single channel of scalp EEG. Analysis of normal EEG shows no positive indication of change.

Table 2: Times (seconds prior to seizure) when change is detected

Dataset #	D	K	M ₁	L _c	L	χ_c^2	χ^2
109310	1099	*	*	-61	-61	1142	-61
109314	1921	1406	1835	1878	1921	1921	1921
119230	901	386	-216	471	-44	471	514
119234	1915	*	*	1915	1915	1915	1915
62723t	1374	*	-44	2233	1675	2233	2233
69212	*	165	637	1626	1497	1626	1626
73305d	600	600	*	343	772	-87	772
c8492d	-22	321	364	193	193	193	193
wm12sd	*	*	*	-76	10	10	10
szprec	500	-160	500	610	610	610	610
szpr00	*	*	1496	726	-154	836	1716
szpr03	-158	-158	172	502	502	502	502
szpr04	-166	*	-166	384	384	384	384
szpr05	3568	3348	3568	3678	3568	3678	3568
emu002	*	-190	-410	2230	2780	1900	2780
emu003	*	*	*	12760	12760	12760	12760
emu004	*	6950	*	13660	13550	14540	13660
emu014	*	*	-540	670	670	-210	670
emu018	-90	-1630	-310	3650	2220	3650	2220
emu026	11127	11237	4747	11237	11237	11237	11237

Figure 1 shows changes in various metrics as functions of time, for dataset #c8492d. The first 300 seconds of data displays modest variability in all of the measures, representing the dynamics of normal brain activity. The clinical seizure occurs at 966-1035 seconds, as indicated by the vertical bars at these times; all of the measures clearly show the seizure. Maxima and minima in the raw EEG (Fig. 1a) provide no pre-seizure indications, nor does the correlation dimension, D, (Fig. 1b). Both the Kolmogorov entropy, K, (Fig. 1c) and mutual information, M₁, (Fig. 1d) show pre-seizure change, beginning at 750 seconds. Connected (solid lines) and non-connected (dashed lines) phase-space measures for the L₁-distance (Fig. 1e) and χ^2 statistic (Fig 1f) exhibit significant dissimilarity, starting at around 600 seconds. The ordinate value of the respective metric change, U(.), are in units of standard deviation from the mean.

DISCUSSION

The present results differ markedly from previous work, which used conventional nonlinear measures, such as correlation dimension [14], largest Lyapunov exponent [15], and correlation integral [16]. First, previous investigations used multichannel data from subdural and depth electrodes. The present work uses single-channel *scalp* EEG data, which allows non-invasive, ambulatory, long-term, non-clinical monitoring. The use of scalp data is made possible by the combined effect of sensitive measures and

effective low frequency artifact filtering [17]. The robustness of the methodology has been tested over a variety of clinical conditions: digital and analog EEG data from several clinical sites; data sampled at 200 and 512 Hz; raw EEG data precision between 10-12 bits; presence of substantial noise in the raw EEG; various types of seizure; use of a fixed channel in the bipolar montage (channel 13 which lies over the patient's right eye and has a large eye-blink artifact) as well as various clinically designated channels in the 10-20 montage. We intend to develop the methodology to include: (i) consistent use of multi-channel data for improved monitoring and forewarning; (ii) analysis of surrogate data; (iii) more robust renormalization techniques to facilitate broad comparisons; and (iv) other medical, engineering, and geophysical applications.

ACKNOWLEDGMENT

This article has been authored by a contractor of the U. S Government under Contract No. DE-AC05-00OR22725. Accordingly, the Government retains a nonexclusive, royalty free license to publish or reproduce the published form of this contribution, or allow others to do so, for U.S. Government purposes. Research sponsored in part by the Engineering Research Program of the Office of Basic Energy Sciences, U. S. Department of Energy. The Oak Ridge National Laboratory is managed for the U. S. Department of Energy BY UT-Battelle, LLC under contract DE-AC05-00OR22725.

REFERENCES

1. B. R. MOECKEL and B. MURRAY, *Physica D* **102**, 187 (1997).
2. J.-P. ECKMANN and D. RUELLE, *Rev. Mod. Phys.* **57**, 617 (1985).
3. C. E. SHANNON and W. WEAVER, *The Mathematical Theory of Communication*, University of Illinois Press, Urbana (1949).
4. A. M. FRASER and H. L. SWINNEY, *Phys. Rev A* **33**, 1134 (1986).
5. J. C. SCHOUTEN, F. TAKENS, and C. M. van den BLEEK, *Phys. Rev. E* **50**, 1851 (1994).
6. F. TAKENS, *Lecture Notes in Mathematics* **1125** (1984) 99, Springer-Verlag, Berlin.
7. J. C. SCHOUTEN, F. TAKENS, and C. M. van den BLEEK, *Phys. Rev. E* **49**, 126 (1994).
8. H. D. I. ABARBANEL, *Analysis of Observed Chaotic Data*, Springer Publ., New York (1996).
9. L. M. HIVELY, P.C. GAILEY, and V.A. PROTOPOPESCU, *Phys. Lett. A* **258**, 103 (1999).
10. L. M. HIVELY, V.A. PROTOPOPESCU, and P. C. GAILEY, *submitted to Chaos* (2000).
11. V. E. BONDARENKO, *Int. J. Bifur. Chaos* **7**, 1133 (1997).
12. E. N. LORENZ, *J. Atmos. Sci.* **30**, 130 (1963).
13. E. A. JACKSON, *Perspectives of Nonlinear Dynamics*, Vol. 2, Cambridge University Press, Cambridge (1990).
14. K. LEHNERTZ and C. E. ELGER, *Phys. Rev. Lett.* **80**, 5019 (1998).
15. L. D. IASEMIDIS and J.C. SACKELLARES, *Neuroscientist* **2**, 118 (1996).
16. M. Le VAN QUYEN, J. MARTINERIE, M. BAULAE, and F. VARELA, *NeuroReport* **10**, 2149 (1999).
17. L. M. HIVELY, N. E. CLAPP, C. S. DAW, W. F. LAWKINS, and M. L. EISENSTADT, *ORNL/TM-12961* (Oak Ridge National Laboratory, Oak Ridge, TN) 1995.

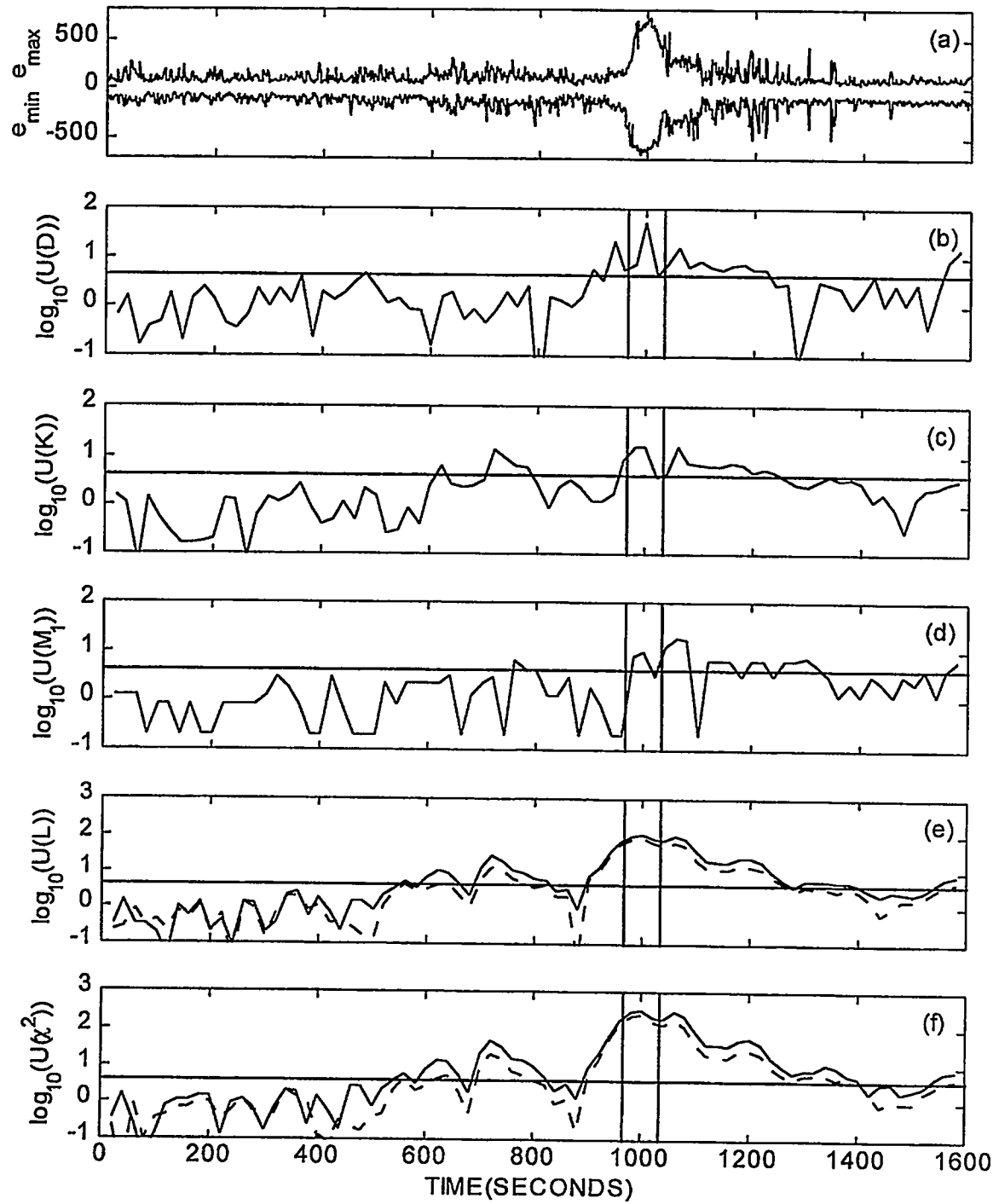


Figure 1: Various metrics for dataset #c8492D versus time (see text for complete explanation)

ENERGY LOCALIZATION, ENERGY PROPAGATION, AND THERMAL RESONANCE IN NONLINEAR ARRAYS

K. Lindenberg, R. Reigada, and A. Sarmiento

Department of Chemistry and Biochemistry and Institute for Nonlinear Science
University of California, San Diego
La Jolla, CA 92093-0340, U.S.A.

ABSTRACT

Signal propagation in discrete nonlinear noisy media has been connected to dynamical processes in systems as diverse as chemical excitable media, arrays of coupled electronic resonators, dislocations in crystals, adsorbed atomic layers, and cardiac tissue. We highlight a number of interesting properties of nonlinear arrays consisting of masses connected by anharmonic springs. In particular, we focus on the effects of a thermal environment and on the role that thermal fluctuations may play in energy localization and propagation in these chains. We show that it is possible to tune the temperature to obtain optimal response, and that the optimal temperature depends on the desired response. We also show that the dynamics of activated processes depend sensitively on the nature of the thermal environment.

In the past few years it has become abundantly clear that the presence of noise in nonlinear systems may lead to an enhancement of a number of desirable features such as energy localization and mobility and the detection and propagation of weak signals. The interplay of stochasticity and nonlinearity that amplifies the system response is a cooperative phenomenon whose detailed nature depends on the particular structure of the system and the forces acting upon it. Recent literature, including our own work [1–3], has focused on spatially extended systems [4] including noise-enhanced propagation in coupled arrays of bistable units [5, 6], excitable media [7–9], reaction-diffusion systems [10], and dynamics and signal propagation in cardiac tissue [11, 12]. It has been repeatedly noted that *discrete* extended systems pose particular mathematical challenges that have barely been explored in spite of the fact that many physical systems are intrinsically discrete [13–17]. We focus on some of the simplest nonlinear arrays, namely, chains of masses connected by anharmonic springs, thereby isolating some of the most generic features responsible for these cooperative phenomena.

In this report we highlight some of our results concerning four sets of questions: 1) What is the texture (magnitude, spatial distribution, persistence) of thermal fluctuations in various discrete anharmonic arrays [1, 3]? 2) How does a pulse travel and disperse along these arrays and how are these properties affected by temperature [2]? 3) How do various chains transmit a persistent signal applied at one end (amplitude and distance of travel) and how are these properties affected by

temperature? 4) If a bistable impurity is embedded in a thermalized discrete medium, how does the nature of the medium affect the transition rate of the impurity [3]?

The equations of motion for chains of N unit masses are

$$\ddot{x}_n = - \sum_{m=1}^N V'(x_n, x_m) - \gamma \dot{x}_n + \eta_n(t) \quad (1)$$

where $n = 1, \dots, N$, γ is a dissipation parameter, and the η 's are zero-centered Gaussian thermal fluctuations that obey the fluctuation-dissipation relation at temperature T , $\langle \eta_n(t) \eta_m(\tau) \rangle = 2\gamma k_B T \delta_{nm} \delta(t - \tau)$. Dots denote time derivatives and the prime a derivative with respect to x_n . The potential of interaction $V(x_n, x_m)$ connects only nearest neighbors. We consider three prototype potentials (here $x \equiv x_n - x_m$):

$$V(x) = \frac{1}{2} k x^2 + \frac{1}{4} k' x^4 \quad \text{hard} \quad (2)$$

$$= \frac{1}{2} k x^2 \quad \text{harmonic} \quad (3)$$

$$= \frac{k}{k'} \left[|x| - \frac{1}{k'} \ln(1 + k'|x|) \right] \quad \text{soft} \quad (4)$$

The numerical integration of the stochastic equations is performed using the second order Heun's method (equivalent to a second order Runge Kutta integration) [18, 19].

In Fig. 1 we display a typical set of equilibrium energy landscapes for the three chains with periodic boundary conditions [1, 3], all at the same temperature and subject to the same damping parameter. Darker regions represent higher energies. The horizontal axis indicates the location along the chain and the vertical axis is time evolving upward. Noteworthy features (robust over broad ranges of parameter values) are: 1) The magnitude of the fluctuations is greatest in the soft chain. This can be explained straightforwardly using the virial theorem [20]; 2) The fluctuations are mobile in the harmonic and hard chains but not in the soft; 3) The thermal fluctuations travel most rapidly and remain localized over considerably greater distances in the hard chain.

Now suppose that a strong (relative to thermal motions) kinetic energy pulse is applied to a particular site on the chain. The pulse then propagates and disperses. We obtain the following results, not all of which can be illustrated here [2]. The pulse in the hard chain propagates *more rapidly* as one increases its intensity, decreases the damping, or increases the temperature. The pulse in the soft chain propagates *more slowly* with these same variations, and the pulse velocity in the harmonic chain is *independent* of these variations. The dispersion increases in all cases with increasing temperature, but most slowly in the hard chain. A rather dramatic illustration of the different effects of damping on the different chains is shown in the left panel of Fig. 2. The effect of a temperature increase is illustrated in the right panel of the figure. The quantities displayed are the local energy $E(n)$ defined as

$$E(n) = \frac{\dot{x}_n^2}{2} + \frac{1}{2} V(x_{n+1}, x_n) + \frac{1}{2} V(x_n, x_{n-1}) \quad (5)$$

(here illustrated for $n = 5$), and the average distance $\langle x \rangle$ traveled by the pulse, defined as

$$\langle x \rangle = \frac{\sum_n |n| E(n)}{\sum_n E(n)}. \quad (6)$$

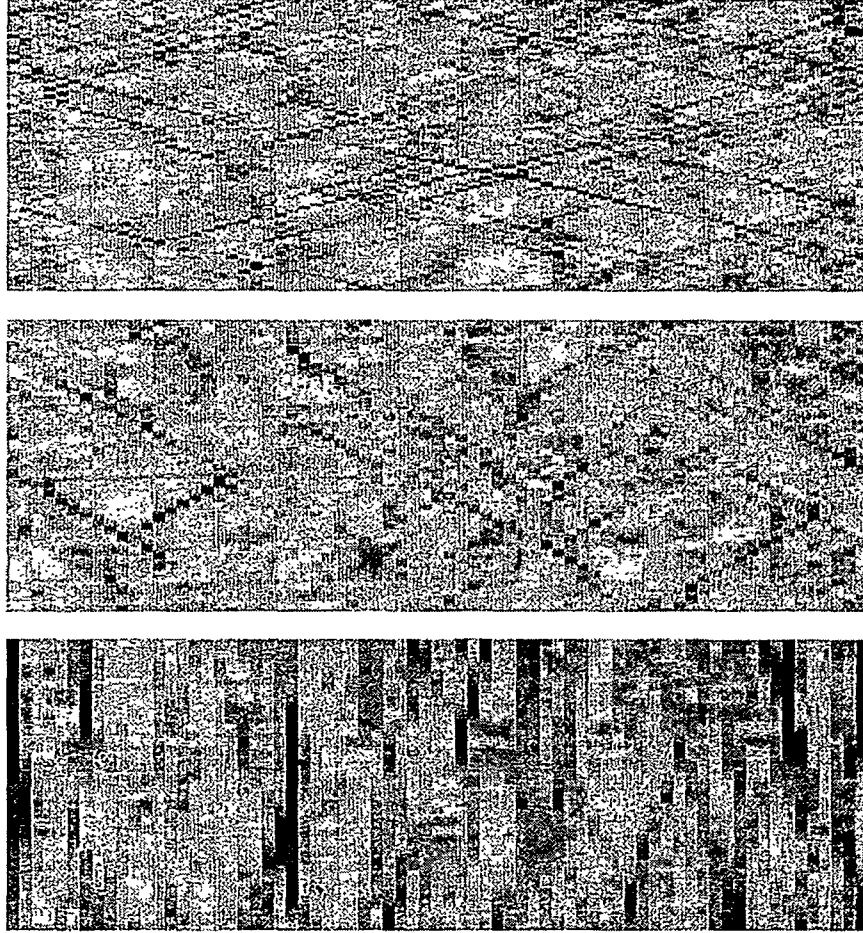


Figure 1: $k_B T = 0.08$, $\gamma = 0.005$, $N = 71$, $t_{max} = 160$. Hard (top): $k = 0.1$, $k' = 1$. Harmonic (middle): $k = 0.1$. Soft (bottom): $k = 0.1$, $k' = 5$.

These results, some of them perhaps counterintuitive, all follow from the observation that pulse velocity increases with average array frequency while pulse dispersion decreases with increasing frequency. Increased pulse intensity, decreased damping and higher temperature are all associated with higher energy; in turn, a higher energy in a hard chain leads to a higher average frequency. In a soft chain higher energies are associated with lower frequencies, and in a harmonic chain the average frequency is independent of energy [2]. The connection between pulse velocity and dispersion and the average array frequency can be established analytically for a periodic chain, but is at this point only a numerical observation for the anharmonic arrays.

The tendencies of the hard array to keep the energy “together” and to transport it more quickly may conflict under certain conditions. For example, in a two-dimensional hard array a front travels more rapidly with increasing temperature, but a local pulse that would have to travel out radially tends to remain localized because outward motion along the bonds of the lattice as required by symmetry would disperse the energy [2] (see Fig. 3).

Next suppose that a sustained sinusoidal signal $\dot{x}(t) = A \sin(\omega_0 t)$ is applied at one site of an otherwise free chain. We observe the propagation of the signal along the chain and, in particular, its temperature dependence. We observe that in a hard chain increasing the temperature can lead to enhanced signal propagation (whereas this does not occur for the other chains). Of course if

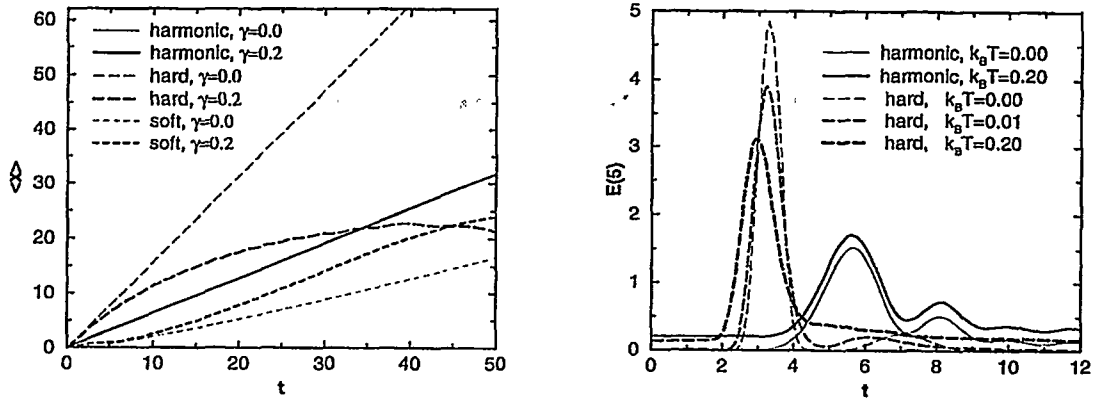


Figure 2: Left panel: Mean distance traveled by the pulse as a function of time for hard ($k = 0$, $k' = 1$), harmonic ($k = 1$), and soft ($k = k' = 1$) chains of 151 sites at zero temperature and for different damping coefficients. Initial momentum at the middle site is $\dot{x}(t = 0) = 8$. Right panel: Energy profile vs time at the 5th site from the initial pulse at different temperatures with damping parameter $\gamma = 0.2$.

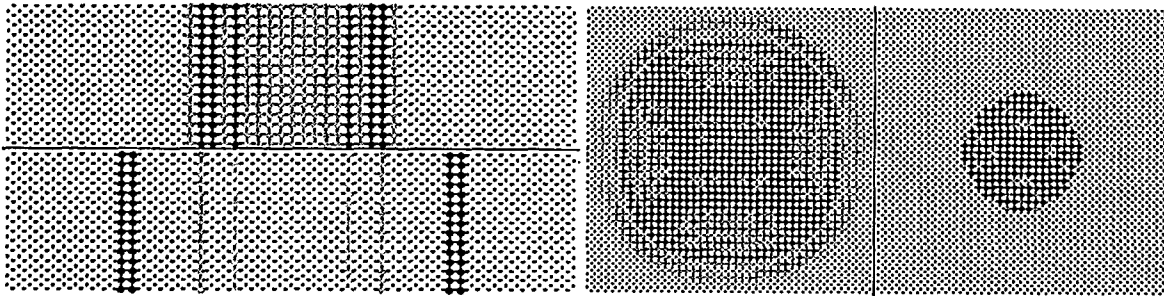


Figure 3: Left panel: energy distribution at a subsequent time for an initial front in a harmonic (upper) and hard lattice (lower). Right panel: energy distribution at a subsequent time for an initial pulse at the center of a harmonic (first) and hard (second) array.

the temperature is too high the signal is buried in the fluctuations and transmission ceases to be effective. Thus we conclude that the temperature can be tuned to achieve optimal transmission properties, with a specific temperature leading to optimization of a specific property. For example, there is an optimal temperature to maximize the signal-to-noise ratio (SNR)

$$SNR(j) \equiv \log_{10} \left(\frac{\text{signal power } (j)}{\text{thermal power } (j)} \right), \quad (7)$$

at a given distance from the forced site, or one can choose a temperature to optimize the transmission distance. These effects are illustrated in Fig. 4. The SNR at site j is expressed in terms of the power spectral density $S_j(\omega)$ at each site j defined as a Fourier transform of the velocity autocorrelation function; the thermal power is estimated by performing a polynomial fit to $S_j(\omega)$ around – but not including – the forcing frequency ω_0 , and the signal power is just the value $S_j(\omega_0)$. The SNR at different distances from the forced site as a function of temperature for a hard chain is shown in the left panel (in the other chains the dependences are monotonically decreasing at all sites). The propagation length is defined as the maximum distance at which the SNR exceeds

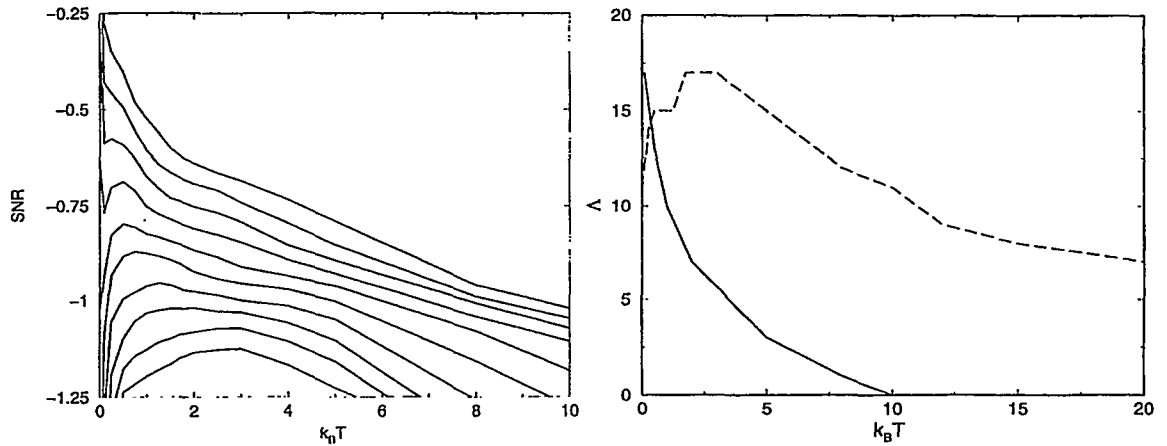


Figure 4: Left panel: SNR curves as a function of temperature for different sites from $n = 6$ (highest curve) to $n = 15$ (lowest curve) along the hard chain with $k = 0$, $k' = 5$, $\gamma = 0.2$, $A = 0.5$, and $\omega_0 = 1$. Right panel: propagation length as a function of temperature for the hard chain (dashed curve) and for a harmonic chain (solid curve) ($k = 1$).

a threshold value. The propagation length as a function of temperature with the threshold value arbitrarily picked as 0.4 is shown in the right panel. We have identified the maxima in the curves as *thermal resonances*, and point to this as one of the few cases in which such resonances are achieved by thermal (as opposed to external noise) tuning.

Finally, consider a bistable system embedded in our various thermal environments. Bistable systems are ubiquitously invoked as models for chemical processes. One well represents the “reactant” state, the other the “product” state, and separating them is the “activation barrier”. A thermal environment may induce transitions from one state to the other, and one studies the associated transition rate or “reaction rate”. This rate of course depends on the nature of the thermal environment and the way in which the bistable system is coupled to it. For example, one of the most extensively studied problems is that of the dependence of the transition rate on the damping [21]: at low damping the system is in the “energy-limited” regime where the transition rate increases with increasing damping. In this regime it is difficult for the system to gain or lose energy. Therefore the system tends to move periodically within one well, rarely gaining enough energy to move over the barrier. When it does so, it tends to recross the barrier many times within this single event before losing energy and becoming trapped again in one of the wells, where it again performs periodic motion. With increasing damping the transition eventually becomes “diffusion-limited.” Here the system tends to move erratically within one well. The system can easily gain energy from large fluctuations, but it can also lose energy rather easily. Therefore the independent barrier crossing events are more frequent, but recrossings are rare and the system immediately gets trapped in a well where it moves erratically until another large fluctuation causes another barrier crossing event.

If a bistable system is embedded in a chain which is in turn connected to a thermal environment, how does the nature of the chain affect the transition rate [3]? A sample of behaviors can be seen in Fig. 5, which shows the trajectory of the coordinate y of a bistable system connected to the three types of chains. When the bistable system is in the right (left) well the coordinate is $y = 1$ ($y = -1$). The thermal fluctuations and crossings over the barrier at $y = 0$ are apparent. Note that these three sample trajectories involve the same damping and temperature - the only difference

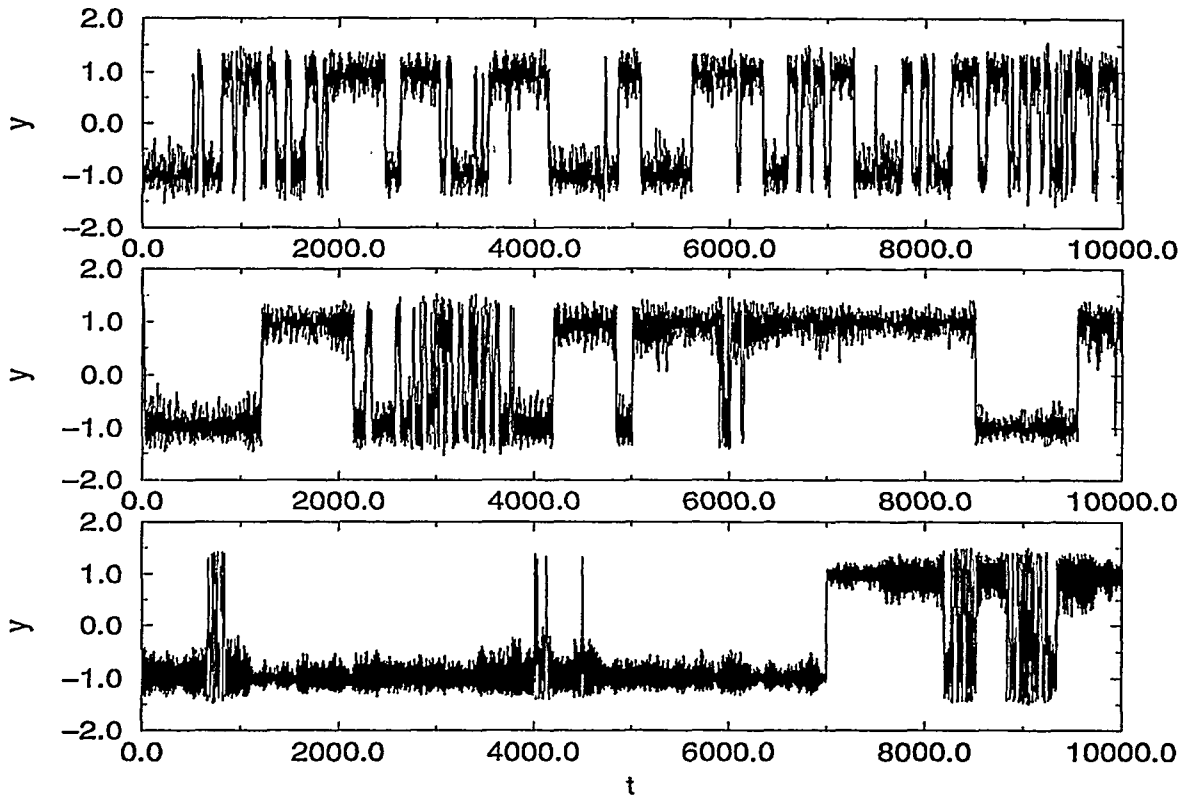


Figure 5: Trajectory of a bistable impurity with barrier height of 0.25 embedded in a chain of 30 oscillators with $k_B T = 0.08$, and $\gamma = 0.005$. Top panel: hard chain with $k = 0.1$ and $k' = 1$. Middle panel: harmonic chain with $k = 0.1$. Bottom panel: soft chain with $k = 0.1$ and $k' = 5$.

lies in the nature of each chain. Nevertheless the trajectories are entirely different; in particular, in the hard chain the trajectory is typical of the diffusion-limited regime, while in the soft chain it is that of the energy-limited regime. This is a direct reflection of the behavior seen in Fig. 1, that is, of the fact that in the hard chain the thermal fluctuations created elsewhere along the chain have a good chance of reaching the bistable impurity and hence causing a transition, but the same energy mobility also makes it easy for the impurity to then lose its energy back to the chain. In the soft chain, on the other hand, only fluctuations that occur in the sites immediately adjacent to the impurity can excite the impurity - fluctuations originating elsewhere do not travel to the impurity. These neighboring fluctuations are rarer but stronger and more persistent.

A useful characterization of these trajectories is the correlation function

$$C(\tau) = \frac{\langle y(t+\tau)y(t) \rangle}{\langle y^2(t) \rangle}, \quad (8)$$

where the brackets indicate an average over t . The correlation functions for the three trajectories of Fig. 5 are shown in Fig. 6. The oscillations apparent in the soft and harmonic chain at short times are the direct result of oscillatory motion characteristic of energy-limited behavior. The alternation of amplitudes of the oscillations in the soft chain correlation function is a direct consequence of the correlated periodic motion above the barrier that is associated with the prolonged bursts that often accompany the barrier crossing event. Such bursts are not nearly as prevalent in the harmonic system. The hard chain correlation function decays essentially monotonically: the suppression of oscillations is indicative of the erratic motion within the wells that is characteristic of higher

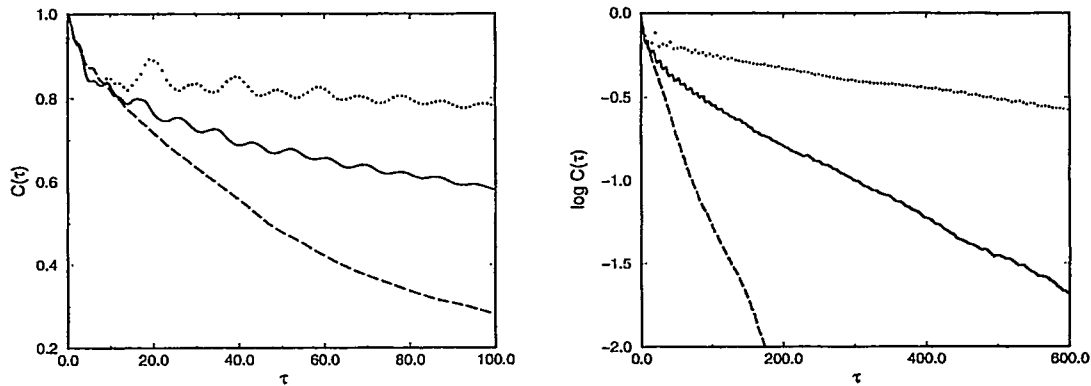


Figure 6: Correlation functions associated with the trajectories of Fig. 5. Dashed curves: hard chain; solid curves: harmonic chain; dotted curves: soft chain. Left panel: short-time behavior. Right panel: correlation function on a logarithmic scale.

effective damping. The slopes in the logarithmic rendition can be associated with the inverse of the transition rate from one well to the other. The transition rate is highest for the hard chain and lowest for the soft. The hard chain clearly provides the most favorable environment for transitions to occur at a given temperature. More detailed explanations, comparisons, and parameter variation effects can be found in Ref. [3].

ACKNOWLEDGEMENT

This work was performed under the auspices of the Engineering Research Program of the Office of Basic Energy Sciences at the U. S. Department of Energy. Portions of this work were carried out in collaboration with J. M. Sancho and A. H. Romero.

References

- [1] R. REIGADA, A. H. ROMERO, A. SARMIENTO and K. LINDENBERG, "One-Dimensional Arrays of Oscillators: Energy Localization in Thermal Equilibrium," *J. Chem. Phys.* **111**, 1373 (1999).
- [2] A. SARMIENTO, R. REIGADA, A. H. ROMERO and K. LINDENBERG, "Enhanced Pulse Propagation in Nonlinear Arrays of Oscillators," *Phys. Rev. E* **60**, 5317 (1999).
- [3] R. REIGADA, A. SARMIENTO, A. H. ROMERO, J. M. SANCHO and K. LINDENBERG, cond-mat/0003337, to appear in *J. Chem. Phys.*
- [4] J. GARCIA-OJALVO and J. M. SANCHO, *Noise in Spatially Extended Systems*, Springer, New York (1999).
- [5] J. F. LINDNER, S. CHANDRAMOULI, A. R. BULSARA, M. LOCHER and W. L. DITTO, "Noise Enhanced Propagation," *Phys. Rev. Lett.* **81**, 5048 (1998).

- [6] M. LOCHER, N. CHATTERJEE, F. MARCHESONI, W. L. DITTO and E. R. HUNT, "Noise Sustained Propagation: Local vs Global Noise," *cond-mat 0003048*.
- [7] S. KADAR, J. WANG and K. SHOWALTER, "Noise-Supported Travelling Waves in Sub-Excitable Media," *Nature* **391**, 770 (1998).
- [8] P. JUNG, A. CORNELL-BELL, F. MOSS, S. KADAR et al., "Noise-Sustained Waves in Subexcitable Media: From Chemical Waves to Brain Waves," *Chaos* **8**, 567 (1998).
- [9] P. JUNG and G. MAYER-KRESS, "Spatiotemporal Stochastic Resonance in Excitable Media," *Phys. Rev. Lett.* **74**, 2130 (1995).
- [10] F. CASTELPOGGI and H. WIO, "Stochastic Resonant Media: Effect of Local and Nonlocal Coupling in Reaction-Diffusion Models," *Phys. Rev. E* **80**, 5437 (1998).
- [11] J. P. KEENER, "The Effect of Gap Junctional Distribution on Defibrillation," *Chaos* **8**, 175 (1998).
- [12] W. C. COLE, J. B. PICONE and N. SPERELAKIS, "Gap Junction Uncoupling and Discontinuous Propagation in the Heart. A Comparison of Experimental Data with Computer Simulations," *Biophys. J.* **53**, 809 (1988).
- [13] S. FLACH and C. R. WILLIS, "Discrete Breathers," *Phys. Rep.* **295**, 181 (1998).
- [14] C. LAROCHE, T. DAUXOIS and M. PEYRARD, "Discreteness Effects on Soliton Dynamics: A Simple Experiment," *chao-dyn/0002001*.
- [15] T. PROSEN and D. K. CAMPBELL, "Momentum Conservation Implies Anomalous Energy Transport in 1D Classical Lattices," *chao-dyn/9908021*.
- [16] P. J. MARTINEZ, L. M. FLORIA, F. FALO and J. J. MAZO, "Intrinsically Localized Chaos in Discrete Nonlinear Extended Systems," *Europhys. Lett.* **45**, 444 (1999).
- [17] C. GIARDINA, R. LIVI, A. POLITI and M. VASSALLI, "Finite Thermal Conductivity in 1D Lattices," *Phys. Rev. Letters* **84**, 2144 (2000).
- [18] T. C. GARD, *Introduction to Stochastic Differential Equations*, Marcel Dekker, Vol.114 of *Monographs and Textbooks in Pure and Applied Mathematics* New York: Marcel Dekker (1987).
- [19] R. TORAL, in *Computational Field Theory and Pattern Formation*, 3rd Granada Lectures in Computational Physics, Lecture Notes in Physics Vol. 448, Berlin: Springer Verlag (1995).
- [20] D. W. BROWN, L. BERNSTEIN, and K. LINDENBERG, "Stochastic Localization," *Phys. Rev. E* **54**, 3352 (1996).
- [21] V. I. MELNIKOV, "The Kramers Problem: Fifty Years of Development," *Phys. Rep.* **209**, 1 (1991).